A Reduced Order Model for the Dynamics of Long Flexible Cylinders in an offshore environment

Dissertation

submitted to and approved by the

Department of Architecture, Civil Engineering and Environmental Sciences
University of Braunschweig – Institute of Technology

and the

Department of Civil and Environmental Engineering
University of Florence

in candidacy for the degree of a
Doktor-Ingenieur (Dr.-Ing.) /
Dottore di Ricerca in Civil and Environmental Engineering[*)]
by

Giovanni Stabile
born 03/10/1987
from Bagno a Ripoli, Italy

Submitted on	01/03/2016
Oral examination on	10/05/2016
Professorial advisors	Prof. Claudio Borri Prof. Hermann G. Matthies

2016

*) Either the German or the Italian form of the title may be used.

ABSTRACT

In this thesis the development of a reduced order model for the analysis of long flexible cylinders in an offshore environment is proposed. In particular the focus is on the modelling of the vortex induced vibrations and the aim is the development of a model capable of capturing both the in-line and cross-flow oscillations.

The reduced order model is identified starting from the results of a high fidelity solver developed coupling together a finite element solver with a computational fluid dynamics finite volume solver. The high fidelity analyses are conducted on a reduced domain size representing a small section of the long cylinder, which is nevertheless, already flexible. The section is forced using a motion which matches the expected motion in full scale, and the results are used for the system-parameter identification of the reduced order model.

Several different models are analysed and their results are compared and discussed. The reduced order model is identified by using a system and parameter identification approach. The final proposed model consists in the combination of a forced van der Pol oscillator, to model the cross-flow forces, and a linear state-space model, to model the in-line forces.

The model developed in such a way is applied to study a full scale flexible model and the results are validated by using experiments conducted inside a towing tank. Finally the parameter identification, focusing on the van der Pol model is repeated in a probabilistic setting. In particular, the applicability of the ensemble Kalman filter for the parameter estimation of the van der Pol oscillator is discussed and analysed.

SOMMARIO

In questa tesi è proposto lo sviluppo di un modello ridotto per l'analisi di strutture cilindriche snelle e flessibili in ambiente offshore. In particolare l'attenzione è focalizzata sulle vibrazioni indotte dal distacco dei vortici. L'obiettivo finale è lo sviluppo di un modello capace di catturare la risposta sia in direzione trasversale che longitudinale rispetto alla direzione del flusso.

Il modello ridotto è stato identificato utilizzando i risultati di un solutore ad alta fedeltà per interazione fluido struttura ottenuto accoppiando un solutore agli elementi finiti con un solutore per fluidodinamica computazionale ad i volumi finiti. Le analisi ad alta fedeltà sono state condotte su di un dominio ridotto rappresentante un tronco estratto dall'intera struttura in cui la flessibilità è comunque considerata. Agli estremi del modello in scala ridotto è imposta una storia di spostamenti che riproduce la risposta attesa in scale reale. I risultati sono poi utilizzati per l'identificazione del sistema dinamico utilizzato per il modello ridotto.

Sono analizzati diversi modelli e le loro caratteristiche fondamentali sono confrontate e discusse. Il modello ridotto è identificato utilizzando un approccio di identificazione di sistemi dinamici ed identificazione parametrica. Il modello finale che viene proposto consiste nella combinazione di un oscillatore di van der Pol forzato, per la modellazione delle azioni trasversali rispetto alla direzione del flusso, e di un modello lineare nello spazio di stato, per la modellazione delle azioni longitudinali rispetto alla direzione del flusso.

Il modello così sviluppo è applicato per lo studio di un modello flessibile in scale reale ed i risultati sono confrontati con esperimenti condotti all'interno di un vasca navale. Infine, per quanto riguarda l'oscillatore forzato di van der Pol l'identificazione parametrica è stata ripetuta modellando i parametri come variabili stocastiche. In particolar modo l'applicabilità del filtro di Kalman ensemble, per l'identificazione parametrica dell'oscillatore di van der Pol forzato, è discussa ed analizzata.

ZUSAMMENFASSUNG

In dieser Dissertationsschrift wird die Entwicklung eines reduzierten Modells (Reduced Order Model) zur Analyse von langen, flexiblen Zylindern im Hochseebereich vorgeschlagen. Der besondere Fokus liegt auf der Modellierung der durch Wirbel hervorgerufenen Vibrationen, und das Ziel ist die Entwicklung eines Modells, das in der Lage ist, sowohl Schwingungen in Richtung der Strömung als auch quer dazu abzubilden.

Das reduzierte Modell wird identifiziert mit den Ergebnissen eines hochgenauen Lösers, der durch die Kopplung eines Finite Elemente-Lösers mit einem Finiten Volumen-Lösers entwickelt wurde. Die hochgenaue Analyse wird auf einem beschränkten Gebiet durchgeführt, welches einen kleinen Abschnitt eines langen Zylinders repräsentiert, der dennoch flexibel ist.

Dem Zylinderabschnitt wird an den Enden eine Bewegung aufgezwungen, die der erwarteten Bewegung in der echten Größenordnung entspricht, und die Ergebnisse werden zur Systemparameteridentifizierung des reduzierten Modells genutzt.

Verschiedene reduzierte Modelle werden analysiert und ihre Resultate verglichen und diskutiert. Das reduzierte Modell wird durch eine System- und eine Parameteridentifizierung bestimmt. Das schließlich vorgeschlagene Modell besteht aus der Kombination eines erzwungenen van der Pol-Oszillators, womit die Querstromkräfte modelliert werden, und einem linearen Zustandsraummodell, um die Kräfte in Strömungsrichtung zu modellieren.

Das so entwickelte Modell wird auf ein flexibles Modell für die echte Größenordnung angewendet, und die Ergebnisse werden mit Experimenten in einem Schlepptank validiert. Schließlich wird die Parameteridentifizierung mit Hauptaugenmerk auf des van der Pol-Modell in probabilistischer Formulierung durchgeführt. Im Speziellen wird die Anwendbarkeit des Ensemble Kalman Filters zur Parameterschätzung des van der Pol-Oszillators diskutiert und analysiert.

To My Family

Acknowledgements

This work has been conducted partially at the University of Florence in Italy and partially at the TU Braunschweig in Germany. After three years of work it is not easy to list and to thank all the people that have contributed to the realization of this work.

Firstly I would like to thank my supervisors Professor Borri and Professor Matthies for their guidance over the last three and a half years. Every meeting with Professor Borri was always helpful and he was a really great support during my PhD activity. Professor Matthies taught me how to approach problems in a more rigorous and mathematical way: I still remember when during one of our first meetings he told me: *'You are not getting things, you are solving equations'*. He also taught me how to write a scientific text and every discussion with him was fruitful and inspiring. Among my unofficial supervisors I want to thank also Professor Oumeraci for the support and expert guidance he gave me at the beginning of my PhD activity.

I am also grateful to the "Regione Toscana" that financed my scholarship through the "Giovanisì" project and to the DAAD (Deutscher Akademischer Austasch Dienst) institution that gave me precious financial help during the last months of my activity.

A big thank you goes to all the German colleagues that always welcomed and helped me during my numerous stays at the Institute of Scientific Computing of the TU Braunschweig. In particular I would like to thank Rainer Niekamp, the developer of the CTL and C++ master, who helped me a lot with every technical matter during the development of the FSI solver, Martin Krosche who provided me the existing coupled solver and helped me with the development of my version of the FSI solver, Thorsten Grahs who introduced me to the world of OpenFOAM and always cleared up any doubts regarding the fluid part of my problem. A special thank you goes to my colleague and friend Bojana Rosic who helped me a lot with the part of my thesis regarding the parameter identification in a probabilistic setting and who always cheered me

up when I was lost or feeling down. I would like to thank also Cosima Meyer who took care of all the organisation during my stays in Germany.

I also want to thank all the people I met in Trondheim, Norway during my short stay at Marintek and Sintef. In particular I would like to thank Philippe Mainçon who received me and gave me advice during a crucial period of my PhD activity, Carl Larsen, one of the most renowned VIV experts, for his hospitality and for the suggestions he gave me about my work, Trond Kvamsdal for the inspiring comments he gave me during our discussion. Finally, a grateful acknowledgement to the Norwegian Deepwater Programme for making available the dataset I used for the validation of my model.

From the Italian side my gratitude goes to all the colleagues and friends of the international doctorate course with whom I shared all the good and bad feelings of being a PhD student and with whom I enjoyed the night-life during our German stays. Thank also to Serena Cartei, the secretary of our doctorate course who was always really helpful and went out of her way to solve any administrative issues.

Finally, I really want to express all my gratitude to all the people that have contributed indirectly to this work with their emotional support. First of all to my family, to whom this thesis is dedicated, you have always supported me in every choice I made since I started walking for the first time. To Sofia who has always believed in my ability and has always encouraged me every day and night when I was lost and I wanted to give up. To my waterpolo team-mates, my relief valve, who allowed me, at least during that one and a half hour inside the water, to completely clear my head. *To All of You, Thank you, Thank you, Thank you.*

Giovanni Stabile

Florence, Italy, February 2016

Preface

This thesis was submitted to the Department of Civil and Environmental Engineering of the University of Florence in Italy and to the Department of Architecture, Civil Engineering and Environmental Sciences of the TU Braunschweig in Germany, as a partial fulfilment of the requirements to obtain the PhD degree. The work presented was carried out in the years 2012-2016 partially at the department of Civil and Environmental Engineering of the University of Florence under the supervision of Prof. C. Borri and partially at the Institute of Scientific Computing of the Technical University of Braunschweig under the supervision of Prof. H.G. Matthies.

Thesis objectives

The main objective of this work is the development of a novel reduced order model for mooring lines, risers and in general for long cylinders in an offshore environment, accurate enough to capture complex phenomena such as vortex induced vibrations but with reasonable computational costs. The idea is to use the results of a high fidelity fluid-structure interaction solver in order to identify the main physical aspects of the problem and to study locally the hydrodynamics forces acting on the cable. The results of this solver are then used to create a novel reduced order model suitable for design purposes and for long term simulations.

Thesis outline

In ***Chapter 1*** a general overview of the problem and the motivations behind this work are given. In the first part of the chapter different applications in an offshore environment, where long flexible cylinders can be found, are presented. In particular, the review is focused on mooring lines and risers. Methods to treat the dynamics of long flexible cylinders are presented and the most important previous works on the topic are summarized and discussed. The second part of the chapter is focused on Vortex Induced Vibrations (VIV) problems that have proven to be one of the biggest open questions for these kinds of structures. Current methods for the prediction and the analysis of VIV phenomena are presented and discussed. In the last part of the chapter the method proposed in this thesis is explained and the motivations behind it are given and explained.

Chapter 2 explains how the fine scale model, on which the method is based, has been developed. It consists of the coupling of a finite element method (FEM) computational structural dynamics (CSD) solver with a computational fluid dynamic (CFD) solver. The coupling is realised using a partitioned approach. The partitioned approach allows the re-use of existing solvers, in particular for the fluid structure interaction problem the open source code OpenFOAM [62] and the open source code FEAP [118] are used for the fluid and for the structural parts respectively. The communication between different codes is realised using the approach of software components through the component template library (CTL) tool developed by Rainer Niekamp[89] at the Institute of Computing Science of TU Braunschweig. The fluid is solved by using an arbitrary Lagrangian-Eulerian[31, 49] (ALE) formulation while the structure is modelled through a geometrically-exact beam element as proposed by Simo[114]. Results of some preliminary analysis performed by the so developed solver are presented and discussed.

Chapter 3 presents and compares different reduced order models (ROMs) developed using the results obtained by the high fidelity simulations. The idea is to create a new element inside the structural solver which can be added to any CSD solver and which permits the calculation of the fluid forces with a reasonable computational cost. Using such an approach the fluid computation, which is the most computationally demanding part, can be dramatically simplified. The developed ROM is applied to reproduce a full-scale experiment conducted on a long flexible cylinder of 38m at the laboratories of the University of Trondheim in Norway. The structural model

is the same as the one used for the fine scale model and has been treated using a finite element approach. Fluid forces are evaluated by using the resulting reduced order model. Results of the simulations are compared with full scale measurements from the towing tank experiments.

In ***Chapter 4*** the identification procedure is repeated in a probabilistic setting. In particular, the applicability of the Ensemble Kalman Filter (EnKF) for the parameter estimation of the forced van der Pol oscillator, is studied and discussed.

The possible coupling between the developed model and a floating offshore wind turbine model, is presented in **Chapter 5**. Here the different sub-problems involved in the simulation of a floating offshore wind turbine are presented. A possible coupling strategy between the platform solver and the presented reduced order model is introduced and discussed.

Finally in ***Chapter 6*** the results of the whole thesis are discussed and some suggestions and indications for future works are proposed.

Contents

List of Abbreviations

ALE Arbitrary Lagrangian Eulerian

BEM Blade Element Momentum

$BIBO$ bounded-input, bounded-output

CF Cross Flow

CFD Computational Fluid Dynamics

CSD Computational Structural Dynamic

CTL Component Template Library

DC Drag Coefficient

$DFMT$ Direct Force-Motion Transfer

DNS Direct Numerical Simulation

EKF Extended Kalman Filter

$EnKF$ Ensemble Kalman Filter

$FPSO$ Floating Production, Storage and Offloading

FSI Fluid-Structure Interaction

IL In Line

KF Kalman Filter

LC Lift Coefficient

LES Large Eddy Simulation

$MIMO$ Multi Input Multi Output

PDF probability density distribution

PEM Predicton Error Method

$PISO$ Pressure implicit with splitting of operator

$RANS$ Reynolds Averaged Navier-Stokes

$ROMs$ Reduced Order Models

$SIMPLE$ Semi-Implicit Method for Pressure Linked Equations

$SISO$ Single Input Single Output

St Strohual Number

TLP Tension Leg Platform

VDP van der Pol

VIV Vortex Induced Vibrations

Chapter 1

General Overview

In this chapter a general overview regarding the dynamic analysis of long flexible cylinders in an offshore environment is presented. VIV phenomena are introduced and discussed.

Contents

1.1 Introduction

Due to the gradual depletion of oil and gas resources onshore and in shallow waters, recent years have seen an increasing interest in deeper waters, where a large proportion of the remaining oil and gas is located. The recent interest in deeper waters comes not only from the petroleum industry but also from the renewable energy sector. The sea, especially in deep waters, has a huge energy potential, which could be exploited using wave energy converters, solar power plants and wind turbines located on offshore platforms. Long slender cylinders are found in many offshore applications and are the representative system for mooring lines, risers, umbilicals and free spanning pipelines in deep water. The responses of these kinds of structures to wave, current and tide loads may be complex, and phenomena such as vortex induced vibrations (VIV), unsteady lock-in, dual resonance, and travelling waves response may occur [141]. Much progress has been made to understand the hydrodynamic forces that have to be used for these structures but an efficient and reliable model, especially dealing with vortex induced vibrations [107], is still missing in literature. Computational fluid dynamics (CFD) methods have been demonstrated to be a possible way of getting the response of flexible structures in an offshore environment, especially considering the increasing of the available computational power, but they are still not applicable to long-term simulations and to values of the Reynolds number interesting for practical applications.

Although in the future CFD methods will probably be the first choice for design purposes, at the moment we still have to rely on simplified and approximated methods mostly based on experimental activities conducted on rigid cylinders undergoing forced or free vibrations [107, 140, 139]. This contribution aims to develop a new time domain simplified method identified through high-fidelity FSI simulations conducted on flexible cylinders undergoing forced oscillations.

1.2 Long flexible cylinders for offshore applications

Slender and circular structures are used in many offshore applications such as mooring lines, risers, umbilicals and free spanning pipelines. In this thesis the attention is focused on mooring lines and risers and in this section an overview about this kind of structures is given. Different typologies of mooring lines and risers are presented and their characteristics are explained and discussed.

1.2.1 Mooring Lines

The mooring system ensures that a floating platform is kept in position. The station-keeping systems of a floating structure may be grouped into two main types: the mooring lines type and the caisson or pile-type dolphins. Only the first type becomes economically and technically feasible when dealing with deep waters [131]. Mooring lines are used in most offshore structures to keep the floating platform in position. Nowadays, most of the realized offshore platforms are used for the extraction of oil or natural gas, but during the last few years offshore platforms and especially very large offshore platforms have also been proposed for different purposes. They may also be used to create floating airports, bridges, wind and solar power plants, etc... The development of cost-effective designs is especially needed when dealing with offshore power plants in order to realize a technology that can compete with other energy sources. Mooring lines in deep water are exposed to hydrodynamic forces due to the relative motion between the water and the cables. Among all aspects mooring line dynamics represents one of the most uncertain one. Mooring lines can be classified into two different types: catenary systems and taut leg systems (see Figure 1.2). A review on different mooring line combinations can be found also in Childers [22, 23, 24].

CATENARY SYSTEMS utilize the horizontal force component of the mooring lines to provide restoring forces. Any movement of the platform increases the tension in the moorings and creates the restoring force. There are different types of catenary mooring systems: all chain, all wire and chain/wire systems (see Figure 1.1).

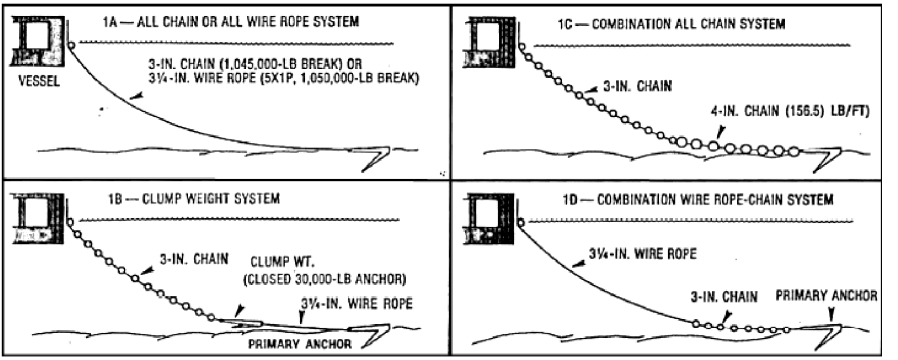

Figure 1.1: Different kind of mooring systems - Image taken from [22]

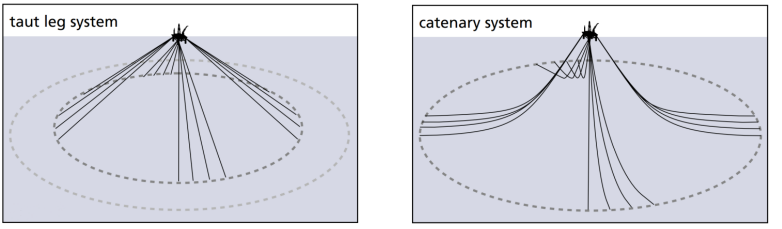

(a) Taut leg system **(b)** Catenary system

Figure 1.2: Different methods to provide restoring forces - Image taken from [129]

All chain systems in which the mooring lines are composed only by chain elements. The high weight of the chain produces, in this mooring system, a steep catenary with high vertical restoring forces and small horizontal ones. Small horizontal restoring forces allow the structure to undergo large displacements which could exceed the limiting design parameters. In deep water, the chain can become very heavy and this produces a high reduction in the load deck capacity and problems during deployment operations. For the above reasons chain systems are not feasible for deep-water structures.

All wire systems in which the mooring lines are composed only by wires. In this mooring system, the lower weight of wires produces a shallower catenary profile resulting in higher horizontal forces. The overall system is stiffer than a chain system, however, in presence of anchors, small vertical forces are allowed. In order to ensure the absence of vertical forces at the anchors, because of the small weight of wires, considerable lengths of wire lying on the ground

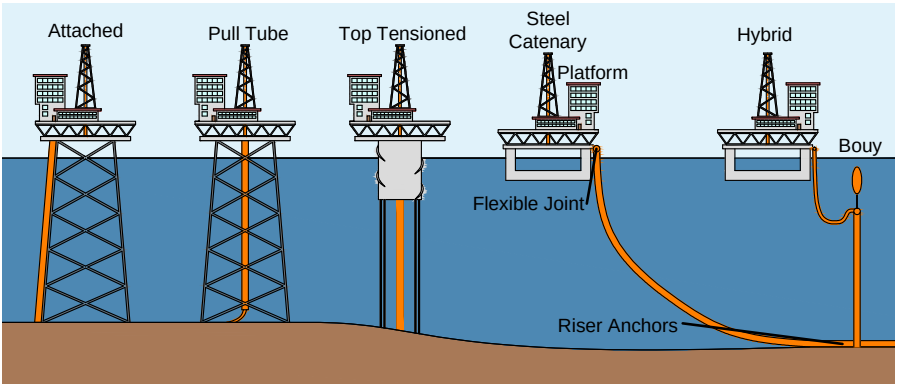

Figure 1.3: Examples of different riser systems

are required. For this reason, all-wire systems are not the best options for deepwater structures.

Chain/wire systems Chain/wire systems combine the advantages of both the previous systems. The wire section forms the upper part of the mooring producing a shallow catenary profile with a good horizontal restoring force while the chain section is used in the lower part ensuring enough weight which lies on the ground.

TAUT LEG SYSTEMS require an anchor that can resist high vertical forces and they generate an overall system which is very stiff to vertical motion. In a taut-leg system, where the wires are normally not vertical, the anchor points are subjected to vertical and horizontal forces. The taut leg system has a much more linear stiffness than the catenary system. The disadvantage of the taut-leg system is that the mooring line must have sufficient resistance to absorb the vessel wave motions without overloading.

1.2.2 Risers

Risers are common structures in offshore engineering and are extensively used for oil and gas exploitation in marine environments. They are conduits used to transfer materials from the seabed to the drilling facility [6, 7, 61]. It is possible to find a variety of different types of configuration depending on the

kind of platform located on the sea surface (Figures 1.4, 1.5) and on the water depth. They can be classified into the following different categories (depicted in Fig. 1.3):

- **Attached and Pull Tube Risers** are used on fixed structures and are directly linked to the support structure. In the attached type the riser pipeline is directly clamped to the supporting tower while pull tube risers are pulled inside a wider tube, normally pre-constructed in the centre of the tower from the seabed to the platform.
- **Steel Catenary Risers** are normally used in deep-water conditions with Tension Leg Platforms (TLP), Floating Production Storage and Offloading (FPSO) units and spars platforms. The steel pipeline hangs freely from the platform and it is connected to it with a flexible joint. Although this kind of structure, due to its dimension, has a considerable bending stiffness, the word catenary is used because the pipeline forms a catenary shape between the hanging point on the platform and the seabed.
- **Top Tensioned Risers** are vertically oriented risers which are normally used with tension leg and spar platforms. On their top, a tension which excises the apparent weight is applied to provide stability. Since the tension increases with the water depth these structures are used only with moderately deep waters.
- **Hybrid Risers** are a combination of a vertical riser and a flexible riser. They consist of a vertical bundle where the tension is provided by external buoyancy; the fluid is transported to the production platform from the top of the vertical bundle using flexible jumpers.

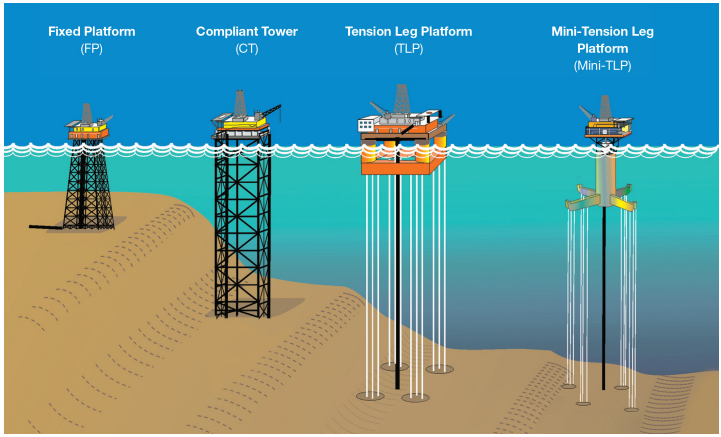

Figure 1.4: Different Platform Configurations for shallow and intermediate waters - Image taken from [99]

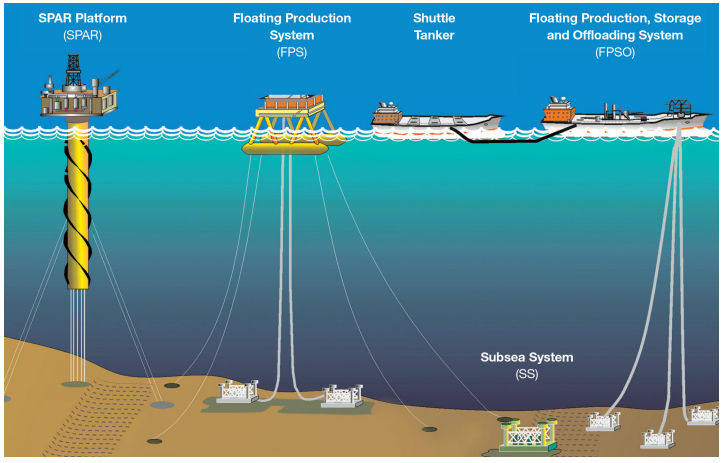

Figure 1.5: Different Platform Configurations for deep waters - Image taken from [99]- Image taken from [99]

1.3 Dynamic analysis methods

In literature two different approaches for the treatment of long flexible cylinders in an offshore environment are found: the frequency domain approach and the time domain approach. The choice between the different methods requires a compromise between computational effort and accuracy.

1.3.1 Frequency domain methods

These approaches are based on the linearity of the system. When a linear system is subjected to a Gaussian input it produces a Gaussian output. This means that the statistical properties of the response process can be derived from the response spectrum. The random sea, for small value of the wave steepness $\frac{H}{L}$, can be approximated with a Gaussian process with zero mean. For this reason, the frequency domain approach can be used to analyse a large number of offshore structures. In the above expression H is the wave height and L is the wave length. For further details about frequency domain methods one may see many textbooks and lecture notes on hydrodynamics [66, 88].

1.3.2 Time domain methods

Although frequency domain methods are relatively simple and can lead to a good estimation of the structural response, in most applications a time domain solution is necessary. A comparison between the main features of the two methods are shown in Table 1.1 taken from [8]:

	Frequency domain methods	Time domain methods
Assumptions:	Linear or quadratic dynamic system	Linear or non-linear dynamic system
	Stationary process	Stationary or not stationary processes
	Gaussian process	Gaussian or non-Gaussian processes
Results from:	Mean, standard deviation, zero crossing period and probability density function	Sampling of the random process time history

Table 1.1: Comparison between different analysis methods - Table taken from [8]

A general review on time domain methods, that inspires this overview can be found in [40]. The sea environment is generally a random, non-stationary and non Gaussian process. This means that the principle of superposition of different regular waves is not applicable. Time domain methods can accurately describe the real physical process with more accurate results than frequency

domain methods. The main drawbacks of time domain methods are related to the need to solve a nonlinear problem at each time step; furthermore each solution represents a realisation of just one of the process responses. In order to obtain maximum value of the response it is necessary to perform a huge number of different realizations. Different numerical methods can be classified with respect to the different method used to discretize the system in space and to discretize the system with time. While in time discretization there is universal agreement on the method (finite differences) one can find different approaches for the space discretization. The most common methods that one can find in literature are: finite differences, finite elements and lumped elements. Apart from these differences there are distinctions regarding different mathematical and physical features which may be incorporated in the model such as: bending stiffness, seabed interaction and hydrodynamic loadings. Different methods also differ in the procedure used for time integration. Most of the research done on flexible cylinders during last decades comes from the petroleum industry where mooring lines and risers are used in conjunction with oil platforms. Walton and Polachek[130] pioneering work presented the first treatment of the dynamic solution. They formulated the equation of motion using discrete elements with concentrated mass at the element nodes. This approach is now categorised as lumped parameter method. Recent models making use of this approach can be found in Huang[52] and Thomas[119], in these works the emphasis is given to the cable-seabed interaction. Gobat, in his PhD thesis [41] and in a more recent article [40] analysed a geometrically compliant mooring system with a finite difference method and reported a thorough review of mooring lines models since 2006. He assessed seabed interaction and VIV problem as the most interesting field of research on mooring lines and proposed a new model to treat cable-seabed interaction. Palm et al [92] recently used a discontinuous Galerkin finite element method for mooring lines dynamics. Bending stiffness and torsional stiffness are not included in the model and hydrodynamic forces are modelled using Morison's equation while ground interaction is made up of a bilinear spring and damper system. The developed model is also compared with experimental results showing good agreement. None of the previously cited articles deal with vortex induced vibrations (VIV) or use a hydrodynamic model other than Morison's equation. Most of the research dealing with mooring lines is focused on developing simple hydrodynamic models in order to be manageable and to be easily coupled with a platform model. Here only some of relevant and general contributions are proposed but in summarising the entirety of the research analysed the

following conclusions can be drawn:

- With the arrival of modern computers and nowadays-computational resources complex and accurate structural models have been proposed and can be solved with a reasonable effort. The *structural* part of the problem is one of the most certain: by *structural* it is intended here the determination of the response of a certain structure under some known load conditions.
- The determination of the loads acting on the structure and the interaction between the entity of these loads and the structural response is still an open question. Loads acting on the structure, such as fluid-structure interaction forces or seabed-structure interaction forces, depend on the structural response making the coupled problem complex and highly nonlinear.
- Among fluid-structure interaction phenomena the VIV problem is one of the most complex and commonly-studied. Although a lot of research has been published over the years a definitive and reliable method is still missing in literature [107, 140, 139, 20, 141].

In the next section an overview regarding the VIV problem is given and current methods for the analysis and prediction of hydrodynamics forces, due to the VIV phenomena, are explained and discussed.

1.4 VIV phenomena

This section is dedicated in particular to VIV problems. Long flexible cylinders in an offshore environment are often exposed to the phenomena of vortex-induced vibrations (VIV). VIV are an important phenomenon in many different engineering fields and have been studied in either air or water for many years. The content of this section is summarized from the numerous reviews on the topic available in literature [139, 140, 107, 141, 37]. This phenomenon is caused by the oscillating flow arising from the alternate vortex shedding. Among all possible existing phenomena that may happen on flexible cylindrical structures in an offshore environment, VIV are one of the most dangerous and hard to predict. If a rigid and fixed cylinder is considered, the frequency of the vortex

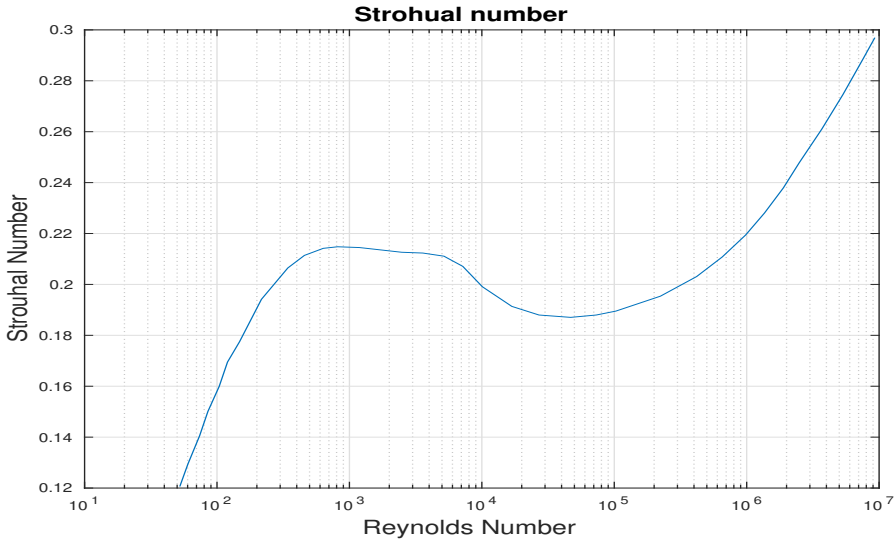

Figure 1.6: Strouhal Number vs Reynolds Number for a circular cylinder - Image created by the author using the data taken from [42]

shedding phenomenon follows the Strouhal law [117]:

$$St = \frac{f_v D}{U} \tag{1.1}$$

in which St is the Strouhal number, f_v is the frequency of the vortex shedding, and U is the free stream velocity. For a rigid and fixed circular cylinder the Strouhal number, over a certain range of the Reynolds number, assumes a constant value approximately equal to 0.2 as depicted in Figure 1.6. In this range of values, which are particularly interesting for practical applications, the relationship between the free stream velocity and frequency of oscillation is linear. Conversely, if it is considered a cylinder which is free to vibrate or forced to move the phenomenon does no longer obey the Strohual law (Figure 1.7). When the vortex shedding frequency approaches the natural frequency the so called lock-in phenomenon is observed. The synchronisation of the vortex shedding frequency to the frequency of oscillation occurs over a certain range of the flow velocity. In this range the vortex shedding phenomenon is driven by the frequency of oscillation of the cylinder. Although a lot of research has been performed in this field, three basic different methods to predict the behaviour of a slender cylinder subjected to VIV can be found:

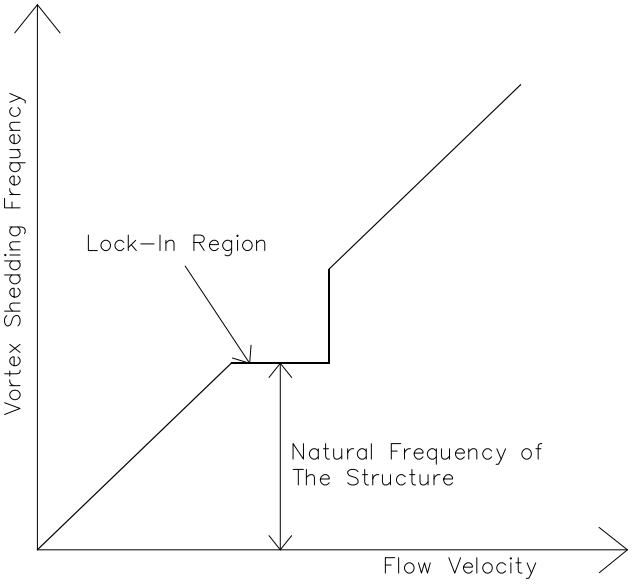

Figure 1.7: Qualitative trend of vortex shedding frequency with flow velocity during lock-in - Image re-adapted from [112]

- Semi-empirical models
- Navier-Stokes models
- Simplified wake models

Here the methods are only briefly introduced and discussed A comprehensive review regarding these different approaches and a comparison of their results can be found in Chaplin et al. [20].

1.4.1 Semi-empirical models

These methods are widely used by numerous authors and are nowadays the standard for many commercial codes used in offshore engineering such as VIVA [122, 142], VIVANA [74, 75], SHEAR7 [125, 127]. The instantaneous amplitude of oscillation is evaluated using appropriate force coefficients. These are evaluated on experimental tests on rigid cylinders undergoing free or forced vibrations. The assumption of only cross flow motion is made. In this approach the response of the structure is evaluated in frequency domain and it is normally assumed that the cylinder is oscillating only in cross-flow direction.

Within this method, natural frequencies of the structure are evaluated and than the modes which are most likely to be excited by the vortex shedding are identified. Normally only the steady in line response of the structure is identified. The main limitation of this category of models is that they make the assumption of only cross-flow motion and, since they operate in the frequency domain, they are not able to capture non-linearities. These tools also make the assumption of a harmonic motion and the solution is given by a superposition of different oscillation modes.

1.4.2 CFD models

In CFD methods the flow field around the cylinder is computed by solving numerically the Navier-Stokes equations. Bourget et al. [10, 9] proposed a full three dimensional analysis of a long flexible cylinder. In these works the authors coupled a structural code with a CFD solver with direct numerical simulation of three dimensional Navier-Stokes equations, and the structural response is investigated. Boyer et al in [12] used a geometrically-exact beam model for the coupling with a CFD code which solves the unsteady incompressible Reynolds-averaged Navier-Stokes equations enabling vortex induced vibration configurations to be handled. In his PhD thesis, Huang[53] investigated the vortex shedding on a riser. He used a direct FEM integration solver for the structural dynamic and an unsteady incompressible Navier-Stokes solver with a LES turbulence model for the fluid dynamic. A complete review on numerical methods for VIV is also presented in his thesis. In [1] Akhtar performed several high-fidelity CFD analyses with Navier-Stokes DNS methods in order to represent the flow field with few dominant modes using a POD. The emphasis is here given to the control of VIV using fluid actuators. In the article only low Reynolds number flows are investigated. In [38] Gallardo et al. applied POD, after several high-fidelity CFD analyses, in order to condense the information contained in the flow field into a limited set of modes. When summarising the whole of the cited works, CFD methods can be classified into two different classes:

- **Full 3D simulations** where the flow is discretized using 3D elements [9, 11, 10, 50]. This approach has the advantage of completely capturing the three-dimensionality of the flow, but even with today's computational resources this is too demanding for the case of long cylinders and for flows with realistic values of the Reynolds number.

- **Strip theories** where the flow is modelled using bidimensional analysis at several different positions along the cable length. The flow at different planes is completely independent [72, 47, 108, 135, 136] and the three-dimensionality is only due to the structural model. This approach is computationally less demanding, and flow with realistic values of Reynolds number can be simulated. The disadvantage is that the three-dimensionality of the flow cannot be captured and forces at different planes have to be interpolated, and it is not easy to find a general way to perform such an interpolation.

DNS CFD methods, even if have been used, are not suitable for riser VIV simulation. Contributions where DNS methods are used always consider a small Reynolds number which is not compatible with real conditions. RANS and LES CFD methods demonstrated to be suitable to study VIV effects on short rigid cylinders, even for higher Reynolds numbers, but in case of long flexible cylinders they are still computationally too demanding and for this reason they cannot be used for design purposes where a large number of simulations are needed. The analyses are performed for a relatively small value of the Reynolds number or for small value of the length ratio. Moreover, these approaches require high computational resources and long computational times which make theme unsuitable for design purposes. To give an idea of the computational cost of a full 3D-dimensional simulation, we refer here to Bourguet [10]. He conducted a DNS CFD analysis on a long flexible cylinder ($L/D = 200$) at $Re = 1100$ on a 512 cores computer. The simulation time for each time step resulted to be approximately equal to 3s and considering that a cross-flow vibration cycle counted 13000 time steps this would led to a simulation time approximately equal to 11h for each vibration cycle.

1.4.3 Simplified wake models

These models, instead of completely solving the flow field, model the flow forces using simplified models. The 3-dimensionality of the problem is reconstructed using a strip theory. Most of the simplified model present in literature are able to predict only the hydrodynamic forces for the cross-flow direction [80]. The fluctuating value of the drag is normally not considered and when taken into account is supposed to be independent from the lift coefficient [35]. Large parts of the proposed models are based on the idea of the wake oscillator [106]. In this approach, the dynamics of the wake behind the cylinder is modelled by one

single variable which is supposed to satisfy a non-linear differential equation which is self-excited and self-limited. For this purpose, systems normally used to model vortex shedding on static cylinders, such as the Rayleigh (Eq. 1.2) [44] or the van der Pol (Eq. 1.3) equations, are extended [35, 116] with a forcing term depending on the motion of the cylinders:

$$\ddot{l} + \omega_s^2 l - \mu_r \dot{l} + \alpha_r \dot{l}^3 = F(d, \dot{d}, \ddot{d}) \tag{1.2}$$

$$\ddot{l} + \omega_s^2 l - \mu_v \dot{l} + \alpha_v l^2 \dot{l} = F(d, \dot{d}, \ddot{d}) \tag{1.3}$$

in which l is the lift coefficient, ω_s is the vortex shedding frequency for a stationary cylinder, μ_r, μ_v and α_r, α_v are the linear and non-linear damping terms identified respectively for the Rayleigh and the van der Pol equation, and F denotes a forcing term which couples the structural motion and the wake oscillator equation. This forcing term differs among different authors but it usually depends linearly on acceleration, velocity or displacement along the considered direction. Harrie and Currie [44] proposed a Rayleigh wake oscillator. The structure is represented by a 1-DOF elastically mounted rigid cylinder, modelled as a linear damped second order dynamical system. The coupling term is in this case proportional to the transverse cylinder velocity:

$$\ddot{l} + \omega_0^2 l - \mu\omega_0 \dot{l} + \frac{\alpha}{\omega_0} \dot{l}^3 = B\dot{y} \tag{1.4}$$

Facchinetti et al. [35] coupled a 1-DOF structural oscillator, free to vibrate only along the cross flow direction, with a van der Pol wake oscillator. In his work different coupling terms are analysed and it is assessed that the configuration which gives the best results is the acceleration coupling model:

$$\left(m_s + \frac{1}{4}\pi C_M \rho D^2\right)\ddot{Y} + \left[r_s + \gamma 2\pi \mathrm{St}\frac{U}{D}\rho D^2\right]\dot{Y} + hY = \frac{1}{4}\rho U^2 D C_{L0} q \tag{1.5}$$

$$\ddot{q} + \varepsilon\left[2\pi\mathrm{St}\frac{U}{D}\right]\left(q^2 - 1\right)\dot{q} + \left[2\pi\mathrm{St}\frac{U}{D}\right]^2 q = \frac{A}{D}\ddot{Y} \tag{1.6}$$

in which Eq. 1.5 and 1.6 represent the structural and the wake oscillator respectively. C_M, St, γ, C_{L0}, ε, A are parameters to be determined using experimental activities. Y is the dimensional cross-flow displacement, D is the diameter of the cylinder, m_s is the mass of the structure, r_s is the structural damping, h is the stiffness of the supports, U is the flow velocity. q is a dimensionless wake variable associated with fluctuating lift of the structure. Less research has been performed concerning the in-line displacements and

the hydrodynamic forces for the in-line direction. Nayfeh et al. [87] modelled the lift coefficient using a standard van der Pol oscillator and for the drag, considering that the fluctuating frequency of hydrodynamic forces along the in-line direction is twice the cross-flow frequency, used a quadratic coupling between lift and drag in a Reynolds decomposition setting:

$$d = d_m - Kl\dot{l} \tag{1.7}$$

in which K is a coefficient that must be determined experimentally and d and d_m are respectevely the total and fluctuating drag coefficients. Srinil and Zanganeh [116] proposed to model both the cross-flow and in-line fluctuating hydrodynamic forces using a van der Pol wake oscillator. The structure is modelled with a 2-DOF double Duffing oscillator. For the forcing of the van der Pol oscillator they used the structural transversal acceleration for the cross-flow direction and the acceleration along the direction of the flow for the in-line direction. Mainçon [80] proposed a model allowed to capture the chaotic response of marine structure under VIV. For each cross-section recent velocity history is compressed using Laguerre polynomials. The instantaneous velocity is used inside an interpolation function carried out using experimental activities. The recent trajectory is described so that it is more precise for the immediate past and becomes less precise further back in time.

1.4.3.1 Conclusions on the literature review

After the revision regarding VIV problems on long flexible cylinders some conclusions can be drawn:

- CFD methods showed to be a promising way to get the response of slender cylinders in an offshore environment. CFD simulations easily permits the changing of physical parameters and give more flexibility with respect to "real" experimental activities. Unfortunately, the available computational power is still not enough to perform accurate and reliable simulations in full scale, especially for realistic values of the Reynolds number [53, 10, 135].
- Semi empirical models based on simplified harmonic oscillators, although they are are the most used for design activities, have several drawbacks. The motion is supposed to be along only the cross flow direction but it is now well known that VIV phenomena are characterized by an oscillation

along both directions. In-line oscillations contribute strongly to fatigue loads since they are normally at twice the frequency respect to cross-flow oscillations. The neglect of in-line oscillations may lead to big errors during the fatigue loads prediction. The motion is also supposed to be harmonic and evidence shows that, in general, especially for flexible cylinders, the motion is not harmonic [141, 140].

- Simplified non-linear wake models showed ability to reproduce some features of the VIV phenomena but a definitive model still needs to be developed [37, 141].

A simplified time domain model which is able to predict both the in-line and the cross-flow oscillations in a relatively accurate manner is still missing in literature. The identification of the parameters of the simplified models has always always been conducted using results from rigid cylinders forced to oscillate only along the cross-flow direction. The effect of the flexibility of the cylinder, on the determination of the hydrodynamic forces, is not considered in the identification procedure. Although, strip theory with bi-dimensional CFD analysis at each plane are used in literature, in order to capture the three-dimensionality of the turbulence in the wake it is necessary to use a three-dimensional CFD simulation. In fact, bi-dimensional simulations, as stated by Shur et al. [111], may lead to incorrect results in the prediction of drag and lift forces. Moreover, since LES CFD simulations are used through the thesis, bi-dimensional simulations would not be the best choice. Bi-dimensional LES are in fact physically incorrect, because it would mean that one is modelling large eddies in 2-D while their behaviour is very much three-dimensional.

1.5 Introduction to the present method

The method proposed in this thesis aims to exploit both the advantages of CFD methods and of simplified wake models. The response of a piece of flexible cylinder is studied only locally, on a reduced domain size. The limited size of the domain permits to use a complete three-dimensional analysis with values of the Reynolds number suitable for practical applications. The logical process on which the present method is based is explained in Figure 1.8. The local model of the cable, henceforth called the fine-scale model or the high-fidelity model, is subjected to an imposed motion which matches the statistical properties of the expected motion in full scale. The reaction forces at the

ends of this model are measured. The results of these high-fidelity simulations together with the correspondent input motion can be used to feed a system identification technique which permits the definition of a reduced order model. Once the reduced model is identified one can create a new finite element which contains additional degrees of freedom that consider the hydrodynamic forces. The resulting developed model can be added to any computational structural dynamic solver.

Figure 1.8: Flowchart of the proposed method

Chapter 2

The Fine-Scale Model

In this chapter the fine-scale model is presented and explained. The methods used to developed the FSI solver are introduced and explained. A validation of the CFD solver and some preliminary analyses using the FSI solver are presented.

Contents

The method presented in Chapter 1 is strongly based on the used fluid-structure interaction solver. A large proportion of the work conducted for the preparation of this thesis is dedicated to development of this solver. The interaction between the structure and the fluid is a coupled problem and in the next sections it will be explained how it is solved in the context of this thesis. In this thesis the solid problem is solved using a finite element method [143, 56] while the fluid problem is solved using a finite volume method [128, 3]. Several simulations are performed but they all have some common features which are reported here.

2.1 The Coupled Problem

The coupled problem is solved here using a partitioned strategy with a so called [104] direct force-motion transfer (DFMT) method. In general, a fluid-structure interaction problem is formed by three different sub-problems [14, 13]: the fluid problem, the solid problem, and the mesh motion problem. The structural problem will be henceforth indicated with s while the fluid problem will be indicated with f. The solid problem is governed, in an Eulerian frame, by the momentum balance equation in terms of Cauchy stresses:

$$\boldsymbol{\nabla} \cdot \boldsymbol{\sigma} + \rho_s(\boldsymbol{b} - \ddot{\boldsymbol{u}}) = \boldsymbol{0} \text{ in } \Omega_s \times [0, T] \tag{2.1}$$

in which $\boldsymbol{\sigma}$ is the Cauchy stress tensor, ρ_s is the solid density, $\boldsymbol{b}$ is the body force vector, $\ddot{\boldsymbol{u}}$ is the acceleration vector. Ω_s is the structural domain, and T is the length of the considered time window. The water is modelled as a Newtonian, incompressible, viscous, isothermal and isotropic flow. Since the fluid domain is not static but changing in time due to the deformation of the solid body one needs to reformulate the Navier-Stokes equation for incompressible and viscous flows considering the motion of the FSI interface. This is done using an arbitrary-Lagrangian-Eulerian (ALE) [31, 32] framework referenced to a frame moving with a velocity $\boldsymbol{v_m}$. One needs to replace the convective term inside the velocity $\boldsymbol{v}$ with the convective velocity $\boldsymbol{v_c} = \boldsymbol{v} - \boldsymbol{v_m}$, where $\boldsymbol{v_m}$ is the velocity of the moving part of the domain The momentum balance equation and the continuity equation, for the fluid domain, can be

written in an Eulerian frame as:

$$\begin{aligned} \frac{\partial \boldsymbol{v}}{\partial t} + (\boldsymbol{v_c} \cdot \boldsymbol{\nabla})\boldsymbol{v} - \nu \boldsymbol{\nabla}^2 \boldsymbol{v} = & \quad -\tfrac{1}{\rho_f}\boldsymbol{\nabla} p \quad \text{in } \Omega_f \times [0,T] \\ \boldsymbol{\nabla} \cdot \boldsymbol{v} = & \quad \mathbf{0} \quad \text{in } \Omega_f \times [0,T] \end{aligned} \tag{2.2}$$

in which $\boldsymbol{v}$ is the flow velocity vector, t is the time, ν is the flow viscosity, and p is the pressure. Ω_f is the fluid domain, and T is the length of the considered time window. In the present work the solid and the fluid problem are solved using different space discretization techniques. The solid problem is solved using finite elements [143, 56], while the fluid problem is solved using finite volumes [128, 3]. The mesh motion problem is solved imposing the matching of velocities and stresses at the FSI interface:

$$\begin{aligned} \boldsymbol{v_s} = \boldsymbol{v_f} \text{ on } \partial\Omega_{FSI} \times [0,T] \\ \boldsymbol{n} \cdot \boldsymbol{\sigma} = -p\boldsymbol{n} + 2\nu(\boldsymbol{n} \cdot \boldsymbol{\nabla^S})\boldsymbol{v_f} \text{ on } \partial\Omega_{FSI} \times [0,T] \end{aligned} \tag{2.3}$$

where $\boldsymbol{n}$ is the vector normal to the FSI-interface and, $\boldsymbol{\nabla^S}$ is the symmetric part of the gradient operator. The matching of variables at the interface is enforced with an implicit scheme which conserves the energy at the interface. For each time step of the coupled simulation $t_{c,i}$ an iterative cycle on the velocity residual is performed until the achievement of a desired tolerance:

$$\boldsymbol{res} = \boldsymbol{v_{s,i}} - \boldsymbol{v_{f,N}} \leq TOL \tag{2.4}$$

The iterative scheme is realized using a block Gauss-Seidel procedure reported in Algorithm 1 [82]. In the algorithm T_0 is the initial time, T is the simulation time, Δt_f, Δt_s and Δt_c are the the time step of the fluid, solid and coupled simulation respectively, TOL is the tolerance that defines the maximum allowed value of the residuals $\boldsymbol{res^{(k)}_{N+1}}$. In the algorithm the subscript defines the N^{th} time step while the superscript defines the k^{th} sub-iteration. The starting point of the algorithm is the prediction of the fluid velocity $\boldsymbol{V^{(0)}_{f,N+1}}$ at the FSI interface based on the previous converged values of the velocity at the interface $\boldsymbol{V^{(k_{max})}_{N}}$, $\boldsymbol{V^{(k_{max})}_{N-1}}$, etc. For values of the subiteration index $k > 0$ the Aitken's relaxation factor ω is evaluated using the expression reported in the algorithm. The fluid problem is then solved and the fluid forces $\boldsymbol{F^{(k)}_{f,N+1}}$ acting on the FSI interface are determined. These are applied on the structure and the solid problem is solved in order to determine the velocity of the solid points at the interface $\boldsymbol{V^{(k)}_{S,N+1}}$. The residual $\boldsymbol{res^{(k)}_{N+1}}$ is evaluated as the

difference between the solid and fluid velocities at the interface. Finally the predicted value of the fluid velocity at the interface is updated using the new determined solid velocity at the interface and the evaluated Aitken's relaxation factor.

The time step size of the fluid sub-problem may differ the time step size of the solid sub-problem. The only requirement is that each sub-problem has to be performed the sufficient number of times necessary to reach the time step size of the coupled simulation. Inside the algorithm the term ω is a scalar value obtained by Aitken's relaxation [71]. The Aitken's relaxation factor is used to speed up the computation but the coupling algorithm also works with a constant relaxation value. This procedure works with any CFD solver and any CSD solver which can be coupled properly; here the solid sub-problem is solved using the FEM solver FEAP [118], while the fluid sub-problem is solved using the FVM solver OpenFOAM [62]. The coupling is realized using the approach of software components and the component template library (CTL) [82] is used as common middleware. Here the features of the FSI solver are only briefly reported: for additional details please refer to [57]. As already mentioned in this thesis, the solid and the fluid problems are solved independently and then coupled together using the explained coupling algorithm. In the next subsections a brief overview on how the two sub problems are solved is reported.

2.1.1 The Fluid Sub-Problem

The starting points for the solution of the fluid problem are its governing equations which were briefly introduced in Subsection 2.1. A Newtonian, incompressible, viscous and isothermal flow is considered so the problem is fully described by Navier-Stokes equations for incompressible flows which consist of the equations of conservation of momentum and conservation of mass. Here the strong form of these equations is reported in an Eulerian description:

$$\begin{aligned} &\frac{\partial \boldsymbol{v}}{\partial t} + (\boldsymbol{v_c} \cdot \boldsymbol{\nabla})\boldsymbol{v} - \nu \boldsymbol{\nabla}^2 \boldsymbol{v} = -\frac{1}{\rho_f}\boldsymbol{\nabla} p && \text{in } \Omega_f \times [0,T] \\ &\boldsymbol{\nabla} \cdot \boldsymbol{v} = \boldsymbol{0} && \text{in } \Omega_f \times [0,T] \end{aligned} \tag{2.5}$$

Algorithm 1 Coupling algorithm

Given: initial time T_0, length of the simulation T, time step size of the fluid simulation Δt_f, time step size of the solid simulation Δt_s, time step size of the coupled simulation Δt_c, the tolerance TOL

while $t < T$ **do**
  $k = 0, \omega^{(0)} = \omega_0$
  while $\boldsymbol{res}_{N+1}^{(k)} < TOL$ **do**
    if $k = 0$ **then**
      Predict fluid v. at the inter.: $\boldsymbol{V}_{f,N+1}^{(0)} = P(\boldsymbol{V}_N^{(k_{max})}, \boldsymbol{V}_{N-1}^{(k_{max})}, \dots)$
    else
      $\omega^{(k)} = -\omega^{(k-1)} \frac{\boldsymbol{res}_{N+1}^{(k-1)} \cdot (\boldsymbol{res}_{N+1}^{(k)} - \boldsymbol{res}_{N+1}^{(k-1)})}{\left\| \boldsymbol{res}_{N+1}^{(k)} - \boldsymbol{res}_{N+1}^{(k-1)} \right\|^2}$
    end if
    Given $\boldsymbol{V}_{f,N+1}^{(k)}$ solve the fluid problem in ALE formulation $\rightarrow \boldsymbol{F}_{f,N+1}^{(k)}$
    Given $\boldsymbol{F}_{f,N+1}^{(k)}$ solve the solid problem $\rightarrow \boldsymbol{V}_{S,N+1}^{(k)}$
    Evaluate residual $\boldsymbol{res}_{N+1}^{(k)} = \boldsymbol{V}_{S,N+1}^{(k)} - \boldsymbol{V}_{f,N+1}^{(k)}$
    Update fluid velocity at the interface $\boldsymbol{V}_{f,N+1}^{(k+1)} = \boldsymbol{V}_{S,N+1}^{(k)} + \omega^{(k)} \boldsymbol{res}_{N+1}^{(k)}$
    $k = k + 1;$
  end while
  $N = N + 1, t = t + \Delta t_c$
end while

2.1.1.1 Boundary Conditions

Navier-Stokes equations form a system of partial differential equations that in order to have a full mathematical description must come together with its relative boundary conditions. In CFD boundary conditions play a crucial role not only from a mathematical point of view but also from a physical one [3, 26, 128]. In fact, they describe important macroscopic and microscopic effects that are considered as the engine of the motion. Here most important kinds of boundary conditions used through the thesis are explained and discussed.

DIRICHLET CONDITIONS are used to prescribe the value of a certain quantity on a boundary. They are normally applied on both the velocity and the pressure field. At the outlet when one is considering a fully developed flow a constant zero pressure is prescribed while a velocity profile is normally

prescribed at the inlet. Among them one can find some boundary conditions that have a particular physical meaning:

- **NO-SLIP CONDITION** is normally applied to all kind of obstacles which lie inside the computational domain. This condition is also used to simulate the case of a body which is moving inside a fluid with a certain velocity. Normally in an Eulerian description it is more convenient to describe the body as it would be at rest and to impose that the velocity of the fluid at the inlet, far from the body, is equal to the opposite of the velocity of the body. In the case studied in the thesis this condition is applied to the cylinder. This condition can also be applied to the case where a body is moving inside the computational domain with a certain velocity. If considered on a body domain Ω_b which moves with a certain velocity $\boldsymbol{v_b}(t)$ is of the form:

$$\boldsymbol{v}(t) = \boldsymbol{v_b}(t) \text{ on } \partial\Omega_b \tag{2.6}$$

  This condition is used when viscous effect are considered. It physically means that, because of viscosity, fluid particles are stuck on the body surface and have exactly the same velocity as the body.

- **SLIP CONDITION** is a Dirichlet boundary condition used to simulate obstacles when viscous effects are not considered. Only the velocity normal to the surface of the body is prescribed. This condition is also used for symmetric purposes when it is simulated only a reduced part of the domain and one wants to artificially recreate the remaining part of the domain. In the case studied in the thesis this condition is applied to upper and lower part of the domain and if considered on a body domain Ω_b which moves with a certain velocity $\boldsymbol{v_b}(t)$ is of the form:

$$\boldsymbol{v}(t) \cdot \boldsymbol{n} = \boldsymbol{v_b}(t) \cdot \boldsymbol{n} \text{ on } \partial\Omega_b \tag{2.7}$$

NEUMANN CONDITIONS are boundary conditions where the gradient of a certain quantity is prescribed in a direction normal to the considered boundary. They are normally applied to both velocities and pressure:

- **ZERO GRADIENT CONDITION** is used to simulate fully developed flow. This is a Neumann boundary condition applied on the gradient of the considered quantity. It prescribes the gradient of a certain quantity.

In the following equation, for example, the velocity, across the considered boundary is equal to zero:

$$\nabla \boldsymbol{v} \cdot \boldsymbol{n} = \mathbf{o} \tag{2.8}$$

This condition is often applied to model outflow conditions. In most cases it is practically impossible to simulate the whole domain, and for this reason only a certain part of the domain is considered and one assumes that far from the obstacle the flow is fully developed and the gradient of the velocity is zero. This condition is used here for the velocity at the outlet and for the pressure at the inlet and at the cylinder surface.

2.1.1.2 Discretization of the Navier-Stokes equations

In order to solve numerically the Navier-Stokes equations one has to rewrite them in a discretised form so that they can be transformed into a system of algebraic non-linear equations that can be solved using established numerical methods. The discretisation of the Navier-Stokes equations can be performed in different ways [95, 3, 26, 128]:

- **Finite Differences**: the strong form of the Navier-Stokes differential equations is transformed into a difference equation where derivatives are approximated with finite differences. This approach is also often used for CFD problems and it works better on structured grid and the method is not exactly conservative [25].
- **Finite Volumes**: the weak form of the Navier-Stokes equation is discretised and the integration domain is taken to be a control volume Ω_i associated to a point with coordinate $\boldsymbol{x_i}$ normally located in the centre of the control volume. The whole domain is then decomposed into many control volumes where each integral is evaluated numerically. This approach is particularly suited for fluids because it produces a conservative scheme if the flux on the boundary of one cell equals the flux on the boundary of the adjacent cell (see Versteeg [128]).
- **Finite Elements**: the weak form of the equations is also the starting point here. The domain is discretised into N subdomains and one

assumes that the solution is represented by:

$$v = \sum_{j=1}^{B} N_j(x) v_j(t) \tag{2.9}$$

where $v(j)$ are the nodal variables depending only on time and N_j are trial functions which are normally represented by low order polynomials. Then the weak form of the equation can be integrated over the domain and multiplied by a proper set of weight functions, that in the Galerkin method, are the same as the trial functions. The resulting system of equations can then be solved with respect to the nodal unknowns v_i (see Carey [18]). This approach is not generally used in CFD problems but is mostly used in structural problems.

Here the Navier-Stokes equations are discretised using a finite volume approach. As already mentioned the starting point is the integral form of the Navier-Stokes equations:

$$\begin{aligned} &\int_V \frac{\partial \boldsymbol{v}}{\partial t}\,\mathrm{d}V + \int_V (\boldsymbol{v}\cdot\boldsymbol{\nabla})\boldsymbol{v} && (2.10)\\ &-\int_V \nu\boldsymbol{\nabla}^2\boldsymbol{v}\,\mathrm{d}V = -\int_V \frac{1}{\rho_f}\boldsymbol{\nabla}p\,\mathrm{d}V && \text{in } \Omega_f\times[0,T]\\ &\int_V \boldsymbol{\nabla}\cdot\boldsymbol{v}\,\mathrm{d}V = \mathbf{0} && \text{in } \Omega_f\times[0,T] \end{aligned}$$

which, making using of the Gauss theorem, can be rewritten as:

$$\begin{aligned} &\int_V \frac{\partial u_i}{\partial t}\,\mathrm{d}V + \int_{\partial V} u_i u_j n_j\,\mathrm{d}S && (2.11)\\ &-\int_{\partial V} \mu\frac{\partial u_i}{\partial x_j} n_j\,\mathrm{d}S = -\frac{1}{\rho_f}\int_{\partial V} p n_i\,\mathrm{d}S \\ &\int_{\partial V} n_j v_j\,\mathrm{d}S = 0 && (2.12) \end{aligned}$$

Here the equation is rewritten making use of the Einstein's notation. The integrals over the volume are transformed into an integral over the surface and if one makes the assumption of flat surfaces the contribution acting on each face of the finite volumes can be summed. The entire domain is then discretised into a set of finite volumes with flat surfaces. The contributions of all the finite volumes are then summed and the Navier-Stokes equations are transformed

into a non-linear system of algebraic equations. The resulting system of equations can be solved using different techniques such as a monolithic and a partitioned approach. In the monolithic approach [17] the momentum and the continuity equations are solved together; however this approach is rarely performed because the coupled system generally has a large number of degrees of freedom and the partitioned approach is computationally less expensive. In the partitioned approach the momentum and continuity equations are solved separately using an iterative procedure. If a partition approach is used, different algorithms for the velocity pressure can be used. Among them the most used in literature are the SIMPLE [94],PISO [59] and PIMPLE algorithms. In this thesis, a partitioned approach with a PIMPLE velocity-pressure coupling algorithm is used. The PIMPLE algorithm is a combination of the PISO and the SIMPLE algorithm.

2.1.1.3 Turbulence Modelling

Most flows one finds in nature are turbulent especially at high values of the Reynolds number [85, 76, 83]. In Chapter 1 an overview of computational fluid dynamics methods used for vortex shedding problems is given. A possible way to perform the fluid computation could be using DNS simulations [91], where the whole spectrum of turbulent scales is fully resolved without any turbulent model [134]. This approach is in theory the one which permits to have the most reliable results. However, for practical engineering problems, where high Reynolds numbers are involved, this approach becomes unfeasible. In a DNS simulation, since the turbulence is not modelled the grid must be fine enough to capture all the length scales up to the Kolmogorov length microscales [73]:

$$\eta = (\frac{\nu^3}{\varepsilon})^{\frac{1}{4}} \; ; \varepsilon = \frac{u'^3}{L}; \tag{2.13}$$

in which ε is the rate of dissipation of turbulent kinetic energy per unit of mass and μ is the kinematic viscosity. u' is the root mean square of the turbulent velocity obtained in a Reynolds decomposition setting, and L is the integral length scale which is the largest scale in the energy spectrum. It means that each segment that has the length of the integral scale must be discretised with at least a number of points:

$$N = \frac{L}{\eta} = \left(\frac{u'L}{\mu}\right)^{\frac{3}{4}} \tag{2.14}$$

The quantity inside the brackets is a form of the Reynolds number so one can relate the number of cells N^3 inside a box that has the dimension of the integral length scale with the Reynolds number as:

$$N^3 = Re^{9/4} \tag{2.15}$$

To use DNS not only the grid must be fine enough, but the time step must also be small enough that within a time step a fluid particle does not cross more than one cell. It is easy to understand that this approach becomes unfeasible with the increasing of the Reynolds number. To overcome this limitation it is necessary to use different models for the turbulence modelling. In literature one can find two different approaches:

- **RANS**(Reynolds-Averaged Navier-Stokes) where the time-averaged version of the Navier-Stokes equations is solved. In this approach the instantaneous quantities of the flow, such as velocity or pressure, are decomposed using a Reynolds decomposition into a stationary part and a fluctuating part: $\boldsymbol{v}(\boldsymbol{x}, t) = \overline{\boldsymbol{v}}(\boldsymbol{x}) + \boldsymbol{v}'.(\boldsymbol{x}, t)$. Performing such a decomposition the only fluctuating term which remains inside the equation are the Reynolds stresses. The problem is that averaged Navier-Stokes equations are not a closed problem, there are more unknowns then equations. Different RANS techniques differ in the way they close the model adding additional equations [134].
- **LES** (Large Eddy Simulation) methods, unlike DNS methods, only directly resolve large eddies while small eddies are modelled. Instead of directly solving the Navier-Stokes equations a filtered version of them is solved where only big eddies and large temporal scales are considered. All the scales up to the filter size Δ are then directly resolved while scales below the filter size are opportunely modelled using a sub-grid scale model [134].

In this thesis the fluid computation is carried out using a LES turbulence model [105]. This approach has demonstrated to be particularly suitable for analysing the flow around a circular cylinder, especially in the range of Reynolds numbers interesting for practical applications [98]. In this case a sub-grid scale model is a $k-$equation eddy viscosity model [19].

2.1.2 The Solid Sub-Problem: the nonlinear beam formulation

Since the interest is not on the accurate modelling of the stresses inside each cross-section but rather on the global response of the cylinder, the structure is modelled using a beam element. In particular, a geometrically-exact beam element formulation is used. This formulation, first proposed by Reissner[100] for two-dimensional problems and then extended by Simo[113], Cardona[16] and Ibrahimbegovic[54] for three-dimensional problems, can deal efficiently with large deformations and rotations. The kinematics of the beam is treated without any approximation. The theory is based on the following assumptions:

- Rigid cross-section assumption: the beam cross-sections are treated as a rigid body. It means that during the elastic deformation they remain plane and do not deform.
- Quasi-prismatic beam assumption: meaning that the contour of the cross-sections can vary along the axis of the beam, but only continuously.

The beam element used in this thesis is the one proposed by Simo and Vu-Quoc in [114]. The general background theory presented in the next subsections is taken and re-adapted from Simo and Vu-Quoc [114] and from the other authors that later worked on geometrically-exact beams such as Cardona and Geradin [16], Ibrahimbegovic [54], Crisfield and Jelenic [64].

2.1.2.1 The Kinematic Assumption

The reference and the deformed configurations are presented in Figure 2.1. For sake of simplicity, it is assumed that, in the reference configuration, the line of centroids is a straight line and that the base vector $\boldsymbol{E_3}$, describing the direction of the line of centroids, coincides with the X_3 axis of the inertial reference frame. The other two base vectors $\boldsymbol{E_1}$ and $\boldsymbol{E_2}$ are directed along the principal axis of inertia of the cross-section. The position vector $\boldsymbol{D_o}$ of a material particle P_0 in the reference configuration can be written as:

$$\boldsymbol{D_o} = \boldsymbol{d_o}(X3) + \boldsymbol{R_o}(X1, X2) \tag{2.16}$$

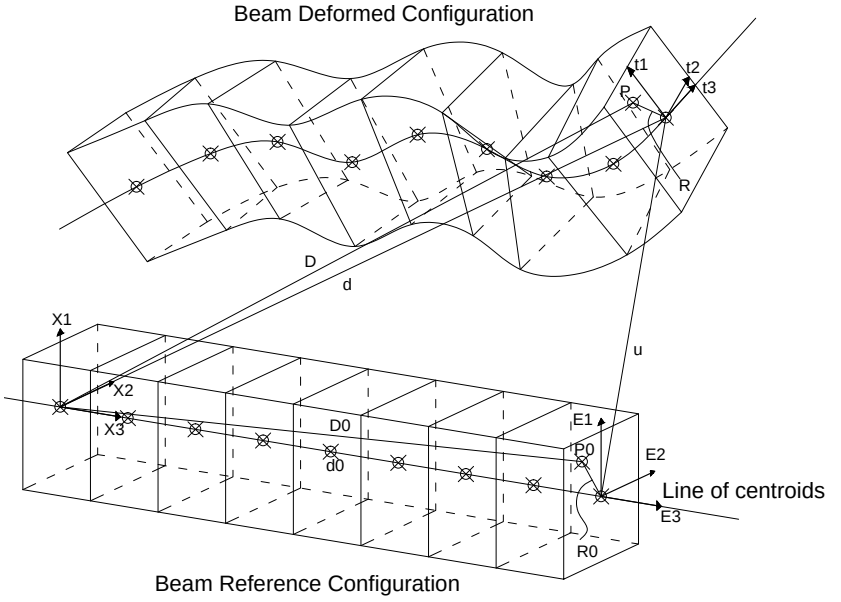

Figure 2.1: Kinematic assumption of the beam element

In the deformed configuration the position vector $\boldsymbol{D}$ of the same material particle P can be written as:

$$\boldsymbol{D} = [\boldsymbol{d_o}(X3) + \boldsymbol{u}(X_3)] + \boldsymbol{R}(X1, X2) \tag{2.17}$$

where $\boldsymbol{R}$ is the radius vector in deformed configuration. Because of the assumption of rigid cross-sections the vector $\boldsymbol{R}$ in deformed configuration can be seen as a rigid rotation of the vector $\boldsymbol{R_o}$ in the reference configuration:

$$\boldsymbol{D} = [\boldsymbol{d_o}(X3) + \boldsymbol{u}(X_3)] + \boldsymbol{\Lambda}(X_3)\boldsymbol{R_o}(X1, X2) \tag{2.18}$$

where $\boldsymbol{\Lambda}$ is a rotation matrix belonging to the $3D$ rotation group $SO(3)$ [55]. Following this theory, at each instant the deformed configuration of the beam is defined by means of the position vector $\boldsymbol{d}$, which defines the deformed configuration of the line of centroids, and by means of a rigid rotation defined by the rotation matrix Λ. The rotation matrix can be described by means of the rotation vector $\boldsymbol{\varphi} = [\varphi_1\ \varphi_2\ \varphi_3]^T$ that has the same direction of the axis of rotation and its modulus is equal to the angle of the rotation. The relationship

between the rotation vector and the rotation matrix can be written as:

$$\boldsymbol{\Lambda} = \exp \tilde{\boldsymbol{\varphi}} = \boldsymbol{I} + \frac{\sin \|\boldsymbol{\varphi}\|}{\|\boldsymbol{\varphi}\|}\tilde{\boldsymbol{\varphi}} + \frac{1 - \cos \|\boldsymbol{\varphi}\|}{\boldsymbol{\varphi} \cdot \boldsymbol{\varphi}}\tilde{\boldsymbol{\varphi}}^2 \tag{2.19}$$

where $\tilde{\boldsymbol{\varphi}}$ is the skew symmetric matrix associated with the rotation vector. Each cross-section of the beam is described by 6 degrees of freedom, 3 translations and 3 rotations. It is important to underline that, contrary to translations, which belong to a vector space, rotations cannot be updated using a simple summation. The updating procedure between two consecutive time steps can be written using the following expression:

$$\boldsymbol{d_{n+1}} = \boldsymbol{d_n} + \boldsymbol{u_n} \tag{2.20}$$

$$\boldsymbol{\Lambda_{n+1}} = \exp \tilde{\boldsymbol{\phi}}_{\boldsymbol{n}} \boldsymbol{\Lambda_n} \tag{2.21}$$

Where $\tilde{\boldsymbol{\phi}}$ is the pseudo-rotation vector that transform the basis $\boldsymbol{G_{i,n}}$ into the basis $\boldsymbol{G_{i,n+1}}$. The subscript n denotes the temporal discrete of a time-varying quantity at time t_n.

2.1.2.2 The strain Measures

Once the kinematics of the beam is defined one can report the translational and rotational strain measures of the beam, $\boldsymbol{\Gamma}$ and $\boldsymbol{K}$, defined here with respect to the initial reference frame and related to the current configuration of the beam $(\boldsymbol{d}, \boldsymbol{\varphi})$ with:

$$\boldsymbol{\Gamma} = \boldsymbol{d}' - \boldsymbol{E_3} \tag{2.22}$$

$$\boldsymbol{K} = \boldsymbol{T}^{\boldsymbol{T}} \boldsymbol{\varphi}' \tag{2.23}$$

where the $'$ symbol denotes the derivative respect to the axial coordinate, $\boldsymbol{E_i}$ is the reference frame in the initial configuration and $\boldsymbol{\varphi}$ is the total rotation vector. $\boldsymbol{T}$ is the transformation tensor [55]:

$$\boldsymbol{T} = \frac{\sin \varphi}{\varphi}\boldsymbol{I} + \frac{1 - \cos \varphi}{\varphi^2}\tilde{\boldsymbol{\varphi}} + \frac{\varphi - \sin \varphi}{\varphi^2}\tilde{\boldsymbol{\varphi}}^2 \tag{2.24}$$

The body-attached formulation, if a linear material is used, permits to relate the strain measures with the force and moment resultants:

$$\boldsymbol{N} = \boldsymbol{C_N \Gamma} \tag{2.25}$$

$$\boldsymbol{M} = \boldsymbol{C_M K} \tag{2.26}$$

in which $\boldsymbol{C_N} = \text{diag}[EA\ GA_2\ GA_3]$ and $\boldsymbol{C_M} = \text{diag}[GJ_t\ EI_2\ EI_3]$ are the constitutive matrices.

2.1.2.3 The equation of motion

Now that the kinematics and the strain measures are defined the equation of motion can be written in strong form:

$$(\boldsymbol{\Lambda N})' + \boldsymbol{n} = A\rho\ddot{\boldsymbol{u}} \tag{2.27}$$

$$(\boldsymbol{\Lambda M})' + \boldsymbol{d}' \times \boldsymbol{\Lambda N} + \boldsymbol{m} = \boldsymbol{\Lambda}(\tilde{\boldsymbol{\Omega}} \boldsymbol{I}_\rho \boldsymbol{\Omega} + \boldsymbol{I}_\rho \boldsymbol{A}) \tag{2.28}$$

in which $\boldsymbol{n}$ and $\boldsymbol{m}$ are external applied forces and moments for unit of length, A is the area cross-section, ρ is the material density, $\tilde{\boldsymbol{\Omega}}$ is the skew symmetric matrix associated with the angular velocity vector $\boldsymbol{\Omega}$, $\boldsymbol{I}_\rho$ is the mass moment of inertia tensor and $\boldsymbol{A}$ is the angular acceleration vector. Among these quantities the following relationship can be observed:

$$\tilde{\boldsymbol{\Omega}} = \boldsymbol{\Lambda^T \dot{\Lambda}};\ \boldsymbol{\Omega} = \boldsymbol{T^T \dot{\varphi}} \tag{2.29}$$

$$\tilde{\boldsymbol{A}} = \boldsymbol{\Lambda^T \ddot{\Lambda}} + \boldsymbol{\dot{\Lambda}^T \dot{\Lambda}};\ \boldsymbol{A} = \boldsymbol{T^T \ddot{\varphi}} + \boldsymbol{\dot{T}^T \dot{\varphi}} \tag{2.30}$$

Equation 2.27 and Equation 2.28, alongside the boundary conditions on displacement or applied external forces and moments, completely define the problem. These equations are then multiplied by appropriate vector test functions $\boldsymbol{P_1}$ and $\boldsymbol{P_2}$, which must be at least C^1, and vanish where one has prescribed kinematic boundary condition, it is possible to obtain:

$$\boldsymbol{P_1}^T[\boldsymbol{\Lambda N}' + \boldsymbol{n} - A\rho\ddot{\boldsymbol{d}}] = 0 \tag{2.31}$$

$$\boldsymbol{P_2}^T[(\boldsymbol{\Lambda M})' + \boldsymbol{d}' \times \boldsymbol{\Lambda N} + \boldsymbol{m} - \boldsymbol{\Lambda}(\tilde{\boldsymbol{\Omega}} \boldsymbol{I}_\rho \boldsymbol{\Omega} + \boldsymbol{I}_\rho \boldsymbol{A})] = 0 \tag{2.32}$$

that after integration over the beam domain $[0, L]$, and partial integration of the terms $(\boldsymbol{\Lambda N})'$ and $(\boldsymbol{\Lambda M})'$, can be collected into a single equation in order

to write the weak form of the equation of motion:

$$\int_0^L (\boldsymbol{P_1}'^T \boldsymbol{\Lambda N} + \boldsymbol{P_1}^T A\rho\ddot{\boldsymbol{u}})\,\mathrm{d}x + \int_0^L [\boldsymbol{P_2}'^T \boldsymbol{\Lambda M} - \boldsymbol{P_2}^T \tilde{\boldsymbol{d}}' \boldsymbol{\Lambda N} + \boldsymbol{P_2}^T \boldsymbol{\Lambda}(\tilde{\boldsymbol{\Omega}} \boldsymbol{I_\rho} \boldsymbol{\Omega} + \boldsymbol{I_\rho} \boldsymbol{A})]\,\mathrm{d}x - \int_0^L \boldsymbol{P_1}^T \boldsymbol{n}\,\mathrm{d}x - \int_0^L \boldsymbol{P_2}^T \boldsymbol{m}\,\mathrm{d}x + (\boldsymbol{P_{1o}} \boldsymbol{F_o} + \boldsymbol{P_{1L}} \boldsymbol{F_L} + \boldsymbol{P_{2o}} \boldsymbol{T_o} + \boldsymbol{P_{2L}} \boldsymbol{T_L}) = 0 \tag{2.33}$$

In Equation 2.33 the last line represents the Neumann boundary conditions. The weak form of the equation of motion can be solved using a finite element approach. The next step is the interpolation of the test functions along the length of the beam, which has to be divided into N-noded finite elements:

$$\boldsymbol{P_1}(x) = \sum_{i=1}^{N} Q^i(x) \boldsymbol{P_{1i}};\ \boldsymbol{P_2}(x) = \sum_{i=1}^{N} Q^i(x) \boldsymbol{P_{2i}} \tag{2.34}$$

in which Q are polynomial shape functions. Once the test functions are interpolated the weak equation of motion becomes partially discretised in space and one can proceed with the time numerical integration of velocities and accelerations. The last the step is the interpolation of the chosen unknowns. The unknown configuration at time step t_{n+1} is given by the position vector $\boldsymbol{d_{n+1}}$ and the rotation matrix $\boldsymbol{\Lambda_{n+1}}$. $\boldsymbol{\Lambda_{n+1}}$ belongs the non-linear differential manifold $SO(3)$ so it cannot be directly interpolated. As discussed in the next subsection, in order to be solved, the presented equations must be linearised, for this reason, the infinitesimal change of displacements and rotations are chosen as unknowns $\Delta \boldsymbol{p}_j = [\Delta \boldsymbol{u}_j\ \Delta \boldsymbol{\varphi}_j]^T$. In this case, the same shape functions are used for the interpolation of the test functions and for the interpolation of the unknowns (Bubnov-Galerkin method [143]). Once the problem is fully discretised in space and time it can be rewritten, for a time step t_{n+1}, in compact form as a non-linear system of equations:

$$\sum_{i=1}^{n} (\boldsymbol{g}^i_{iner,n+1} + \boldsymbol{g}^i_{int,n+1} - \boldsymbol{g}^i_{ext,n+1}) = 0 \tag{2.35}$$

in which the term inside the equation are the inertial, internal and external forces contributions:

$$\boldsymbol{g}^i_{iner,n+1} = \int_0^L Q^i \begin{pmatrix} A\rho\ddot{\boldsymbol{u}}_{n+1} \\ \boldsymbol{\Lambda}_{n+1}(\tilde{\boldsymbol{\Omega}}_{n+1}\boldsymbol{I}_{\boldsymbol{\rho}}\boldsymbol{\Omega}_{n+1} + \boldsymbol{I}_{\boldsymbol{\rho}}\boldsymbol{A}_{n+1}) \end{pmatrix} \mathrm{d}x \tag{2.36}$$

$$\boldsymbol{g}^i_{int,n+1} = \int_0^L \begin{bmatrix} Q^{i'}\boldsymbol{I} & \mathbf{o} \\ -Q^{i'}\tilde{\boldsymbol{d}}'_{n+1} & Q^{i'}\boldsymbol{I} \end{bmatrix} \begin{bmatrix} \boldsymbol{\Lambda}_{n+1} & \mathbf{o} \\ \mathbf{o} & \boldsymbol{\Lambda}_{n+1} \end{bmatrix} \begin{pmatrix} \boldsymbol{N}_{n+1} \\ \boldsymbol{M}_{n+1} \end{pmatrix} \mathrm{d}x \tag{2.37}$$

$$\boldsymbol{g}^i_{ext,n+1} = \int_0^L Q^i \begin{pmatrix} \boldsymbol{n}_{n+1} \\ \boldsymbol{m}_{n+1} \end{pmatrix} \mathrm{d}x + \delta^i_1 \begin{pmatrix} \boldsymbol{F}_0 \\ \boldsymbol{T}_0 \end{pmatrix} + \delta^i_N \begin{pmatrix} \boldsymbol{F}_L \\ \boldsymbol{T}_L \end{pmatrix} \tag{2.38}$$

2.1.2.4 Linearisation of the non-linear system of equations

The non-linear system of equations can be solved iteratively using a Newton-Raphson procedure and a linearisation of the system around an arbitrary configuration:

$$\Delta\boldsymbol{g}^i_{n+1+\alpha} = -\boldsymbol{g}^i_{n+1+\alpha} \tag{2.39}$$

which can be rewritten as:

$$\Delta\boldsymbol{g}^i_{n+1+\alpha} = \boldsymbol{K}^{ij}\Delta\boldsymbol{p}_j \tag{2.40}$$

$$\boldsymbol{K}^{ij} = \boldsymbol{K}^{ij}_{tras} + \boldsymbol{K}^{ij}_{rot} + \boldsymbol{K}^{ij}_{mat} + \boldsymbol{K}^{ij}_{iner} + \boldsymbol{K}^{ij}_{ext} \tag{2.41}$$

$$\Delta\boldsymbol{p}_j = [\Delta\boldsymbol{u}_j\ \Delta\boldsymbol{\varphi}_j]^T \tag{2.42}$$

in which $\boldsymbol{K}^{ij}$ represents the tangent stiffness matrix due to the linearisation procedure and is composed by the geometric contribution due the linearisation of translations and rotations around the configuration, the contribution of the material stiffness matrix, the contribution of the inertial stiffness matrix and the contribution of the external loads in case of external loads which are configuration dependent. The vector $\Delta\boldsymbol{p}$ contains the incremental changes of displacements and rotations.

2.1.2.5 Time Integration Procedure

The numerical integration of velocities and accelerations can be performed using different methods. Here a generalized HHT-α integration scheme [48] is

used. In order to update translational quantities after one step a Newmark procedure is used:

$$\dot{\boldsymbol{u}}_{n+1} = \frac{\gamma}{\beta \Delta t} \Delta \boldsymbol{u} + \left(1 - \frac{\gamma}{\beta}\right) \dot{\boldsymbol{u}}_n + \Delta t \left(1 - \frac{\gamma}{2\beta}\right) \ddot{\boldsymbol{u}}_n \tag{2.43}$$

$$\ddot{\boldsymbol{u}}_{n+1} = \frac{1}{\beta \Delta t^2} \left[\Delta \boldsymbol{u} - \Delta t \dot{\boldsymbol{u}}_n - \Delta t^2 \left(\frac{1}{2} - \beta\right) \ddot{\boldsymbol{u}}_n \right] \tag{2.44}$$

$$\Delta \boldsymbol{u} = \boldsymbol{u}_{n+1} - \boldsymbol{u}_n \tag{2.45}$$

with the difference that the time discrete equation of motion of Equation 2.35 is modified in this manner:

$$\begin{aligned} \boldsymbol{g}^i_{n+1+\alpha} =& \boldsymbol{g}^i_{iner,n+1} + (1+\alpha)\boldsymbol{g}^i_{int,n+1} - \alpha \boldsymbol{g}^i_{int,n} \\ & - (1+\alpha)\boldsymbol{g}^i_{ext,n+1} + \alpha \boldsymbol{g}^i_{ext,n} = \mathbf{o} \end{aligned} \tag{2.46}$$

$$\tag{2.47}$$

in which α is a numerical damping parameter value which may range between 0 and $-\frac{1}{3}$. The same procedure of Equation 2.43 and 2.44 can also be applied to angular velocities and accelerations changing $\dot{\boldsymbol{u}}$ with the angular velocity $\boldsymbol{\Omega}$, $\ddot{\boldsymbol{u}}$ with the angular acceleration $\boldsymbol{A}$ and $\Delta \boldsymbol{u}$ with the skew symmetric matrix associated with the incremental rotation vector. This procedure is valid only if it is performed in a body-attached reference frame. It means that one must use the incremental rotation vector $\boldsymbol{\varphi}$ which performs the rotation of the body attached frame between the instant t_n and t_{n+1}.

2.1.3 The Direct Force-Motion transfer procedure and the mesh motion problem

Once the two sub-problems are defined and Algorithm 1 is introduced one needs to develop an efficient mesh motion algorithm and to implement an efficient DFMT method. This step is particularly delicate because one needs to pay attention to develop a procedure which is energy-conserving. This procedure is not always simple, usually in FSI problems one has to deal with non-matching meshes, and in this particular case even different spatial dimensions are involved. In fact, the beam is a mono-dimensional object, while the fluid forces, obtained via pressure integration and linear interpolation, are evaluated on the FSI interface, which is a 2-D surface in three-dimensional

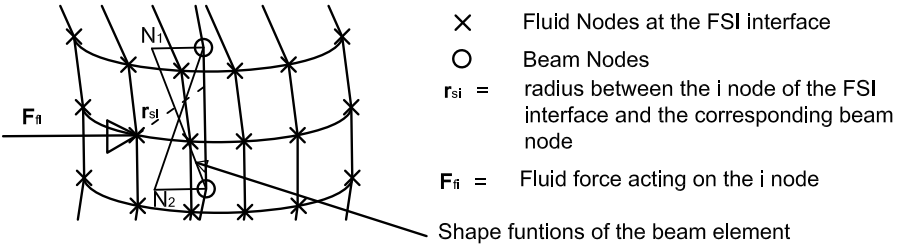

Figure 2.2: Coupling of fluid and structural meshes

space. For each time step of the coupling algorithm one needs to update the mesh of the fluid problem using the displacements coming from the solid computation, and one needs to transfer fluid forces evaluated on the FSI interface to the nodes of the beam element. The problem is solved making the hypotheses of non-deformable cross-sections. Fluid forces are obtained by circumferential integration and transferred to the beam nodes through the shape functions of the beam. Fluid forces may be not always orthogonal to the FSI interface because of viscous stresses. For this reason, both forces and moments need to be transferred. At the beginning of each simulation one has to define a mapping between the nodes on the FSI interface and the beam elements, and vice versa. In other words, one has to assign to each beam element a certain number of nodes which insists on it. This procedure is performed by only making geometrical considerations on the initial in-deformed geometry. Since the assumption of in-deformable cross-section is done, this mapping also remains the same during the beam deformation. Once this mapping is defined, focusing only on one beam element, is possible to write the procedure to transform forces acting on the FSI interface into forces and moments acting on the nodes of the beam (Figure 2.2):

$$\boldsymbol{F_s}_j = \sum_{i=1}^{Nf} I_j(\xi_i) \boldsymbol{F_f}_i \tag{2.48}$$

$$\boldsymbol{M}_{sj} = \sum_{i=1}^{Nf} I_j(\xi_i)(\boldsymbol{r_s}_i \times \boldsymbol{F_f}_i) \tag{2.49}$$

Where $\boldsymbol{Fs}_j$ is the force acting on the j^{th} node of the beam element, $I_j(\xi_i)$ is the shape function relative to the j^{th} node of the beam evaluated on the natural coordinate ξ_i which correspond to the fluid force $\boldsymbol{F_f}_i$. $\boldsymbol{r_s}_i$ is the radius between the i^{th} fluid node and the beam element. The adjoint procedure

has to be performed on displacements. Beam nodal displacements have to be properly converted into displacements of the FSI interface. Since an element with finite rotation is involved, and interpolation of rotation variables only makes sense on incremental quantities [63], the updating procedure of the position of the FSI interface has to be performed in an incremental way:

$$\boldsymbol{u_f}_{i,n+1} = \boldsymbol{u_f}_{i,n} + \sum_{j=1}^{2} \left[I_j(\xi_i)\Delta\boldsymbol{u}_j + \boldsymbol{\Lambda}(I_j(\xi_i)\Delta\boldsymbol{\varphi}_j)\boldsymbol{r_s}_{i,n} \right] \tag{2.50}$$

where $\boldsymbol{u_f}_{i,n+1}$ and $\boldsymbol{u_f}_{i,n}$ are the displacement of the i^{th} fluid node on the FSI interface respectively at time t_{n+1} and t_n, $\Delta\boldsymbol{u}_j$ and $\Delta\boldsymbol{\varphi}_j$ are the incremental displacement and rotation vector, and $\boldsymbol{r_s}_{i,n}$ is the radius between the i^{th} fluid node on the FSI interface and the relative beam at time t_n.

The coupling of the fluid and the solid problems, as already mentioned in Subsection 2.1, is realized in a strong way using a block Gauss-Seidel coupling algorithm. For the sake of simplicity, and because of the limited computational cost of the solid problem, that only consists of a limited number of beam elements, the time step of the fluid problem is imposed to be equal to the time step of the solid problem. Now that the procedure to move points on the FSI interface is defined, a procedure for the movement of other fluid points has to be identified. Fluid points that do not belong to the FSI interface are moved according to a Laplacian smoothing algorithm [62]: the equation of cell motion is solved based on the Laplacian of the diffusivity and the cell displacements. The diffusivity field is quadratically based on the inverse of the cell centre distance to the FSI interface.

2.2 Validation of the CFD problem

The reliability of the present method is strongly correlated to the reliability of the fluid computation. For this reason, in order to validate the whole model, the first step is to validate the small scale model and the CFD solver. A CFD simulation on a static domain is performed and the results are compared to numerical and experimental data in terms of lift, drag, and Strouhal number.

Lift and drag forces are described in terms of the drag coefficient and lift

coefficient:

$$C_D = \frac{F_D}{0.5\rho U^2 D} \qquad (2.51)$$
$$C_L = \frac{F_L}{0.5\rho U^2 D}$$

where F_D and F_L are the drag and lift force per unit of length respectively and U is the free stream velocity of the flow. In Figure 2.3 the time evolution of the lift and drag coefficient is reported. All the results are carried out using a Reynolds number $Re = 6.31 \times 10^4$ which matches the Reynolds value of the benchmark from [98]. The results are compared to the same benchmark case in terms of root mean square (RMS) of the lift coefficient, mean drag coefficient, and Strouhal number. As one can see from Table 2.1, results match well with experimental and previous numerical results.

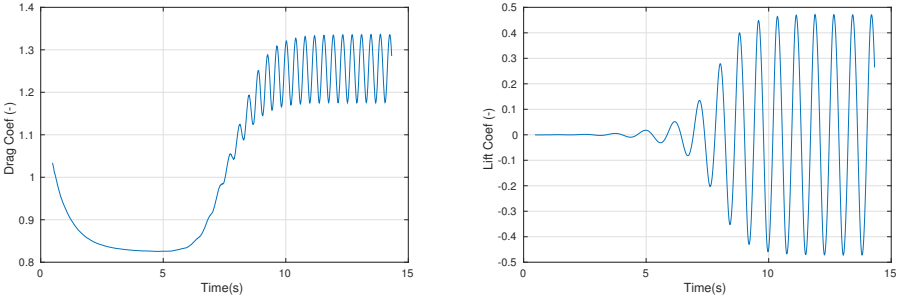

Figure 2.3: Time evolution of drag and lift coefficients

	RMS LC	MEAN DC	ST
Exp. Value	0.24	1.16	0.19
Present	0.33	1.25	0.20
A	0.53	0.70	0.28
B	0.47	0.87	0.25
C	0.83	1.05	0.25
D	0.60	1.37	0.18
E	0.18	1.10	0.28
F	0.51	1.49	0.20
G	0.86	1.14	0.24
H1	1.08	1.28	0.29
H2	0.10	0.54	0.35
H3	0.58	1.38	0.22
H4	0.99	1.70	0.21

Table 2.1: Comparison with literature and experimental values from [98]

2.3 Some results of FSI solver

The developed FSI solver is used to perform some preliminary analysis in order to understand the capability of the code and to gain insight onto the physics of the problem. Three different simulations are proposed here. The first simulation is performed on a beam which is clamped at both ends and immersed in a flow with a uniform constant velocity. In the second simulation, a harmonic motion is imposed for both the cross-flow and the in-line direction at both ends with the same frequencies. In the third simulation, the imposed harmonic motion at one end has a frequency of oscillation which is the double that of the other end. Results are reported in terms of displacements in the mid-point of the model. All the presented simulations have some common features which are presented in Subsections 2.3.1 and 2.3.2.

2.3.1 Setting of the fluid problem

The diameter of the tested cylinder is equal to $D = 0.102$m, which is a common diameter for mooring line cables available on the market. The fluid mesh is represented in Figure 2.4 and is structured using a polar distributed grid in the proximity of the cylinder and a Cartesian distributed grid in the other regions. Only hexahedral elements are used. The region near to the wall is refined in order to obtain a y^+ number close to the unity. An equally spaced mesh is used along the vertical direction ($\Delta z \approx$ D/2). The distance of the

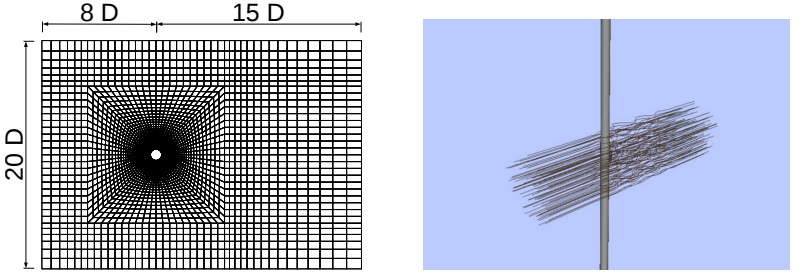

(a) top view of the mesh

(b) View of the cylinder with stream-lines

Figure 2.4: Domain of the simulation

cylinder from the inlet is equal to $8D$, the distance from the outlet is equal to $15D$, and the domain width is equal to $20D$. The domain height is equal to $40D$. The height of the domain is chosen in order to make the structure slender enough to be modelled using a beam theory. The flow has a constant uniform velocity at the inlet and constant zero pressure value at the outlet. Sides are modelled with slip conditions, and the lower and upper sections are modelled as symmetry planes. The PIMPLE algorithm [62] and an Euler implicit time integration scheme are used. A constant time step Δt_f is chosen, making a check on the Courant number running a simulation on a static case. The check on the time step is performed in order to obtain a Courant number which is always smaller than 1. The fluid is water. The properties of the fluid computation are reported in Table 2.2.

Name	Symbol	Value	Unit
Time step	Δt_f	10^{-3}	s
Density	ρ_f	10^3	$\mathrm{kg/m^3}$
Kinematic viscosity	μ_f	10^{-6}	$\mathrm{m^2/s}$
Inlet flow velocity	v_{inl}	1	m/s

Table 2.2: Settings for the fluid computations

2.3.2 Setting of the structural problem

The structure is discretised with 40 equally spaced geometrically-exact beam elements with the same spacing used for the fluid sub-problem. The same

time step size of the fluid sub-problem is used. The structure has a cylindrical cross-section and constant density. The structural properties of the beam are reported in Table 2.3. The time integration scheme used is a HHT-α method with parameters $\alpha = 0.67$, $\gamma = 0.83$ and $\beta = 0.44$. In order to avoid instability due to the beginning of the simulation the hydrodynamic forces are smoothly transferred to the structure with a ramp load during the first 0.5 seconds.

Name	Symbol	Value	Unit
Time step	Δt_s	10^{-3}	s
Young's Modulus	E_s	5.88×10^8	N/m^2
Diameter	D_s	1.020×10^{-1}	m
Density	ρ_s	5.582×10^3	kg/m^3
Poisson's ratio	μ_s	0.3	1
Damping ratio	ξ	0.05	1

Table 2.3: Settings for the solid computations

2.3.3 Setting of the coupled problem

As mentioned in previous sections. The coupled problem is solved using a partitioned approach. The time step of the coupled simulation is the same as the structural and the fluid computation, $\Delta t_{coupl} = 0.001$s. Since a strong coupling algorithm is used, an iteration procedure is needed at each time step. A block Gauss-Seidel algorithm is used to solve the iteration procedure and an Aitken's relaxation technique is used to speed up the computation. For each time step at the beginning of the iteration procedure the initial value of the relaxation value is equal to 0.7; for successive iterations the relaxation factor is evaluated using the Aitken's formula [71].

2.3.4 Clamped Beam

In this simulation the beam is clamped at both ends. Results regarding displacements are presented in adimensionalised form. Displacements are divided by the diameter. After a certain time the cable starts to oscillate in both the cross-flow and the in-line direction at a constant frequency, as seen in Figure 2.5. The frequency of oscillation in cross-flow direction is

equal to 1.05Hz. The first "dry" natural frequency of the structure is equal to 1.3Hz while the first "wet" natural frequency, taking into account only the added mass effect, is equal to 1.2Hz. Considering that the real natural "wet" frequency will have a lower value one can assume that the structure is oscillating to a frequency which is close to the first natural frequency in water. The structure is also oscillating in the in-line direction with approximately twice the cross-flow vibration frequency. The trajectory observed [Figure 2.7] is similar to that observed by other authors, see [11]. A previous analysis, with the same setting of the FSI simulation but conducted on a rigid cylinder, has shown a Strohual number $St = 0.1981$ which matches experimental results and leads to a shedding frequency $S_v = 1.94$Hz. This frequency is almost twice the cross-flow oscillation frequency. In this case, since the structure is oscillating at a frequency which is higher than the cross-flow frequency it means that the natural frequency of the structure is governing the phenomena. The so-called lock-in phenomenon is observed. It is observed similar behaviour regarding the in-line displacement after an initial transient. In fact, it is present a static deformation due the mean component of the drag forces and a fluctuating deformation due to the vortex shedding phenomena. The frequency of oscillation along the cross flow direction is equal to 2.04Hz which is equal to approximately twice the vortex oscillating frequency for the cross-flow direction. The amplitude of oscillation is approximately equal to $1.5D$ for the CF direction and $0.5D$ for the IL direction. As seen in figures 2.5 and 2.6, the motion reaches a regime state after approximately 5s, this corresponds to 5 periods of vortex shedding.

2.3.5 Imposed motion type 1

In this simulation, the cable has a cross-flow and an in-line imposed motion. This test is performed because in the development of the ROM the idea is to force a piece of cable with a certain imposed motion matching the expected full-scale response. The cable remains fixed for the first 3s then an harmonic imposed motion is started. The imposed motion is gradually applied and it reaches a steady state after the first three periods. This is done in order to improve the numerical stability of the simulation. The harmonic motion is imposed on both ends in the cross-flow direction only. The frequency of the imposed motion is equal to 1Hz and the amplitude is equal to $0.25D$. The amplitude of the applied imposed motion is equal to $0.25D$ for both the IL

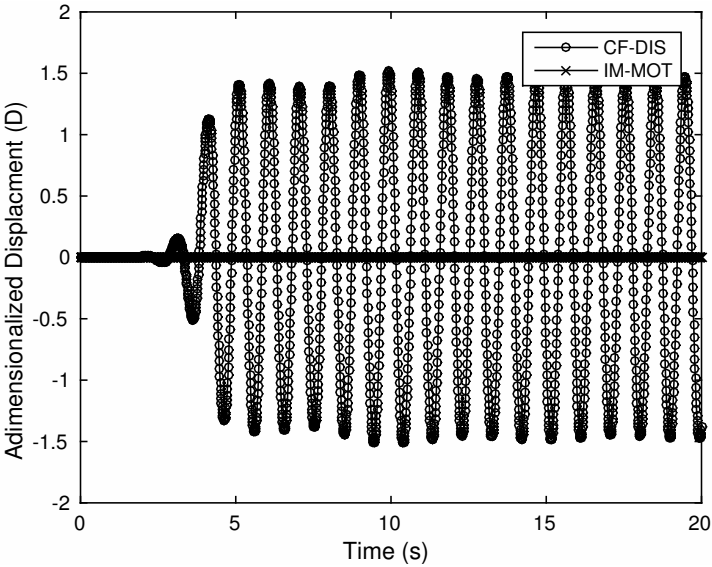

Figure 2.5: Displacement of the centre point in the CF direction

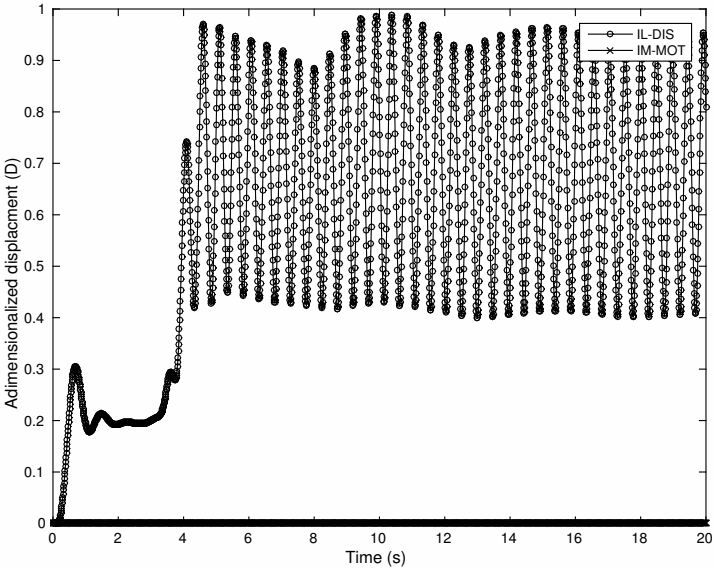

Figure 2.6: Displacement of the centre point in the IL direction

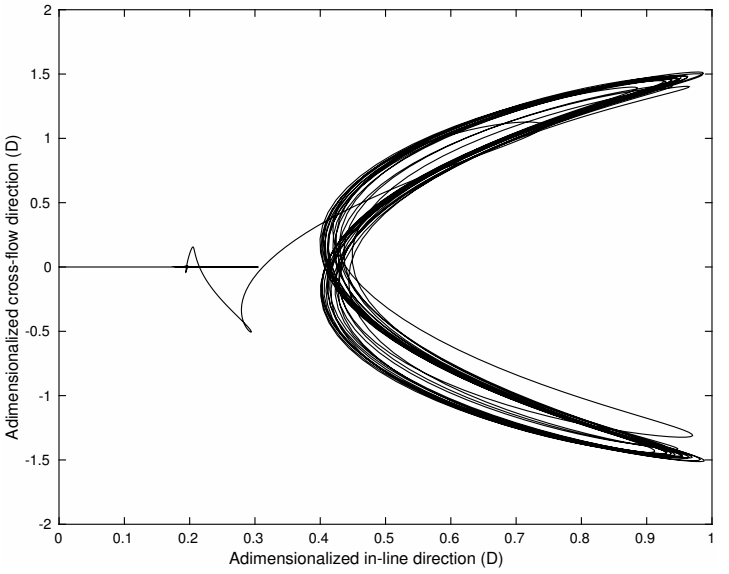

Figure 2.7: Trajectory of the centre point

and the CF direction. It means that the cable is oscillating along a line which is inclined at 45° with respect to the flow direction. Although this trajectory is quite unrealistic it helps to test the robustness of the developed model. As seen in Figure 2.5 the cable reached a steady state behaviour after circa 10 seconds, oscillating on the same frequency as the imposed motion frequency 1Hz. Along the IL direction two frequencies of oscillation are observed, 0.5Hz and 4Hz. The cable has the same characteristics as simulation number 1. In this case, the oscillating motion is governing the vortex shedding. The trajectory is similar to that observed for simulation N.1. In this, case both the in-line and the cross-flow responses show bigger displacements.

2.3.6 Imposed motion type 2

The motion differs for both ends. The amplitude is again equal to $0.25D$ but one end is moving with twice the frequency of the other end, i.e. 0.5Hz and 1Hz. Again this simulation has not a particular physical meaning but it is useful to test the robustness of the code in case of different motions at the ends. As expected, in the response one observes two different frequencies equal to the frequencies of the imposed motions at the two ends.

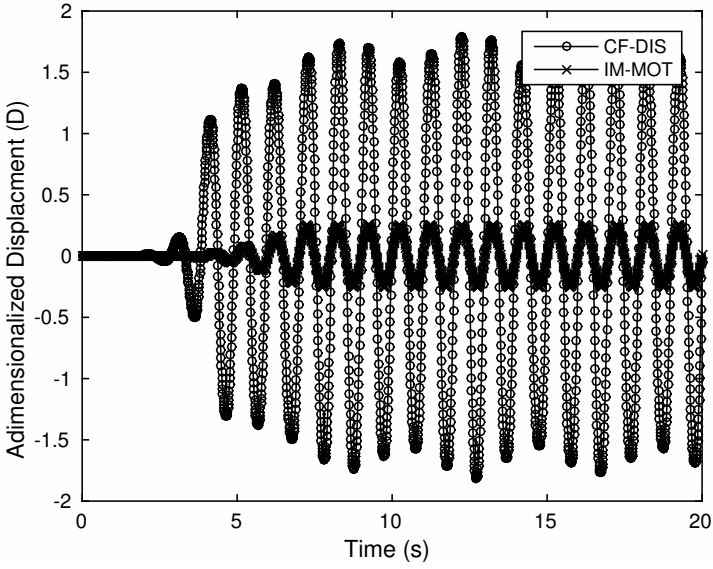

Figure 2.8: Displacement of the centre point in the CF direction

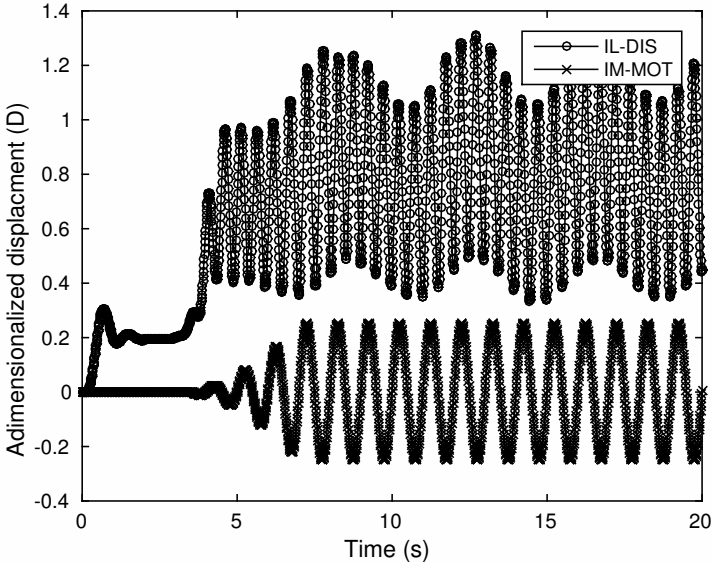

Figure 2.9: Displacement of the centre point in the IL direction

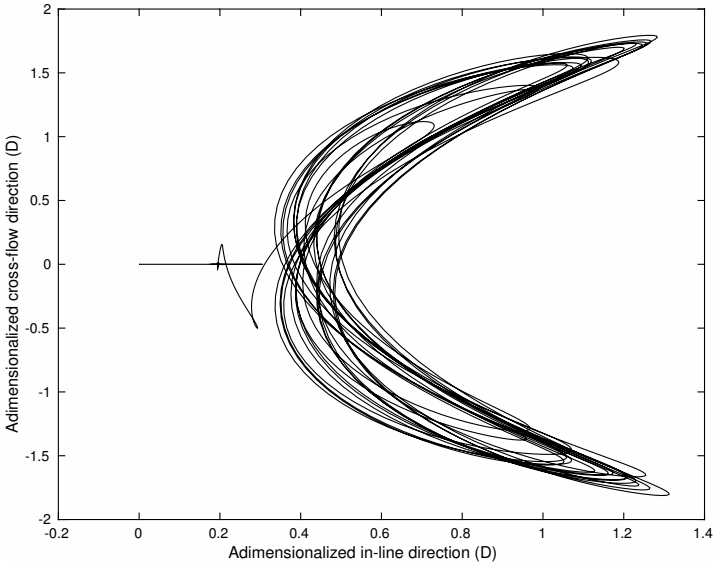

Figure 2.10: Trajectory of the centre point

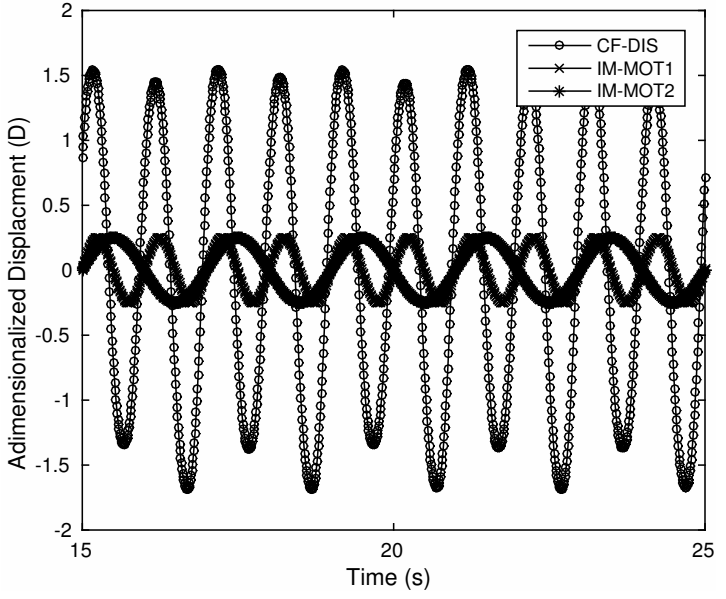

Figure 2.11: Displacement of the centre point in the CF direction

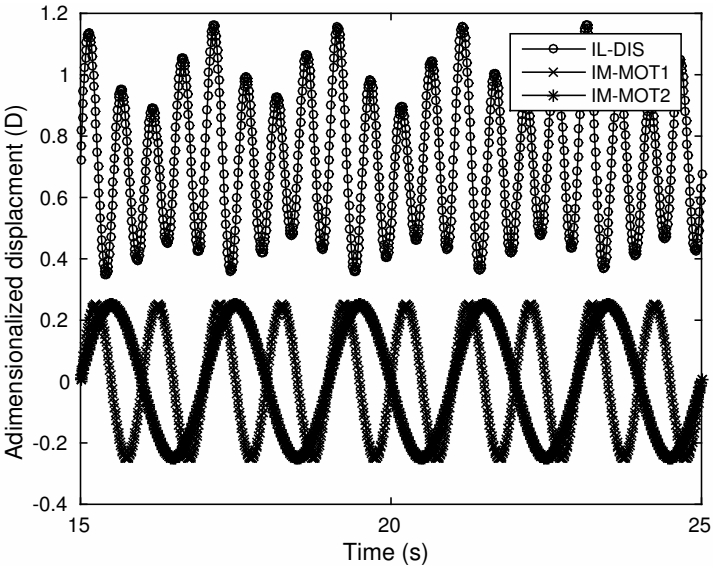

Figure 2.12: Displacement of the centre point in the IL direction

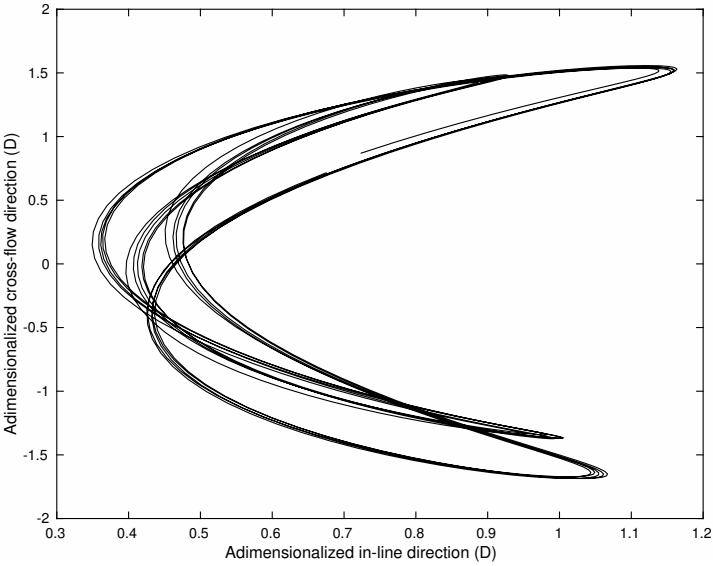

Figure 2.13: Trajectory of the centre point

Chapter 3

The Coarse Scale Model and the Deterministic Identification Procedure

In this chapter the coarse-scale model is introduced and the methods used for the system and parameter identification are explained and discussed. The identification is then applied to a real case and results are presented and discussed.

Contents

In this chapter the methods used for the development of the coarse scale model are introduced and explained. It is important to remember that the aim of this thesis is the development of a computational tool that is able to study the hydrodynamic forces acting on long flexible cylinders. The tool is developed in a way that it can be added to any structural dynamic code. The coarse scale model is constructed through a system-parametric identification technique. The results of the fine scale model are used to identify the parameters and the structure of the coarse scale model. In this thesis, different systems for the coarse scale model are proposed and discussed.

3.1 Deterministic Linear System Identification

In this section the methods used in this thesis, for the linear system identification, are briefly introduced and discussed. For further details on the methods presented in this thesis one may see classical books on linear system identification [78, 137, 124] . The first model used for the identification is a continuous time-invariant state-space model:

$$\begin{aligned} \dot{\boldsymbol{x}}(t) &= \boldsymbol{A}\boldsymbol{x}(t) + \boldsymbol{B}\boldsymbol{u}(t) \\ \boldsymbol{y}(t) &= \boldsymbol{C}\boldsymbol{x}(t) + \boldsymbol{D}\boldsymbol{u}(t) \end{aligned} \tag{3.1}$$

in which $\boldsymbol{x}(t)$ is the state vector of dimension $n \times 1$, $\boldsymbol{y}(t)$ is the output vector of dimension $q \times 1$, $\boldsymbol{u}(t)$ is the input vector of dimension $p \times 1$, $\boldsymbol{A}$ is the state matrix of dimension $n \times n$, $\boldsymbol{B}$ is the input matrix of dimension $n \times p$, $\boldsymbol{C}$ is the output matrix of dimension $q \times n$, $\boldsymbol{D}$ is the feed-through matrix of dimension $q \times p$.

Once the dimension of the state-space vector, and the number of inputs and outputs are fixed the identification process consists of finding the matrices $\boldsymbol{A}$, $\boldsymbol{B}$, $\boldsymbol{C}$ and $\boldsymbol{D}$ that minimize the difference between the measured output and the simulated output. For measured output it is intended the results obtained using the fine scale model. For simulated output it is intended the results obtained using the coarse scale model. Before using the identified matrices inside a structural solver one needs to convert the continuous state-space model to a discrete state-space model which matches the time step used by the structural simulation for the derivation of the proposed equation see [5].

The continuous identified matrices in a discrete form become:

$$\boldsymbol{A}_d = e^{\boldsymbol{A}T},\ \boldsymbol{B_D} = \boldsymbol{A^{-1}}(\boldsymbol{A_d} - \boldsymbol{I})\boldsymbol{B},\ \boldsymbol{C_d} = \boldsymbol{C},\ \boldsymbol{D_d} = \boldsymbol{D} \tag{3.2}$$

This is the general form of a linear state space model. In this particular case the output model is related to the reactions at the ends of the piece of cable used for the simulation while the input is related to the instantaneous motion of the cable. Two different methods are used for the state-space system identification:

- A state-space identification method based on a prediction error minimization (PEM).
- A state-space identification method based on a subspace method.

In the next subsections these two methods are briefly introduced and described.

3.1.1 PEM methods

PEM methods here briefly summarized from Ljung [78] are based on an iterative approach that uses a prediction error minimization (PEM) algorithm. The idea behind the method is to find a set of parameters $\boldsymbol{\theta}$ such that the prediction error $\boldsymbol{e}(t, \boldsymbol{\theta})$ is minimized:

$$\boldsymbol{e}(t, \boldsymbol{\theta}) = \boldsymbol{y}(t) - \hat{\boldsymbol{y}}(t|t-1; \boldsymbol{\theta}) \tag{3.3}$$

where $\boldsymbol{\theta}$ contains the parameters of the model, t is the time, $\boldsymbol{y}(t)$ is the measured output and $\hat{\boldsymbol{y}}(t|t-1; \boldsymbol{\theta})$ is the prediction of $\boldsymbol{y}(t)$ given the data up to $t-1$ and the parameters $\boldsymbol{\theta}$. Once the measured input and output are known, and once the model structure is fixed, one can evaluate the parameters by minimization of:

$$\hat{\boldsymbol{\theta}} = \underset{\boldsymbol{\theta}}{\operatorname{argmin}} \frac{1}{n} \sum_{t=1}^{n} F(\boldsymbol{e}(t, \boldsymbol{\theta})) \tag{3.4}$$

where F is a properly chosen loss function. In this particular case the loss function is simply $F(\boldsymbol{e}) = \boldsymbol{e}^2$. The method is developed following these steps:

- Choice of the structure model
- Choice of the predictor

- Choice of the loss function

3.1.2 Subspace methods

Subspace methods, here briefly summarized from van Overschee[124], are non-iterative algorithms based on the idea of estimating a set of state vectors starting directly from the measured input-output measurements. Once the state vectors are known one can construct the following system:

$$\begin{bmatrix} \overline{\boldsymbol{x}}(t+1) \\ \boldsymbol{y}(t) \end{bmatrix} = \begin{bmatrix} \boldsymbol{A} & \boldsymbol{B} \\ \boldsymbol{C} & \boldsymbol{D} \end{bmatrix} \begin{bmatrix} \overline{\boldsymbol{x}}(t) \\ \boldsymbol{u}(t) \end{bmatrix} \tag{3.5}$$

in which $\overline{x}$ is the estimate of the state vector, $\boldsymbol{u}$ is the measured input vector and $\boldsymbol{y}$ is the measured output vector. In this system everything is known apart from the system parameters $\boldsymbol{\Theta} = \begin{bmatrix} \boldsymbol{A} & \boldsymbol{B} \\ \boldsymbol{C} & \boldsymbol{D} \end{bmatrix}$ then one can construct a least-squares estimate of $\boldsymbol{\Theta}$:

$$\boldsymbol{\Theta} = \left(\sum_{t=0}^{N-1} \begin{bmatrix} \overline{\boldsymbol{x}}(t+1) \\ \boldsymbol{y}(t) \end{bmatrix} \begin{bmatrix} \overline{\boldsymbol{x}}^T(t) & \boldsymbol{u}^T(t) \end{bmatrix} \right) \left(\sum_{t=0}^{N-1} \begin{bmatrix} \overline{\boldsymbol{x}}(t) \\ \boldsymbol{y}(t) \end{bmatrix} \begin{bmatrix} \overline{\boldsymbol{x}}^T(t) & \boldsymbol{u}^T(t) \end{bmatrix} \right)^{-1} \tag{3.6}$$

The state vectors can be identified starting from the input-output measurements using standard linear algebra tools such as orthogonal-triangular decomposition and singular value decomposition. For more details one may see [124] and [69].

3.1.3 Determination of the system size

The methods presented in Subsections 3.1.1 and 3.1.2 work as long as the dimension of the state vector is known. The size of the state vector is a priori normally not known and one should perform the identification procedure using different sizes of the state vector in order to obtain the optimal size. In order to avoid this trial and error procedure the optimal size of the state vector can

be derived by looking at eigenvalues of the Hankel matrix. The only thing one knows a priori are the input and the output data of the system. Using the input and output data the Markov parameters are identified following the procedure presented in [67, 96] and become the entries of the Hankel matrix. Supposing zero initial conditions, and knowing only input-output data, the output equation can be rewritten in matrix form as:

$$\boldsymbol{y} = \boldsymbol{Y}\boldsymbol{U}_N \tag{3.7}$$

where $\boldsymbol{y} \in \mathbb{R}^{q\times N}$ is the output matrix containing q outputs each with N measurements. $\boldsymbol{U}_N \in \mathbb{R}^{mN\times N}$ is a matrix containing m inputs, each with N measurements data rewritten in a upper triangular form, and $\boldsymbol{Y} \in \mathbf{R}^{q\times mN}$ are the Markov Parameters of the system:

$$\boldsymbol{y} = \begin{bmatrix} y(0) & y(1) & \dots & y(N-1) \end{bmatrix} \tag{3.8}$$

$$\boldsymbol{U}_N = \begin{bmatrix} u(0) & u(1) & \dots & u(N-1) \\ & u(0) & \dots & u(N-2) \\ & & \ddots & \vdots \\ & & & u(0) \end{bmatrix} \tag{3.9}$$

$$\boldsymbol{Y}_{N-1} = \begin{bmatrix} D & CB & CAB & \dots & CA^{N-2}B \end{bmatrix} \tag{3.10}$$

In a system with a single input the U matrix is a square matrix and the Markov parameters can be derived through its inversion $\boldsymbol{Y} = \boldsymbol{y}\boldsymbol{U}^{-1}$. In case of a Multi Input Multi Output (MIMO) system, that is asymptotically stable, one can assume that for a certain value of p the entries of $\boldsymbol{A}$ become sufficiently small that the Markov Parameters can be calculated as:

$$\boldsymbol{Y} = \boldsymbol{y}\boldsymbol{U}^{+} \tag{3.11}$$

where the matrix $\boldsymbol{U}^{+}$ is the pseudoinverse matrix of $\boldsymbol{U}$. Once the Markov parameters are determined one can construct the Hankel matrix using the procedure reported in [67]. Applying a singular value decomposition to the Hankel matrix and looking to the eigenvalues one can understand the optimal order of the system. The rank of the Hankel matrix is in fact related to the order of the system. In case of full rank matrix which is often the case with real measurements data, checking the dimension of the eigenvalues one can discard all the eigenvalues smaller than a certain value.

3.1.4 Estimation Focus and Best Fit

Once the size of the system is fixed, one needs to define the method for the identification of the parameters. As mentioned in Subsections 3.1.1 and 3.1.2, regardless from the method used, the identification is a minimization process that minimizes the difference between the measured output and the model response. However, there is not a unique way to define the model response. Here it is discussed the different possibilities for the estimation using the terminology as presented in the MATLAB Identification Toolbox [77]. The estimation focus defines how the error between the measured output and the simulated response is evaluated. Using a prediction focus the difference between the measured output and the 1 step ahead prediction is minimized. Using a simulation focus the difference between the measured output and the simulated response is minimized.

The quality of the identified system is here quantified using the best fit value:

$$\text{B.F.} = \left(1 - \frac{|y - \hat{y}|}{|y - \overline{y}|}\right) \cdot 100 \tag{3.12}$$

where y is the measured output, $\hat{y}$ is the simulated or predicted model output and $\overline{y}$ is the mean of the measured output.

3.1.5 Checking the stability of the system

Once the system is identified, one first step is to check the stability of the identified system. In this thesis the linear time invariant system of Equation 3.1 is considered. In this subsection few recalls about internal and external stability of linear systems is given. The concepts reported can be found in many textbooks on dynamical systems [138, 21]. In order to study the stability of such a system the eigenvalues of the $\boldsymbol{A}$. Here some matrix must be analysed:

- The system is asymptotically stable if all real parts of the eigenvalues of $\boldsymbol{A}$ are negative.
- The system is marginally stable if all real parts of the eigenvalues of $\boldsymbol{A}$ are non-positive and one or more of them have zero values.

The above statements are valid for a system without any input. For a system with inputs, the stability condition must be rewritten. In this case one talks about bounded-input, bounded-output (BIBO) stability.

- A system with inputs is bounded-input, bounded-output stable if, in case of a bounded input $\boldsymbol{u}(t)$, it produces a bounded output $\boldsymbol{y}(t)$. A signal is bounded if exists $B > 0$ such that:

$$\left|\boldsymbol{u}(t)\right| \leq B \quad \forall t \in \mathbb{R} \tag{3.13}$$

  The system has a BIBO stability if exists $M > 0$ such that the output satisfies:

$$\left|\boldsymbol{y}(t)\right| \leq M \quad \forall t \in \mathbb{R} \tag{3.14}$$

3.2 Deterministic Non-linear Parameter Identification

Although linear state-space systems are also capable of reproducing a wide range of non-linear models they have some important limitations, especially dealing with the phenomena of VIV.

3.2.1 The van der Pol Model

As highlighted by many authors [60, 35, 116, 115], the van der Pol equation has some important features that makes it particularly suitable for vortex shedding problems. It is in fact able to reproduce the self-excited and self-limited nature of the VIV response. In this thesis, the van der Pol equation is rewritten as a forced non-linear state-space model:

$$\begin{pmatrix} \dot{x_1} \\ \dot{x_2} \end{pmatrix} = \begin{pmatrix} x_2 \\ \mu(A - x_1^2)x_2 - \omega_0^2 x_1 + Bu \end{pmatrix} \tag{3.15}$$
$$y = x_1$$

where $\boldsymbol{x}$ is a non-linear state-space vector with two components. In particular $x_1 = F_c$ and $x_2 = \dot{F}_c$ where F_c is a force coefficient which in general may be either for the IL or the CF direction. u is the forcing term of the wake oscillator equation; in theory it may be any physical quantity but it is evident from the theory that the wake is influenced by the motion of the structure within the flow. μ, A, ω_0^2 and B are unknown parameters which needs to be determined. The parameters are determined using a non-linear least-squares solver as presented by Coleman and Li [27, 28]. If all the parameters are collected in a vector $\boldsymbol{p}$ the parameter identification problem can be rewritten as:

$$\min_{\boldsymbol{p}} \frac{1}{2}||\boldsymbol{R}(\boldsymbol{p})||_2^2 = \frac{1}{2}\sum_i r_i(\boldsymbol{p})^2 \tag{3.16}$$

where $\boldsymbol{R}(\boldsymbol{p})$ is a function which returns a vector value. In this case $\boldsymbol{R}(\boldsymbol{p})$ is the residual function which returns the difference between the measured and the simulated output:

$$\boldsymbol{R}(\boldsymbol{p}) = \boldsymbol{F_c}(t) - \boldsymbol{y}(\boldsymbol{p}, t) \tag{3.17}$$

where $\boldsymbol{y}$ is the output of the non-linear system and t is the time. This optimization problem is solved herein using a trust region reflective algorithm as presented in [27, 28].

3.3 Numerical Results

In this section, the numerical results obtained using the previously discussed methods are reported and discussed. Before presenting the results it is important to clarify the methodology used to validate the ROM and to test its accuracy. Two different approaches are used for the validation of the model and are reported in Figures 3.1 and 3.2 respectively. The starting points for both approaches are always the input motions used to force the small-scale high-fidelity model which, as already said, should match the statistical motion expected in full-scale. Forcing the high-fidelity model one obtains the force coefficients along the IL and CF direction that can be used to identify the ROM. Once the ROM is identified two approaches are possible for the validation:

- To force the ROM using the same input motion used for the identification of the process, and then to compare the results of the ROM with the results of the high-fidelity model in terms of force coefficients. (Figure 3.1)

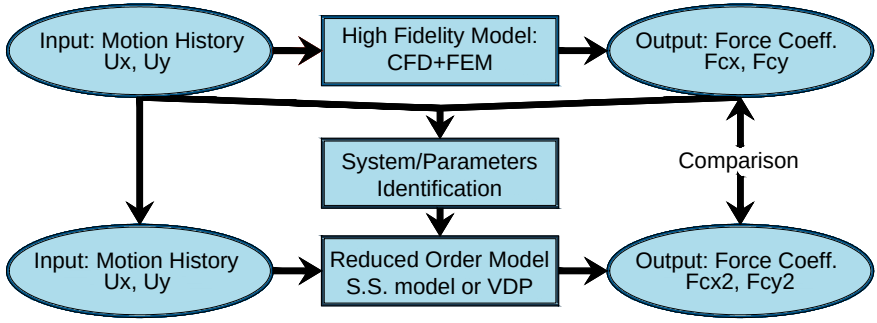

Figure 3.1: Validation through force coefficients

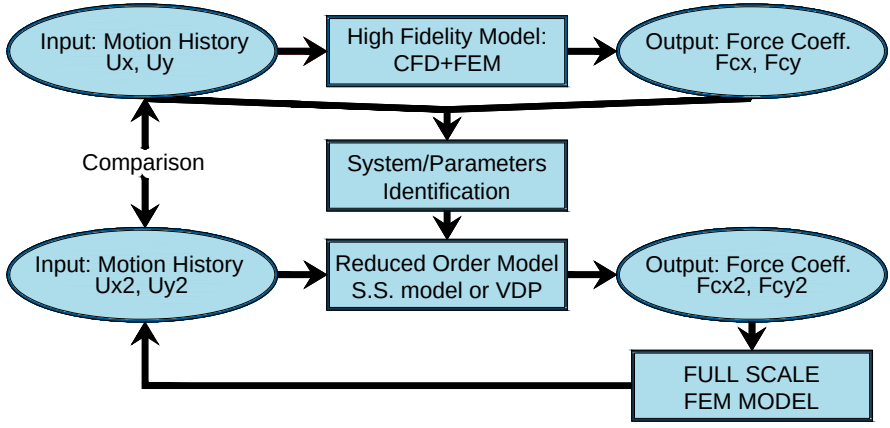

Figure 3.2: Validation through displacements

- To force the finite element model of the structure in full-scale using the developed ROM and to compare the obtained displacements with the displacements coming from full-scale measurements. (Figure 3.2)

The first approach is always possible; the second one is possible only when real scale measurements are available.

3.3.1 Spring-Supported Model

In many cases, full-scale measurements are not available and since the accuracy of the proposed method is based on the input motion used to force the small-

scale model it is necessary to find an accurate way to predict the expected displacements in full-scale.

Without any information, a possible way could be to use a white noise that would excite all the possible frequencies of the system. However, this approach is computationally expensive. A simulation time which is long enough to cover all the possible physical frequencies of the system has to be used. Moreover, this approach may produce non-physical and high frequencies that may lead the FSI solver to diverge. The problem is assessed here using the method of the flowchart presented in Figure 3.3.

The statistical properties of the imposed motion are also obtained through high-fidelity simulations on a small-scale size (PHASE 2). The cable is retained at both ends with suitable springs that replace the remaining parts of the cable.

The stiffness properties of the springs are deduced from the FEM model in full-scale (PHASE 1). It is supposed that, in small-scale, only translations along the x and y axes and rotations around the x and y axes are permitted at the ends of the cable. This assumption does not in any way limit the motion of the cable in full-scale that can move with all the possible degrees of freedom. It is simply assumed that the fluid forces exerted on the cylinder, due to the translation along its axis, and due the rotation around its axis, can be neglected. Once the statistical properties of the full-scale motions are known it is possible to create a random motion for each released degree of freedom that matches the measured power spectra densities. These random motions are imposed on the high-fidelity small-scale model, and the forces are measured (PHASE 3). The FEM full-scale model is built using the structural properties of a catenary mooring line. The cable is hinged at both ends and the contact with the ground is modelled using a penalty method approach. The data does not reproduce an existing structure but the parameters are chosen in order to reflect situations that can be found in standard offshore applications. First, the catenary shape of the cable is found, performing an analysis with gravity loads only, then a load F for each released degree of freedom is applied and the displacement S is measured. The force is applied at $\frac{2}{3}$ of the water depth from the ground. Operating in such a manner it is possible to deduce an equivalent linear stiffness for each released degree of freedom dividing the applied load by

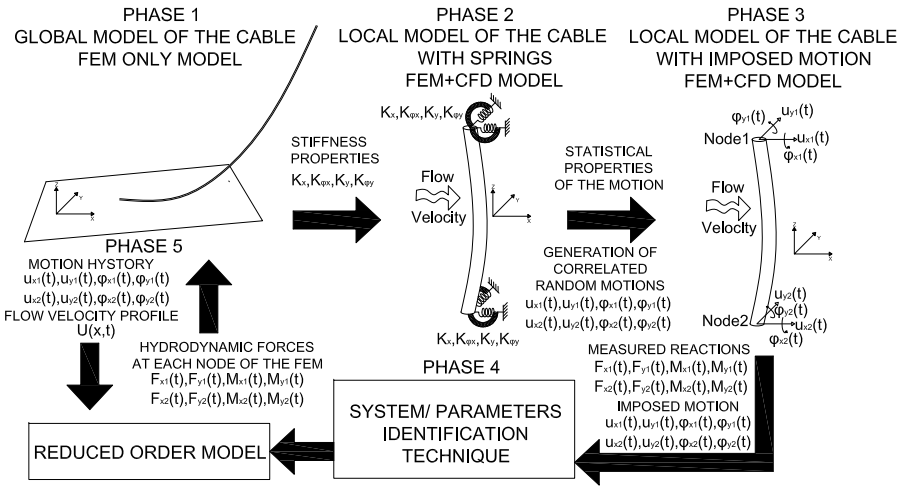

Figure 3.3: Validation through displacements

the relative displacement $K_i = F_i/S_i$. The obtained stiffness are equal to:

$$\begin{aligned} K_x &= 576\text{N/m} \; K_{\varphi x} = 803\text{Nm/rad} \\ K_y &= 409\text{N/m} \; K_{\varphi y} = 10417\text{Nm/rad} \end{aligned} \tag{3.18}$$

A linear stiffness is used because it is assumed that, the behaviour of the cable is linear around the mean deformed shape. It is important to highlight that this assumption does not imply that the structural behaviour of the mooring line is linear, but only that the behaviour around the mean deformed shape, caused by the VIV phenomenon, is linear. A FSI simulation with the same parameters as discussed in Section 2.1 is performed, and the displacements at both ends of the cable are measured. The flow velocity at the inlet is equal to $V = 0.5$m/s. This phase is important in order to understand the statistical properties that an imposed motion at both ends should have and to verify the ability of the present small-scale model to reproduce the full-scale behaviour. Results are reported in time and frequency domain in Figures 3.4, 3.5, 3.6 and 3.7. The DC component is subtracted from the results. It is interesting to note that the in-line displacements at the ends are in-phase at both ends while the cross-flow displacement is π rad out of phase. This means that the cable is vibrating in such a way that in full-scale it would be represented by a travelling wave. In Figures 3.6 and 3.7 the one-sided power spectral density (PSD) of the measured displacements and rotations are plotted. The spectra resemble

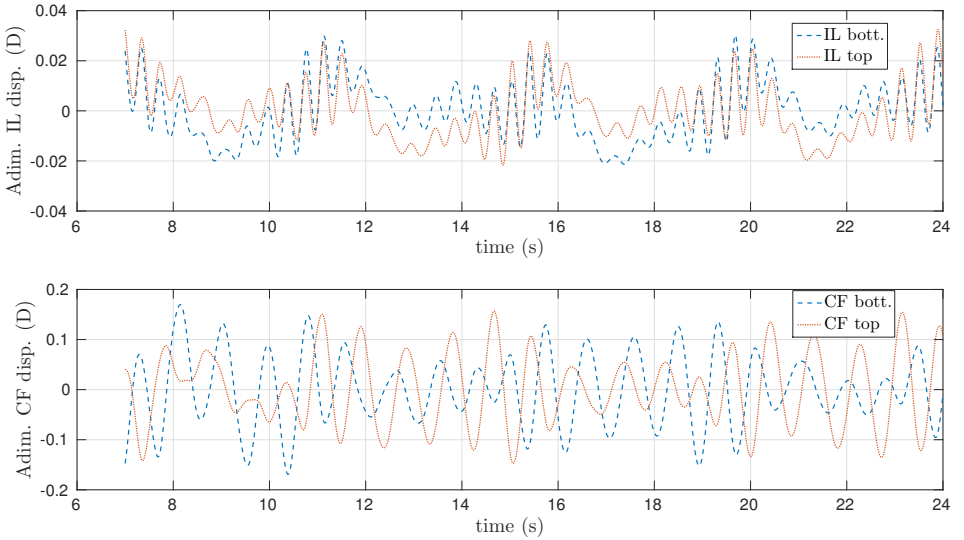

Figure 3.4: Results of the springs supported model in the time domain - Displacements

the behaviour which is normally observed in real full-scale measurements [120]. In the in-line displacements spectrum one can observe two peaks: the first peak is close to the natural frequency of the system $f_{N_{IL}} = 0.4$Hz while the second peak is close to twice the Strouhal frequency $f_{St} = St \cdot D/U = 1$Hz. For the cross-flow displacement one observes a similar behaviour but with a smaller first peak. As expected, the second peak has a frequency close to the Strouhal frequency. In the time domain plot the rotations have a relatively small value.

Once the displacements of the spring-supported model are known is possible to evaluate their statistical properties in order to generate correlated random motions to force the ends of the small-scale model. Firstly the correlation coefficients, which quantify the correlation among degrees of freedom, are computed:

$$\rho_{i,j} = \frac{\text{cov}(u_i, u_j)}{\sigma_{u_i}\sigma_{u_j}} \tag{3.19}$$

where u_i and u_j are two generic measured motions at the ends of the small-scale spring-supported model and σ_{u_i} and σ_{u_j} are the relative standard deviations. Then the one-sided power spectral density of each measured motion is constructed using a discrete transform procedure and the values $S_i(\omega)$ are computed for each motion. The matrix containing the correlated random phases

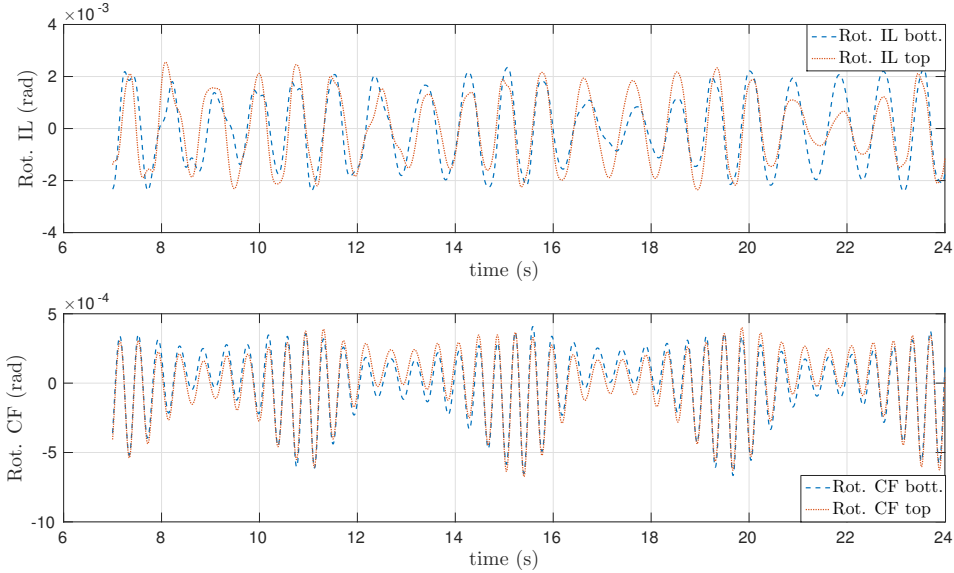

Figure 3.5: Results of the springs supported model in the time domain - Rotations

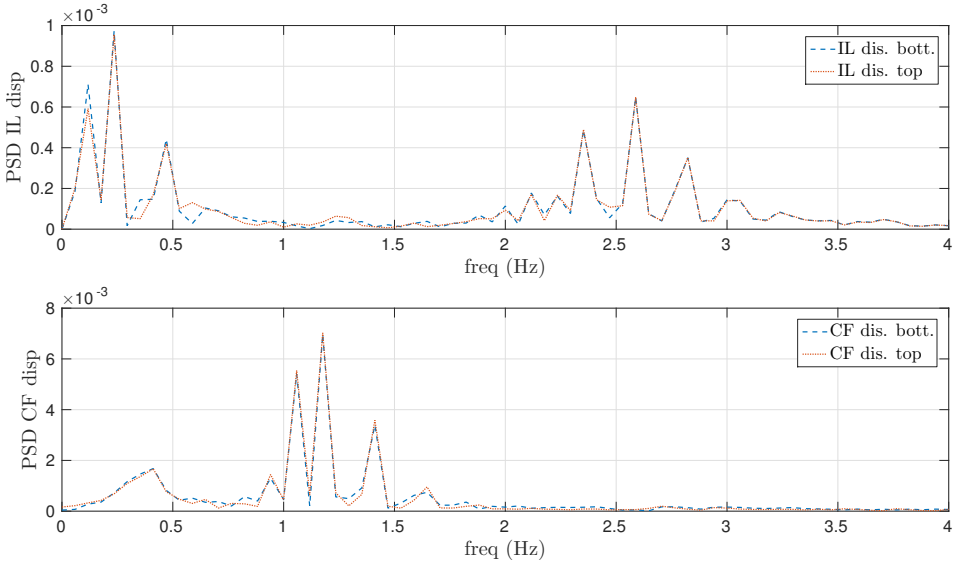

Figure 3.6: Results of the springs supported model in the frequency domain - Displacements

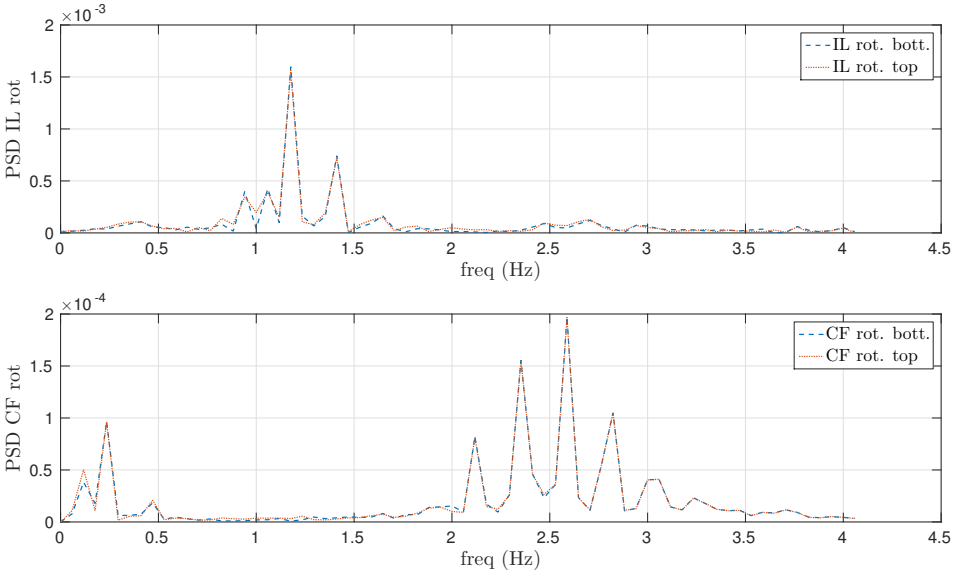

Figure 3.7: Results of the springs supported model in the frequency domain - Rotations

can then be constructed using the Cholesky decomposition of the correlation matrix:

$$\Phi_c = \Phi_{un} U \tag{3.20}$$

where Φ_c is the matrix containing the correlated random phases of the motions, Φ_{un} is a matrix containing uncorrelated random phases and U is the upper triangular matrix related to the Cholesky decomposition of the correlation matrix. The complex amplitudes can be reconstructed as:

$$X_i(\omega) = S_i(\omega) e^{-\phi_i \imath} \tag{3.21}$$

where ϕ_i is the random phase vector associated with the i motion. Finally the time signal can be reconstructed taking the real part of the inverse Fourier transform of the complex amplitudes:

$$u_i(t) = \Re \left(\frac{N}{2} \text{IFFT}(X_i(\omega)) \right) \tag{3.22}$$

where N is the number of time samples and IFFT is the inverse fast Fourier transform.

3.3.1.1 Influence of rotations

At this stage, only the torsional and vertical degrees of freedom at the end of the small-scale model are constrained. It means that each end of the small-scale-model has 4 degrees of freedom, the translations along the IL and CF directions and the rotations around the IL and CF directions. It means that once the statistical properties of the motion are known it is necessary to generate eight correlated random motions. In order to reduce the complexity of the system a check regarding the influence of bending rotations is performed. The only difference is that the springs are replaced with an imposed motion. In particular two identical simulations with and without bending rotational degrees of freedom are performed. In the first case, eight correlated random motions are generated and applied to the small-scale high-fidelity model. In the second case, only translational motions are applied and rotational degrees of freedoms are constrained. The reactions at the ends, for the two simulations, are measured and compared. The setting of the FSI simulations is the same as the spring-supported model. The comparison permits the understanding of the influence of the rotational degrees of freedom on the measured reaction forces and eventually, when the influence is small, to neglect them. The comparison for the IL and CF direction respectively for the upper and for the lower nodes is reported in Figures 3.8 and 3.9. The comparison is performed in terms of translational reaction forces along the IL and the CF direction with respect to time. As can be seen from the graph, there are only some slight differences between the two cases. For this reason, in order to simplify the problem, only translational degrees of freedom are considered from now on.

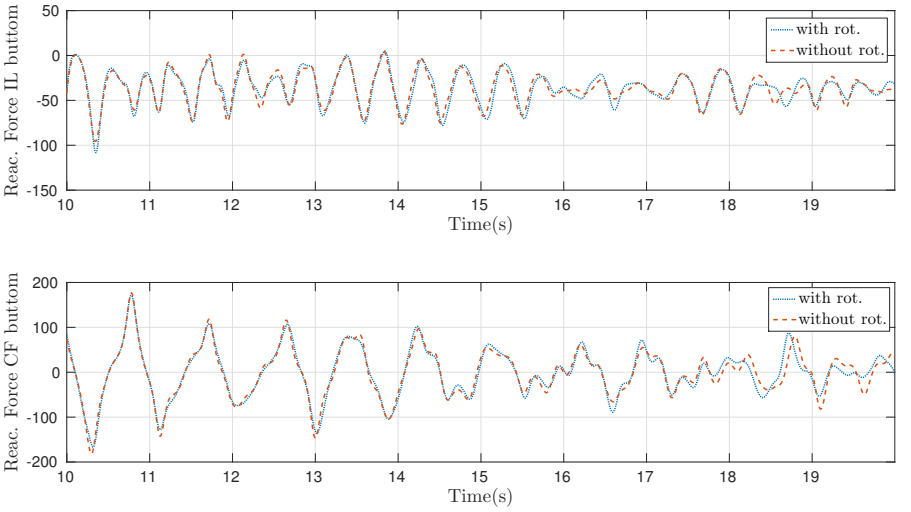

Figure 3.8: Influence of rotational dofs for the upper node

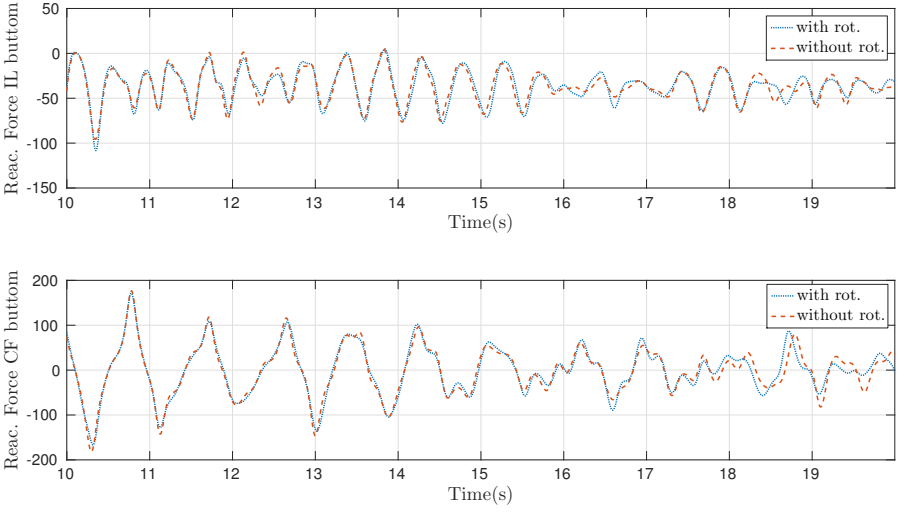

Figure 3.9: Influence of rotational dofs for the lower node

3.3.2 Results of the first proposed state-space model

The identification is performed using a linear state-space model derived from Equation 3.1 and rewritten in a more general form with the disturbance term $\boldsymbol{e}(t)$ also added as:

$$\begin{aligned} \dot{\boldsymbol{x}}(t) &= \boldsymbol{A}\boldsymbol{x}(t) + \boldsymbol{B}\boldsymbol{u}(t) + \boldsymbol{K}\boldsymbol{e}(t) \\ \boldsymbol{y}(t) &= \boldsymbol{C}\boldsymbol{x}(t) + \boldsymbol{D}\boldsymbol{u}(t) + \boldsymbol{e}(t) \end{aligned} \tag{3.23}$$

The optimal system size is chosen from systems with size included between 1 and 40 and has turned out to be 32. The input vector $\boldsymbol{u} \in \mathbb{R}^{N\times 12}$ and output $\boldsymbol{y} \in \mathbb{R}^{N\times 4}$ vectors are respectively:

$$\boldsymbol{u} = [v_{1x}\ v_{1y}\ v_{2x}\ v_{2y}\ a_{1x}\ a_{1y}\ a_{2x}\ a_{2y}\ v_{1x}^2\ v_{1y}^2\ v_{2x}^2\ v_{2y}^2] \tag{3.24}$$

$$\boldsymbol{y} = [R_{1x}\ R_{1y}\ R_{2x}\ R_{2y}\ ] \tag{3.25}$$

where v, a and R contains the components along the IL and CF direction, for the lower and upper node, respectively of velocity, acceleration and reaction forces. For the identification of the system matrices a PEM identification method with a simulation focus is used. The input vector is chosen in order to partially reproduce the terms inside the Morison equation [86] which is a semi-empirical equation normally used to compute hydrodynamic forces acting on a moving slender body in a flow. According to Morison, IL forces acting on a circular cylinder which is moving inside a flow can evaluated using:

$$F = \rho C_m \rho \frac{\pi}{4} D^2 a + \rho C_d A v|v| \tag{3.26}$$

where C_m is the added mass coefficient and C_d is the drag coefficient. In Figure 3.10 and 3.11 the comparison is reported, in the time domain, between the measured and simulated reaction forces at the end of the small-scale model for the IL and CF directions respectively. The same comparison but in the frequency domain is reported in Figures 3.12 and 3.13. The best fit values are reported in Table 3.1. If the same directions for the upper and the lower nodes are considered the results are similar. The model works better for the CF direction than for the IL direction. Regarding the CF direction, as depicted in Figure 3.13, the model is able to capture not only the vortex shedding frequency but also higher frequencies. Concerning the IL direction, as can be seen in Figure 3.12, the model captures the amplitude and the frequency of the

vortex shedding phenomena well but is not able to capture lower frequencies that are related to the natural frequency of the structure.

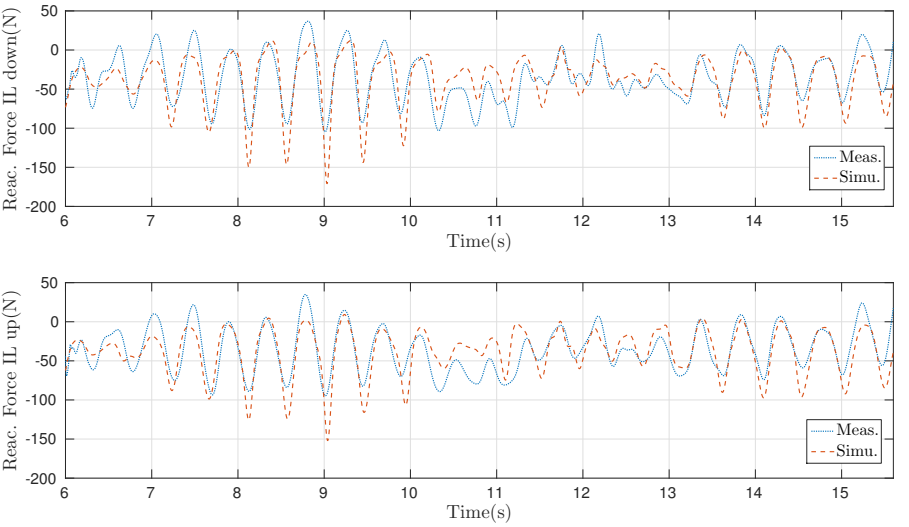

Figure 3.10: Comparison of Meas. and Sim. data for IL direction

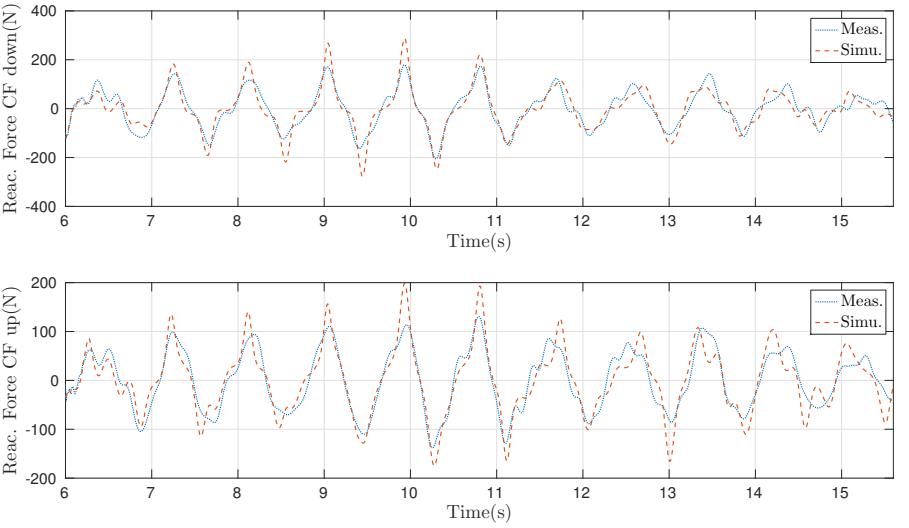

Figure 3.11: Comparison of Meas. and Sim. data for CF direction

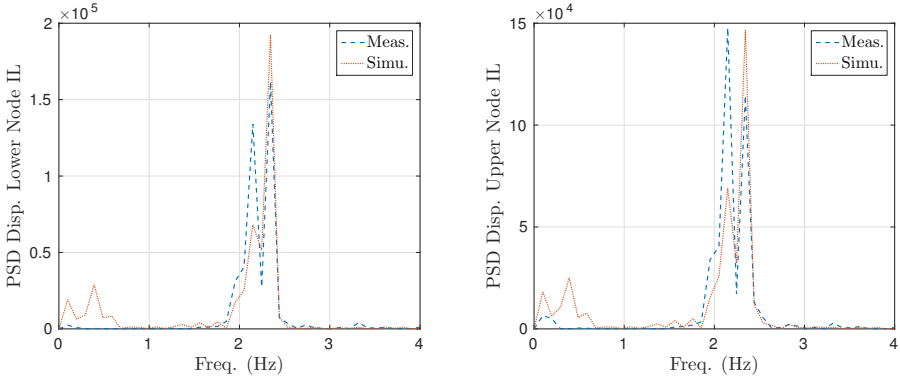

Figure 3.12: Power spectral density of the measured and simulated response for the IL dir.

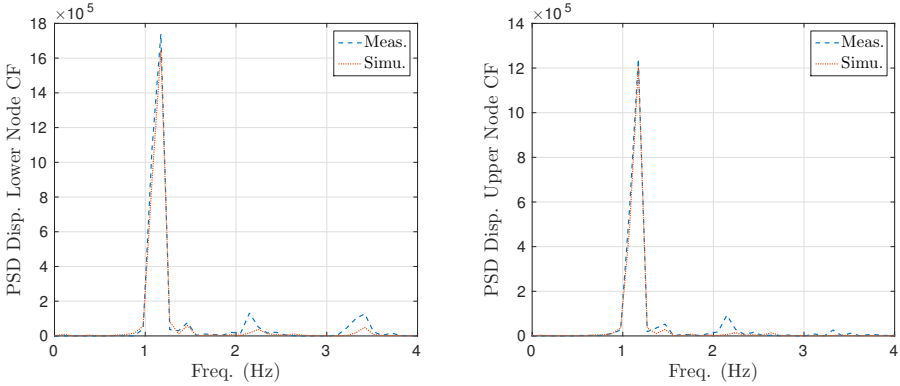

Figure 3.13: Power spectral density of the measured and simulated response for the CF dir.

Name	Best Fit
IL lower	31.79 %
IL upper	29.74 %
CF lower	58.84 %
CF upper	58.13 %

Table 3.1: Best fit values for lower and upper node, for IL and CF directions

3.3.3 Results of identification using the VDP model

The identification procedure is repeated using one VDP system for the IL direction and one VDP system for the CF direction. In this case, in order to have two single-input single-output (SISO) systems only one input variable is used for each direction and instead of reaction forces, respectively for IL and CF direction, the drag and lift coefficient are used. These coefficients are using the total in-line and cross-flow forces acting on the cylinder. The total force is obtained through pressure integration over the surface of the cylinder. Concerning the IL direction it is used only the fluctuating part of the drag obtained in a Reynolds decomposition framework. As already mentioned previously the input variable, which is forcing the wake oscillator, must be related to motion of the cylinder. Three different models that one can find also in literature are proposed. These three models use as input respectively the displacement, the velocity and the acceleration in the mid-point of the cylinder. The system of equations 3.15 is then rewritten for the IL and CF direction as:

$$\begin{pmatrix} \dot{x}_{1,IL} \\ \dot{x}_{2,IL} \end{pmatrix} = \begin{pmatrix} x_{2,IL} \\ \mu_{IL}(A_{IL} - x_{1,IL}^2)x_{2,IL} - \omega_{0,IL}^2 x_{1,IL} + B_{IL}u_{IL} \end{pmatrix} \tag{3.27}$$

$$D_c = x_{1,IL}$$

$$\begin{pmatrix} \dot{x}_{1,CF} \\ \dot{x}_{2,CF} \end{pmatrix} = \begin{pmatrix} x_{2,CF} \\ \mu_{CF}(A_{CF} - x_{1,CF}^2)x_{2,CF} - \omega_{0,CF}^2 x_{1,CF} + B_{CF}u_{CF} \end{pmatrix} \tag{3.28}$$

$$L_c = x_{1,CF}$$

where the subscript IL and CF are for the in-line and the cross-flow direction. The forcing term u, depending on the coupling model used, may be the displacement, the velocity or the acceleration of the central point of the cylinder. In literature, these models are used mainly to describe the cross-flow motion of 1 degree of freedom rigid cylinders. Facchinetti [35] studied these three models, concluding that, regarding the CF direction, the coupling model that gives the best results is the acceleration coupling model. The results, in terms of best fit, obtained for the three different models are reported in Table 3.2. As can be seen from the table the acceleration-coupling model gives the best fit. The fit is better along the CF direction than along the IL direction. The comparison between the measured and the simulated outputs is reported

in time domain in Figures 3.14, 3.15, 3.16 and in frequency domain in Figures 3.17, 3.18 and 3.19 respectively for displacement, velocity and acceleration-coupling. It is important to remember that the input motions used to force the high-fidelity model are generated starting from the displacement spectra coming from the results of the simulation performed using the spring-supported model of Subsection 3.3.1. Focusing on the time results, especially regarding the IL direction, it is clear that the oscillating frequencies observed in Figure 3.6 for displacements are also present in the drag coefficient and lift coefficient. The displacement-coupling model is able to capture the peak frequencies for both the IL and CF direction. It gives higher amplitudes of oscillation in the IL direction, while in the CF direction, since it is a model with only one frequency, it concentrates all the energy at the peak frequency (Figure 3.17). The velocity-coupling model in the CF direction is able to capture the peak frequency but fails to capture the phase of the drag coefficient. In fact, there is a phase shift between the measured and the simulated output (Figure 3.15). Concerning the IL direction, the acceleration-coupling model has similar results as the velocity-coupling model but exhibits better behaviour concerning the CF direction: the phase shift is not present and the amplitude of oscillation is better reproduced. All the VDP models proposed here have some common features:

- They are able to capture both the frequency and the amplitude of oscillation due to the vortex shedding phenomena but are not able to capture lower frequencies.
- They are self-excited and self-limited.
- They give better results for the CF direction.

Name	Best Fit
IL DC dis.	−7.96 %
CF LC dis.	33.23 %
IL DC vel.	6.59 %
CF LC vel.	12.92 %
IL DC acc.	8.07 %
CF LC acc.	34.12 %

Table 3.2: Best fit values for IL and CF directions

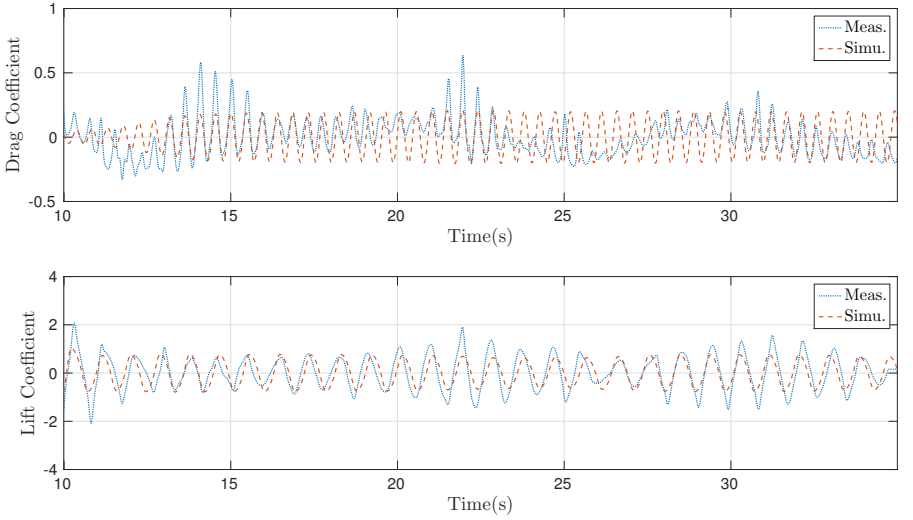

Figure 3.14: Comparison of Meas. and Sim. data for IL and CF using a VDP model with displacement-coupling

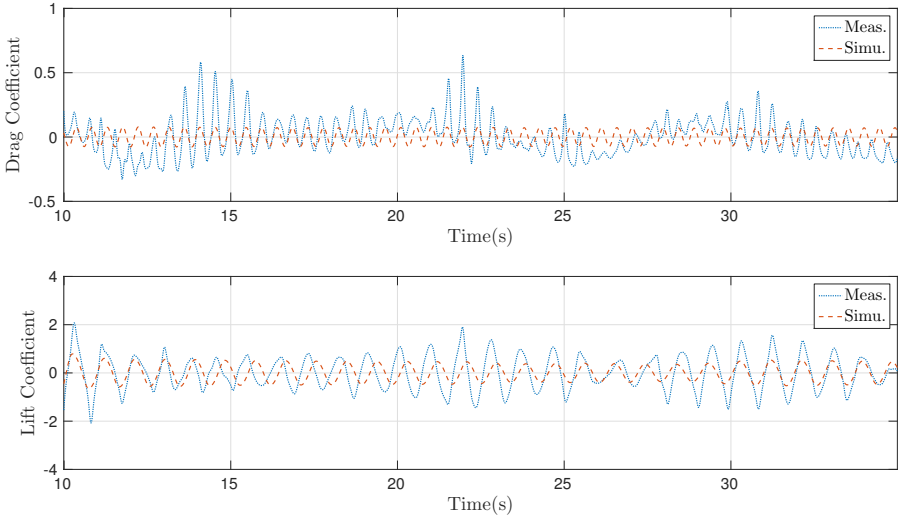

Figure 3.15: Comparison of Meas. and Sim. data for IL and CF using a VDP model with velocity-coupling

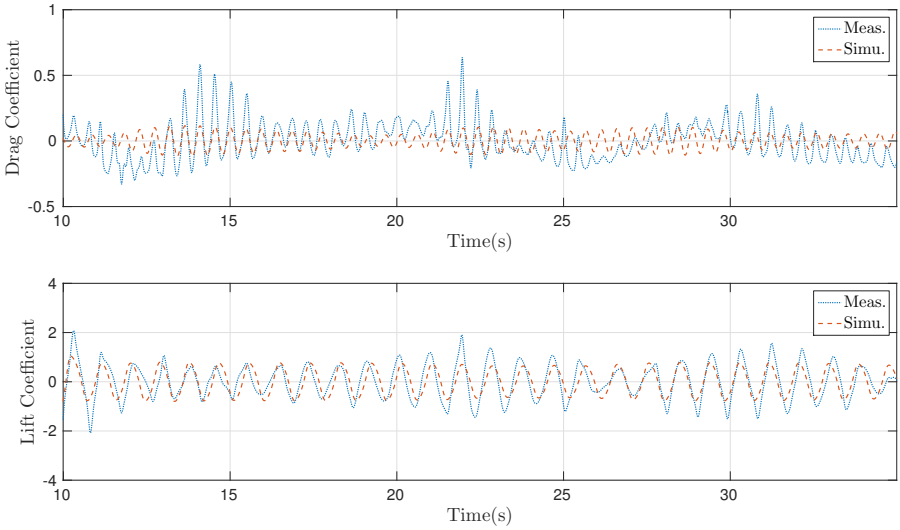

Figure 3.16: Comparison of Meas. and Sim. data for IL and CF using a VDP model with acceleration-coupling

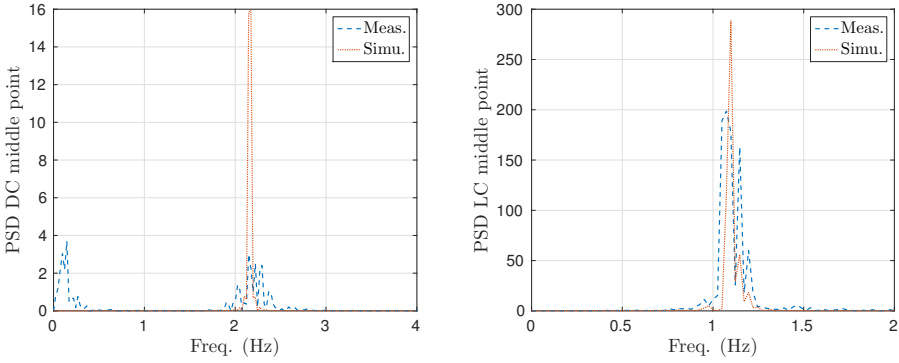

Figure 3.17: Power spectral density of the Measured and Simulated data using a VDP system with displacement-coupling

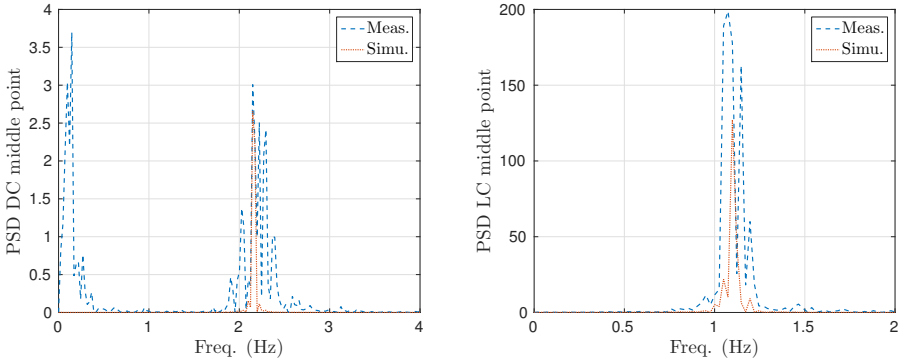

Figure 3.18: Power spectral density of the Measured and Simulated data using a VDP system with velocity-coupling

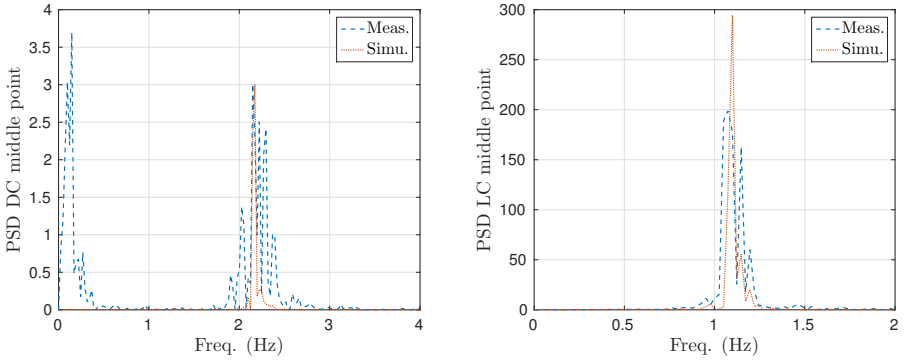

Figure 3.19: Power spectral density of the Measured and Simulated data using a VDP system with acceleration-coupling

3.3.4 Some preliminary conclusions and a new model proposal

These preliminary analyses are important in order to understand the main features of the proposed models and possibly to develop a new model. The VDP equation, in contrast to the state-space model, has only one main frequency of oscillation and it depends on the term ω_0^2. For this reason, especially in the case of an oscillation characterized by more than one main frequency, it is able to capture only the peak frequency. The state-space model on the other hand can capture all the frequencies of oscillation of the VIV phenomena because it has an arbitrary dimension. In comparison with the VDP model, especially concerning the IL direction, it produces a better fit. Unfortunately, it has one important limitation: it is a linear model without any self-excitation and self-limitation features. These two features are an important characteristic of the vortex shedding phenomena. For example if the cylinder was not moving, using a linear state-space model, no forces would act on it. This means that the state-space model gives good results only if it is forced with an input that differs from zero. The VDP model is used extensively in literature because it is both self-excited and self-limited. To use the advantages of both systems, a new model which is a combination of a linear state-space model and a VDP model is proposed here:

$$\begin{aligned} \dot{\boldsymbol{x}}(t) &= \boldsymbol{A}\boldsymbol{x}(t) + \boldsymbol{B}f(L_c(t)) + \boldsymbol{K}\boldsymbol{e}(t) \\ \boldsymbol{D_e}(t) &= \boldsymbol{C}\boldsymbol{x}(t) + \boldsymbol{D}f(L_c(t)) + \boldsymbol{e}(t) \end{aligned} \tag{3.29}$$

$$\begin{pmatrix} \dot{x}_{1,CF} \\ \dot{x}_{2,CF} \end{pmatrix} = \begin{pmatrix} x_{2,CF} \\ \mu_{CF}(A_{CF} - x_{1,CF}^2)x_{2,CF} - \omega_{0,CF}^2 x_{1,CF} + B_{CF}u_{CF} \end{pmatrix} \tag{3.30}$$

$$L_c = x_{1,CF}$$

In the proposed model, forces along the IL direction are modelled through the fluctuating drag coefficient using a linear state-space model which uses a function of the lift coefficient as input. Instead, the lift coefficient is modelled using a VDP system which is forced using the acceleration of the cylinder along the CF direction. Nayfeh et al. [87] modelled the unsteady force coefficients on a stationary cylinder using a VDP model for the lift coefficient and a term proportional to $L_c \cdot \dot{L}_c$ for the drag coefficient. Qin [97] stated that the linear relationship should be proportional to the term L_c^2 while Akhtar [2] concluded

that both terms contribute to the modelling of the lift. Since there is no universal agreement in literature, especially dealing with moving cylinders, here both models are proposed substituting the function $f(L_c(t))$ with $L_c^2(t)$ and $L_c(t) \cdot \dot{L}_c(t)$ respectively. The results of the identified models are proposed in Figure 3.20. In this case, the model which gives the best results is the one which uses C_l^2 as input function of the state-space model. The appropriate size of the model turns out to be equal to 8. Along the IL direction it was

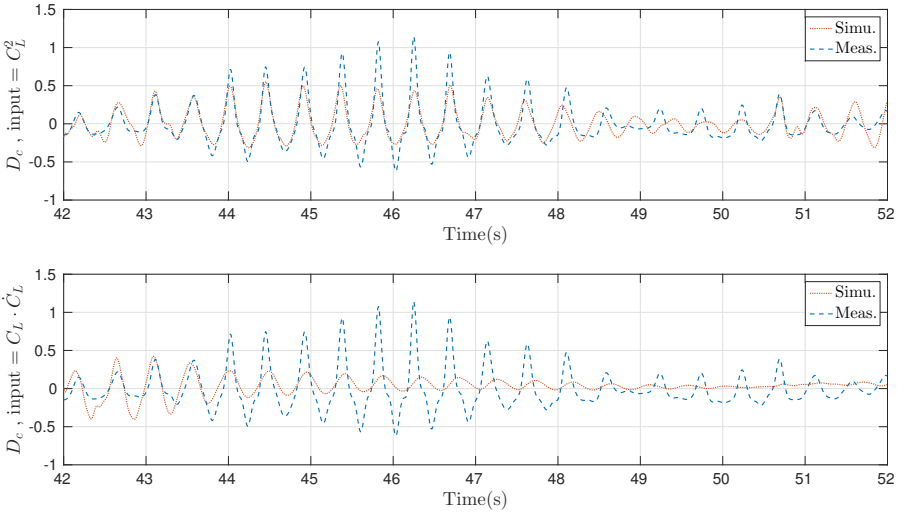

Figure 3.20: Comparison of the drag coefficient for two different models

decided not to use the model of subsection 3.3.2 although it gives good results. The reason is justified by the fact that some preliminary analysis in full-scale returned unreliable results and in some cases the model was not converging. The model of Equation 3.29 is in fact a linear model without self-excitation and self-limitation that in full-scale behaves following the sketch proposed in Figure 3.21. Following the sketch, the drag coefficient is evaluated using the identified state-space model that has as input vector values of velocities, accelerations and square of the velocities of the structure along the IL direction. These terms depend on the structural response evaluated through the global finite element model of the structure. This model creates a closed loop which in the case of a stable system would lead, after a certain period of time, to a zero response. This condition is not physical. Using a combination of a VDP model with a state-space model, which is uncoupled along the two directions, would also lead to the same problem. Moreover, it is evident that the forces

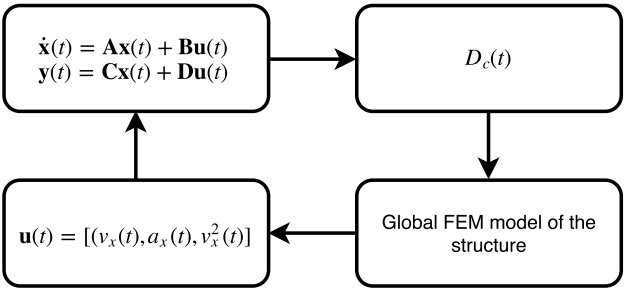

Figure 3.21: Sketch of the model proposed in subsection 3.3.2

along the IL and CF direction, since are both the result of the vortex shedding phenomenon must be coupled.

3.3.5 Validation of the proposed model in full-scale using the NDP dataset

The validation performed using the scheme reported in Figure 3.1 gives some informations about the quality of the identified model but does not give any information regarding the behaviour of the identified model in full-scale. In order to perform the validation of the scheme reported in Figure 3.2, measurements from full-scale activities are used, particularly the data set from experimental activities conducted by the Norwegian Marine Technology Research Institute (Marintek) inside their towing tank located in Trondheim. The set up of the experimental campaign is depicted in Figure 3.22. A 38m long riser is tested. The riser is free to move along the in-line and the cross-flow directions; only the torsional degree of freedom is constrained. Clump weights acting in tandem with pendulum arms, and placed at the ends, are used to moderate the tension variation along the riser. Uniform and linearly sheared flow velocity profiles are investigated. The uniform flow velocity profile is generated by towing the riser with a constant velocity along the towing tank while the linearly sheared flow is generated by a rotation of the crane around its vertical axis. Different riser types are tested: a bare riser and a riser partially or totally covered with helical strakes to investigate their effect on VIV suppression. Here the focus is only on the bare type. The mechanical and geometrical properties of the riser are reported in Table 3.3. The tension is varying along the riser during the tests but for the validation a constant tension is applied to the full-scale finite element model. Only the

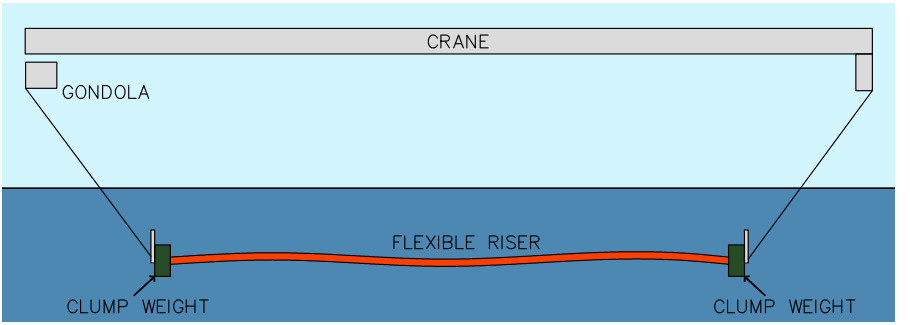

Figure 3.22: Setting of the NDP 38 m experiment setting. Image adapted from [123]

main features of the test setting are reported here - for more details see Trim et al. [123]. The instrumentation placed along the riser counts 24 strain

Quantity	Value	Unit
D	0.027	m
E	$8.894 \cdot 10^8$	$\frac{\mathrm{N}}{\mathrm{m}^2}$
A	$5.7 \cdot 10^{-4}$	m^2
J	$4.2 \cdot 10^{-8}$	m^4
ρ	$1.630 \cdot 10^3$	$\frac{\mathrm{kg}}{\mathrm{m}^3}$
length (l)	38	m
tension (T)	3000	N

Table 3.3: Structural characteristics of riser model

gauges and 8 accelerometers along the CF direction and 40 strain gauges and 8 accelerometers along the IL direction. The sampling rate is equal to 1200Hz. The accelerometers are placed at different positions along the riser length, particularly at $z = 5$m, 10m, 14m, 19m, 22m, 26m, 31m and 36m, where z is the axis along the length of the riser. Several flow velocities are tested in experimental conditions but only velocities equal to 1.4m/s and 1.7m/s are available to the author of this thesis. The time histories of the accelerations measured in the experiments are used to force the high-fidelity small-scale model and the force coefficients are measured.

The output of the developed high-fidelity simulations are used together with the time histories of motion to feed the system/parameter identification technique presented in Chapter 3, and the parameters and the system size of model presented in Equation 3.29 and 3.30 are determined. The developed model is then used to force the global finite element model of the structure and

the results are compared in terms of displacements with the results of the experiments.

3.3.5.1 Flow velocity V=1.4 m/s

The first comparison is performed in small-scale in order to check whether the model is also able to perform a comparison in full-scale. The comparison is performed both in time and frequency domains and is reported in Figures 3.23 and 3.24.

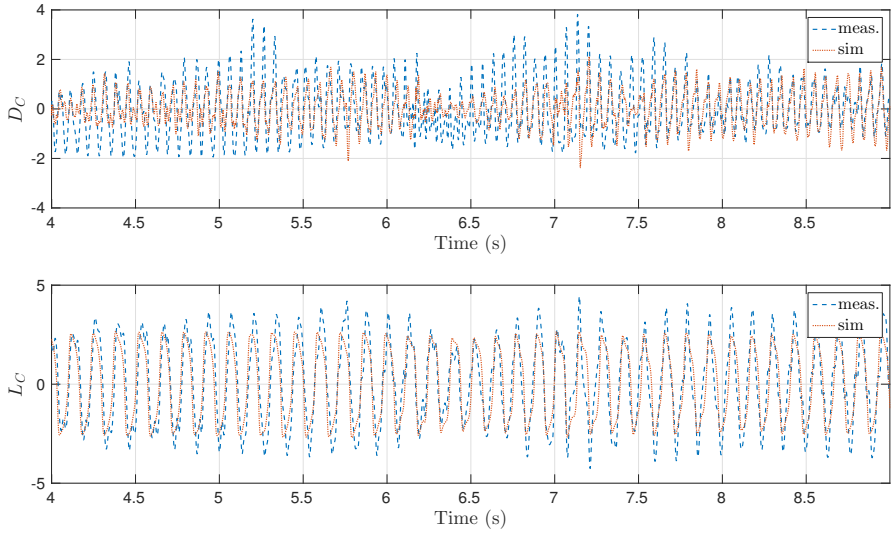

Figure 3.23: Comparison of results in small-scale in terms of force coefficients - Time Domain

Name	Best Fit
IL DC dis.	20.88 %
CF LC dis.	65.6 %

Table 3.4: Best fit values for IL and CF directions $v = 1.4$m/s

As mentioned in Subsection 3.3.5, the identified model is constructed using a linear state-space model forced by a term which depends linearly on the square of the lift coefficient for the IL direction and a forced van der Pol model along the CF direction. The optimal model size turns out to be equal to 6.

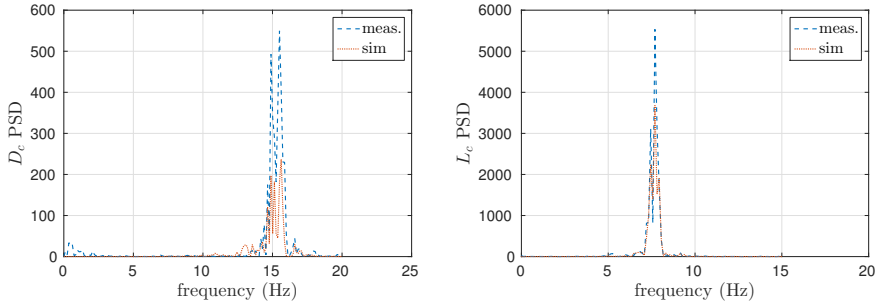

Figure 3.24: Comparison of results in small-scale in terms of force coefficients - Freq Domain

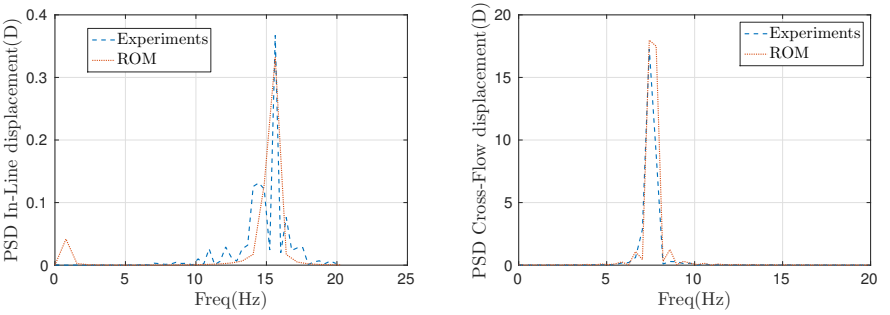

Figure 3.25: Comparison of results in full-scale in terms of displacements for z=19 m - Freq Domain

The non-linear deterministic identification procedure led to the parameters of the VDP model reported in Table 3.5. The simulation performed using

Name	Value
μ_{CF}	68.29
A_{CF}	1.18
$\omega^2_{0,CF}$	2117
B_{CF}	70.68

Table 3.5: Identified parameters of the VDP model for V=1.4 m/s

the identified model, especially along the CF direction, matches well with the high-fidelity data. As observed in the numerical results presented in Subsection 3.3.2 and 3.3.3, the identification along the IL direction produce a worse fit respect with the CF direction.

In order to perform the comparison in full-scale the finite element model

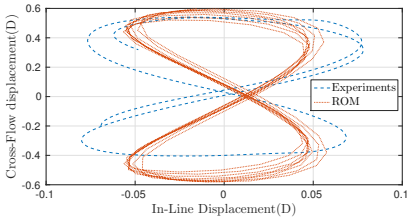

Figure 3.26: Comparison of the trajectory for z=19 m, v=1.4 m/s, between the simulated and the measured response

of the structure is built. The finite element model is constructed using 50 geometrically exact beam elements described in Chapter 2 and matching the mechanical properties reported in Table 3.3. At the ends of the full-scale model only translational and torsional degrees of freedom are retained. At each node of the structure hydrodynamic forces are modelled using the identified model and displacements are measured. The steady part of the drag is applied as a static load before the beginning of the VIV phenomena. The steady drag matches the mean value measured during the high-fidelity simulation. In this case, the mean value of the drag coefficient is equal to $D_{C,mean} = 2.34$. This value is higher than the values normally observed on static cylinders but this is a common feature of oscillating cylinders. The amplification of the mean (steady) drag coefficient was observed by many authors [70, 126]. In the full-scale model the mass of the riser is increased to take into account the added mass effect. Since force coefficients, are obtained through the integration of pressures around the cylinder surface, the added mass effect is not taken into account in the results of the high-fidelity data. To reintroduce this effect the mass of the cylinder is increased considering a constant added mass coefficient equal to $C_A = 1$. This value, without further analysis, is normally considered the standard value for moving cylinders in water [88].

The comparison is performed in the frequency domain in terms of displacement. It is performed only in the frequency domain because the initial conditions and the small transient may lead to a phase shift between the measured and simulated response. In Figure 3.25 the comparison of the power spectral density between the experiment and the simulation in terms of displacements is reported. Results are presented for $z = 19$, located at the midpoint of the full-scale model. As can be seen from the graphs, a good agreement between the simulated and measured response is observed. It is interesting to note that not only the main frequency and amplitude of oscillation are captured, but the trajectory of the motion also matches. The phase angle between the

measured and simulated response differ slightly.

3.3.5.2 Flow velocity V=1.7 m/s

The procedure performed in Subsection 3.3.5.1 is repeated here for the other available value of flow velocity. This second test is performed in order to check the sensitivity of the proposed model to the flow velocity and to check whether the realisation of a future model which would also consider the flow velocity as a parameter is possible. The same graphs reported in Subsection 3.3.5.1 are also reported here for both the small-scale and the full-scale. As can be seen in Table 3.6, results are similar to the case with a flow velocity of $v = 1.4$m/s.

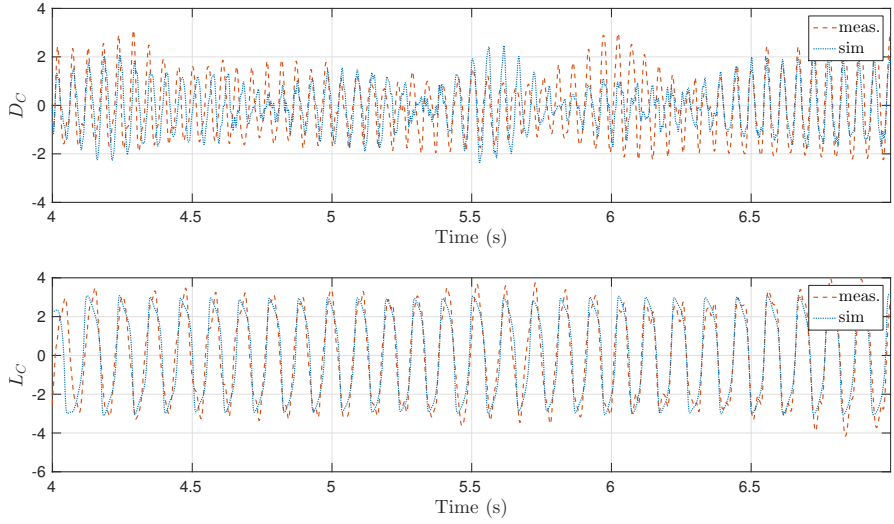

Figure 3.27: Comparison of results in small-scale in terms of force coefficients - Time Domain

The identified parameters of the VDP system are reported in Table 3.7.

Name	Best Fit
IL DC dis.	20.9 %
CF LC dis.	71.2 %

Table 3.6: Best fit values for IL and CF directions $v = 1.7$m/s

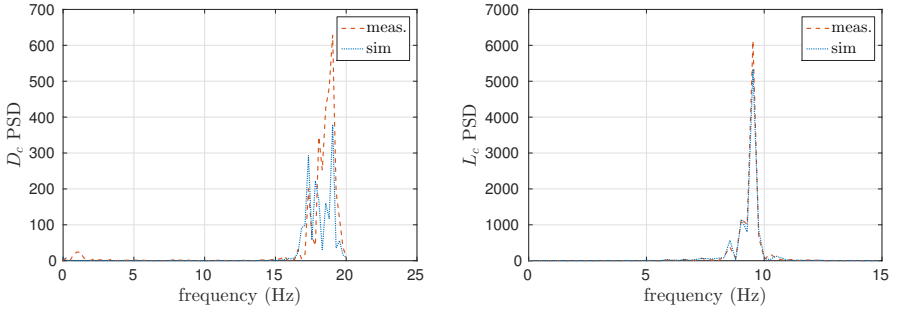

Figure 3.28: Comparison of results in small-scale in terms of force coefficients - Freq Domain

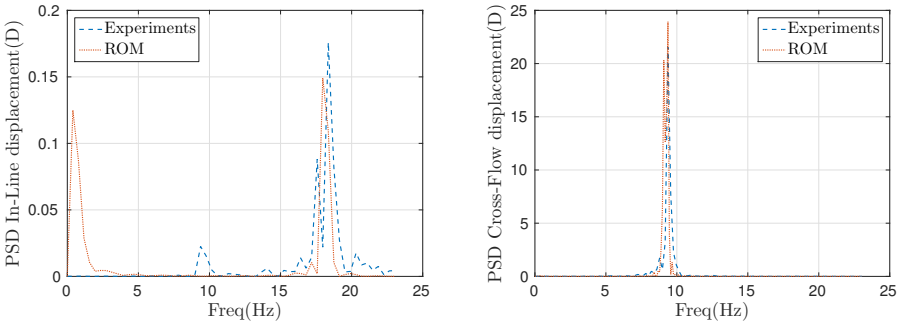

Figure 3.29: Comparison of results in full-scale in terms of displacements for z=19 m - Freq Domain

Name	Value
μ_{CF}	88.60
A_{CF}	1.35
$\omega^2_{0,CF}$	3540
B_{CF}	34.94

Table 3.7: Identified parameters of the VDP model for V=1.7 m/s

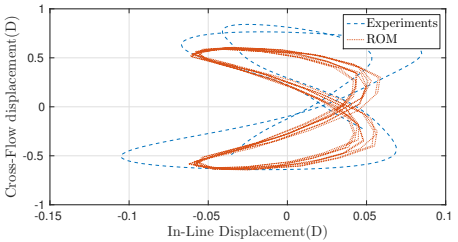

Figure 3.30: Comparison of the trajectory for z=19 m, v=1.7 m/s, between the simulated and the measured response

3.3.6 Discussion on the identified models

For both flow velocities the main features of vortex shedding phenomenon are captured and reproduced. The main frequencies of oscillation and the amplitudes, for both the IL and the CF direction, are well represented. It is interesting to notice that for both cases also the trajectory of the cylinder is represented in an accurate manner. Concerning the CF direction, some conclusions regarding the identified parameters can be drawn. The parameter $\omega_{0,CF}^2$ as suggested by Facchinetti [35] is related to the vortex shedding frequency f_s by the expression $\omega_{0,CF}^2 = (2\pi f_s)^2$. This value defines in fact the natural frequency of the unforced van der Pol oscillator. The parameter A_{CF}, related to the amplitude of the limit cycle, that in [35] is not considered a parameter but it is taken constant and equal to 1, for both velocities, assumes values bigger than 1. The damping term μ_{CF} assumes similar values for both the flow velocities while the term B_{CF}, that multiplies the acceleration term, differs between the two flow velocities. For the lower flow velocity its value is higher. This describes how big is the influence of the transversal cylinder motion respect to the response of the oscillator. It means that for higher velocities the influence of the transversal acceleration of the cylinder gets smaller. The previous consideration are performed analysing only two velocities in order to obtain a more general trend about the behaviour of the model parameters respect to the flow velocities a wider range of flow velocities should be considered.

3.3.7 Comparison of the proposed model with standard Morison's equation

In this subsection a new analysis using the proposed model for the two considered flow velocities is performed. In particular three different velocities are considered: a zero velocity, a constant velocity equal to 1.4m/s and a constant velocity equal to 1.7m/s following the sketch of Figure 3.31. The cable is clamped at the top and has a punctiform mass $M = 305.81kg$ on the other end. The mass is used to create tension on the cable. This produces a vertical force of $3000N$ which is equal to the medium tension applied in Subsections 3.3.5.1 and 3.3.5.2. The length and the mechanical properties of the cable are the same as those used in Subsections 3.3.5.1 and 3.3.5.2. The results of this analysis are compared to the results of the analysis which

neglects the vortex induced vibrations phenomena. In the second analysis hydrodynamic forces are evaluated using the standard Morison's equation applied only along the IL direction using the mean value of the drag coefficient evaluated on a rigid circular cylinder.

$$F_{IL} = \rho_w \frac{\pi}{4} D^2 \dot{V}_{IL} + \rho_w C_a \frac{\pi}{4} D^2 (\dot{V}_{IL} - a_{IL}) + \frac{1}{2} \rho_w C_d D (V_{IL} - v) |V_{IL} - v_{IL}| \tag{3.31}$$

in which V_{IL} is the flow velocity along the IL direction, a_{IL} and v_{IL} are the acceleration and the velocity respectively of the cable along the IL direction, D is the cylinder diameter, ρ_w is the water density, C_a is the added mass coefficient, and C_d is the drag coefficient. The current is steady, therefore the first term of the equation equals zero while the second term vanishes when the analysis reaches a steady solution. Once a steady solution is reached the third term becomes equal to:

$$\frac{1}{2} \rho_w C_d D V_{IL} |V_{IL}| \tag{3.32}$$

The value of the mean drag coefficient is taken, for both values of the flow velocities according to Wieselberger[133], equal to 1.2. The value of the mean drag coefficient is in fact, in the range $10^4 < Re < 10^5$ approximately constant. In this case the values of the Reynolds numbers were equal to $Re_{1.4} = 37800$ and $Re_{1.7} = 45900$. This test is performed in order to understand the influence of the vortex induced vibrations and specifically to measure how big is the effect of the drag amplification due to the VIV process.

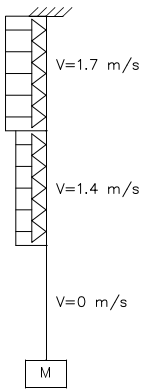

Figure 3.31: Sketch of the analysis used for the comparison

It is possible to see in Figure 3.32 the comparison between the two models.

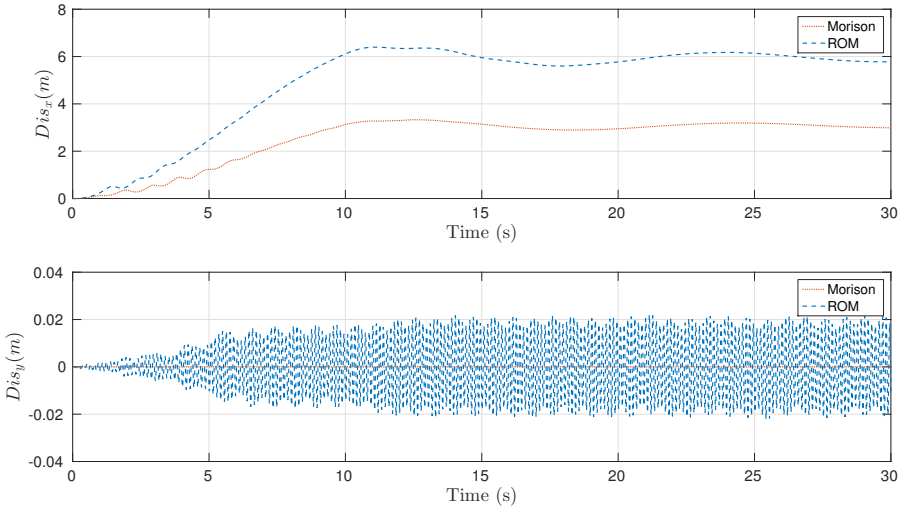

Figure 3.32: Comparison of results - Morison equation vs ROM for $z = 19$

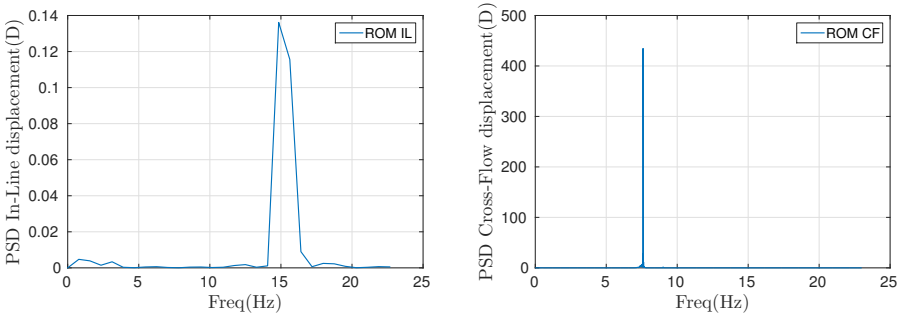

Figure 3.33: Results of the ROM for $z = 19$

Results are plotted for a point at the mid-point of the cable length for $z = 19$m. The Morison model, since it does not model the cross flow forces, it produces a response equal to zero along the cross flow direction. The only difference is not only along the CF direction but also along the IL direction. Due to the magnification of the mean drag coefficient, because of the VIV phenomenon, the structure exhibits bigger mean displacements also along the IL direction. Moreover, as it is possible to observe in Figure 3.33, where the results of the ROM are plotted in the frequency domain, it is observed a vibration also along the IL direction. In the Figure only the frequency relative to the VIV phenomenon is plotted; lower frequencies, related to the first natural frequencies of the structure are filtered. In Figure 3.34 it is reported the time

history of the reactions at the anchoring point for the three restrained degrees of freedom. The vortex induced vibration has a big influence also on the reaction at the anchoring point. The VIV produce, in comparison with the reactions evaluated with the Morison model (Tab. 3.8), an increase of the mean value. This simple test highlights the importance of the VIV in the evaluation of the design loads especially dealing with fatigue loads.

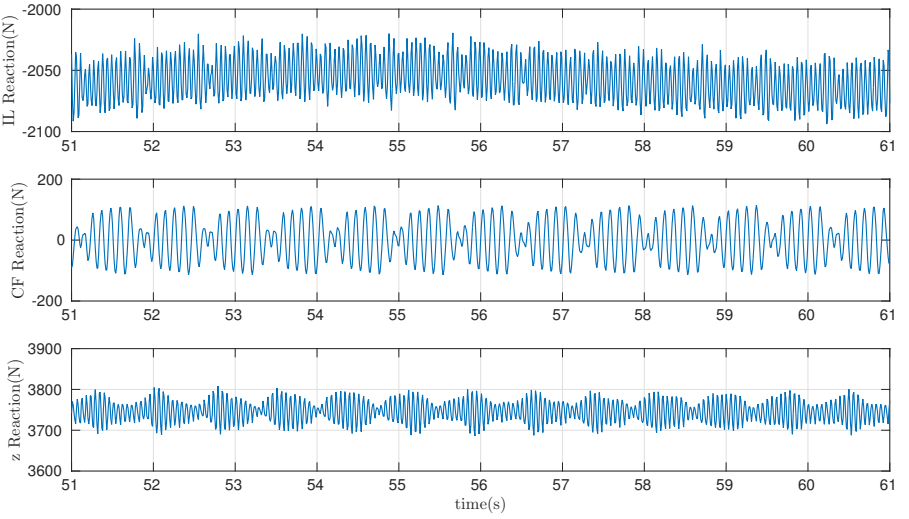

Figure 3.34: Reactions at the anchoring point

Name	Value
R_{IL}	1002.4 N
R_{CF}	0.0 N
R_z	3745.6 N

Table 3.8: Reactions at the anchoring point with Morison equation

3.3.8 Interpolation of different flows velocity

In order to use the proposed ROM also to study different environmental conditions the first step is to extend it in order to also account for unsteady and sheared velocity. So far, only constant and steady currents are analysed. Here it is explained how the procedure should be performed but no results are presented. Since the idea is to rewrite the model in order to account for different flow velocities, each parameter and each identified matrix of the model, for both the IL and CF directions, become a function of the flow velocity. It means that the model proposed in equations 3.29 and 3.30 must be rewritten as:

$$\dot{\boldsymbol{x}}(t) = \boldsymbol{A}(U)\boldsymbol{x}(t) + \boldsymbol{B}(U)f(L_c(t)) + \boldsymbol{K}(U)\boldsymbol{e}(t) \tag{3.33}$$
$$\boldsymbol{D_c}(t) = \boldsymbol{C}(U)\boldsymbol{x}(t) + \boldsymbol{D}(U)f(L_c(t)) + \boldsymbol{e}(t)$$

$$\begin{pmatrix} \dot{x}_{1,CF} \\ \dot{x}_{2,CF} \end{pmatrix} = \begin{pmatrix} x_{2,CF} \\ \mu_{CF}(U)(A_{CF}(U) - x_{1,CF}^2)x_{2,CF} - \omega_{0,CF}^2(U)x_{1,CF} + B_{CF}(U)u_{CF} \end{pmatrix} \tag{3.34}$$

$$L_c = x_{1,CF}$$

in which U is the flow velocity. The identification procedure of Chapter 3 should be then repeated for different values of the flow velocity, covering the whole range of expected flow velocity values. In this case it is not possible to define an affine or analytical dependency of the flow velocity with respect to the parameters and matrices of the model. For that reason the identification must be performed on a discrete number k of flow velocities. For flow velocity values that differ from the ones used for identification, an interpolation procedure must be used. The parameters of the different ROMs can then be interpolated in order to obtain the model parameters inside the whole range of velocities. For each time step and for each position along the cable the instantaneous flow velocity has to be selected, and through interpolation, the relative model can be derived.

The parameters of the van der Pol equation can be interpolated using a simple linear interpolation taking into account also the correlation between the different paramaters. The interpolation of the system matrices along the IL direction is more trivial because system matrices do not belong to a vector space but belong to a Lie group. The system matrices can be interpolated using the procedure explained in [93, 39].

Operating in such a manner one can analyse also unsteady and sheared current profiles.

3.3.9 Effect of waves and vessel motion on the proposed model

In order to account also for the motion of the vessel and for waves the procedure proposed by Lyions and Patel [79] can be used. In their theory the flow velocity used for the evaluation of the VIV forces is the relative velocity between the cable and the flow velocity. The velocity used for the analysis can be by derived summing the different components depicted in Figure 3.35.

$$U(t) = U_{currents} + U_{waves} + U_{motion} \tag{3.35}$$

After a certain water depth the influence of the vessel motion and waves becomes less relevant. In fact, the increase of relative flow velocity, due to the vessel motion, decreases linearly with the water depth. The increase of relative flow velocity, due to ocean waves, decreases exponentially with the water depth. After a water depth equal approximately to $L/2$, where L is the wavelength, the increase of the flow velocity due to the waves and to the vessel motion can be neglected.

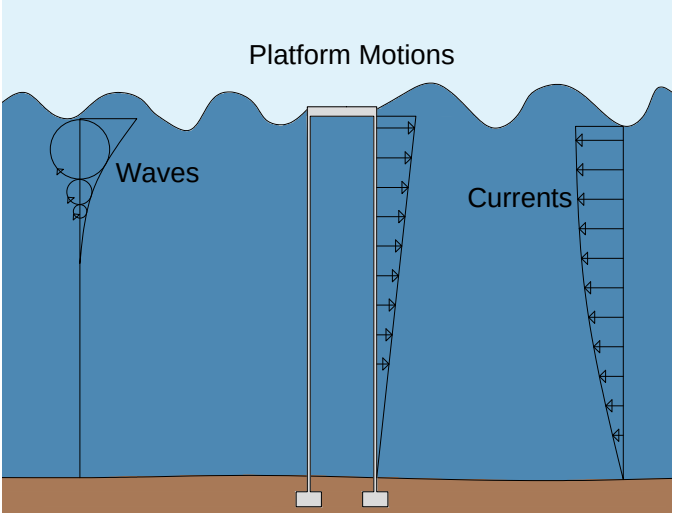

Figure 3.35: Different types of actions acting on moorings

Chapter 4

The stochastic parameter identification

The parameter identification along the CF direction is repeated in a probabilistic setting in order quantity the probability distribution functions. The applicability of the EnKF algorithm for the VDP parameter estimation is studied and discussed

Contents

4.1 Probabilistic parameter identification

In this chapter the identification procedure is repeated in a probabilistic setting. In particular the focus is on hydrodynamic forces along the CF direction. These are evaluated, as already shown in Equation 3.30, using a forced van der Pol system which depends on four parameters μ_{CF}, A_{CF}, ω^2_{0CF}, and B_{CF}. These are here indicated, for sake of simplicity, as a vector of parameters $\boldsymbol{s}$. Using this notation, a generic dynamical system can be rewritten as:

$$\dot{\boldsymbol{x}}(t) + \boldsymbol{A}(\boldsymbol{s}, \boldsymbol{x}(t)) = f(\boldsymbol{s}, t) \tag{4.1}$$

in which $\boldsymbol{x}(t)$ is the state vector, $\boldsymbol{A}$ is an operator that describes the physics of the system, and f is the excitation loading related to external input. In order to identify the parameters of the model, the response of the system is 'compared' to some observations of the state $\overline{\boldsymbol{y}}(\boldsymbol{x}(t))$. Here, since the focus is on model reduction, the observed function represents the response of the high-fidelity model of Chapter 2. In deterministic parameter identification the problem consists in finding the set of parameters $\boldsymbol{s}$ that minimizes the difference between the simulated and measured system output. This approach leads to the set of parameters which gives the best fit between the measured system response and the simulated output but does not give any information about the probability distribution function (PDF) of the identified parameters.

In a probabilistic setting each parameter of the vector $\boldsymbol{s}$ is modelled as a random variable with a priori probability distribution. The a priori probability distribution is generally determined using the preliminary knowledge one has about the system. The observations give additional informations on the system behaviour and can be used to update the prior probability distribution into posterior via Bayes's rule [103]. The predicted measurements $\boldsymbol{y}(\boldsymbol{x}(\boldsymbol{s}))$ are computed using a certain number of assumed values of $\boldsymbol{s}$ and then compared with the observations $\overline{\boldsymbol{y}}(\boldsymbol{x}(t))$. An overview about the two approaches is given in Figure 4.1. As it shown on the right part of the figure, for the probabilistic setting, the starting point are the prior PDFs of the parameters. Once the PDFs are defined one needs to compute the forward problem, which consists in the simulation of the model using the prior distributions. The last step is the update of the prior distributions into posteriors distributions in a Bayesan manner. In order to perform the update the observations one has about the system response must be used.

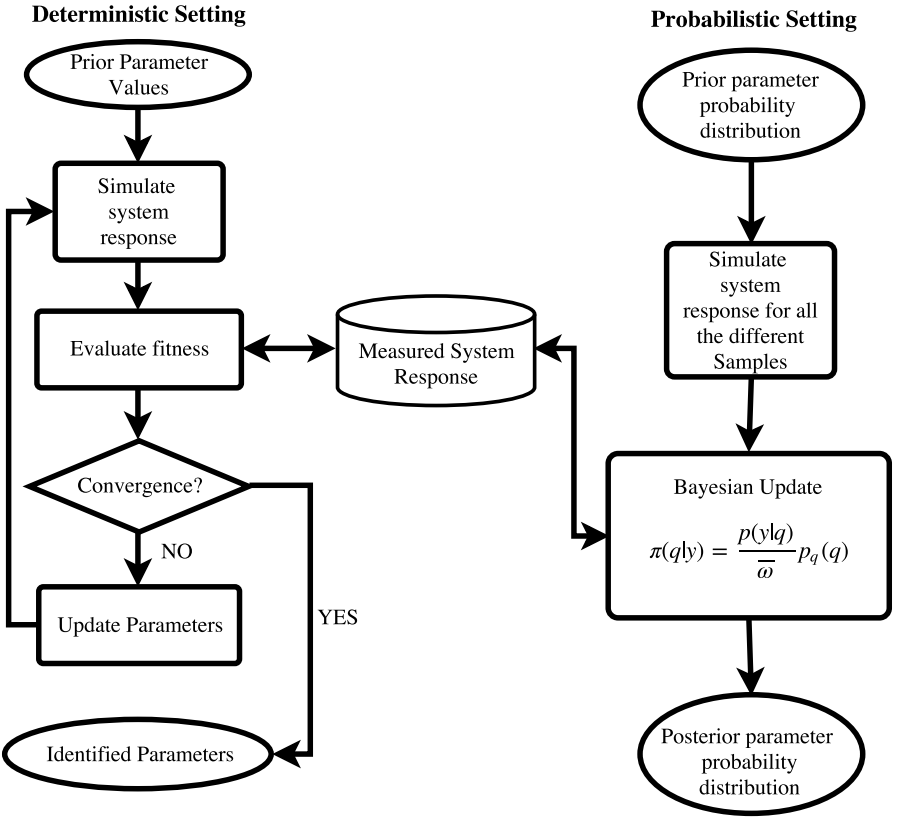

Figure 4.1: Comparison between the deterministic and probabilistic parameter identification approaches

4.1.1 The Bayesian Update

In Section 4.1 the basic idea behind stochastic parameter identification is given. Here the focus is on the Bayesan update which is a common way to update the uncertain probability distribution of a parameter using the additional knowledge, which in this context, comes from the high-fidelity model. According to [103] the Bayes theorem is expressed by:

$$\mathbb{P}(I_q|M_y) = \frac{\mathbb{P}(M_y|I_q)}{\mathbb{P}(M_y)}\mathbb{P}(I_q) \tag{4.2}$$

in which I_q a subset of possible values of $\boldsymbol{s}$, and M_y is the additional information provided by the observations. In the case of measures that all have a probability

density function it reads:

$$\pi(q|y) = \frac{p(y|q)}{\overline{\omega}} p_q(q) \tag{4.3}$$

in which p_q is the PDF of q, $p(y|q)$ is the likelihood function of y given q and $\overline{\omega}$ is a normalising factor for which the conditional density integrates to unity.

4.1.2 Ensemble Kalman Filter

The Ensemble Kalman filter (EnKF) is a tool which is normally used for state and parameter estimation. In order to present the parameter identification using the EnKF [33, 34] few recalls about the Kalman filter (KF) [68] and the extended Kalman filter (EKF) [46] are presented. The Kalman filter is an algorithm that produces the optimal estimate of the state of a linear system using the gain of prior knowledge obtained using a series of observed measurements. In general, the time evolution of a discrete system, in state-space notation, is described by the difference equation:

$$\boldsymbol{x}_{k+1} = f(\boldsymbol{x}_k, \boldsymbol{u}_k) + \boldsymbol{w}_k \tag{4.4}$$

where one observes the quantity:

$$\boldsymbol{y}_k = \boldsymbol{h}(\boldsymbol{x}_k) + \boldsymbol{v}_k \tag{4.5}$$

in which $\boldsymbol{x}_k, \boldsymbol{w}_k \in \mathbb{R}^n$ are respectively the state of the system and a stationary zero-mean white noise that reproduces the model error; $\boldsymbol{u}_k \in \mathbb{R}^m$ is the system input which influence the response; $\boldsymbol{y}_k, \boldsymbol{v_k} \in \mathbb{R}^p$ are respectively a function of the state and its associated zero-mean white noise that represents the measurement error. For a linear system the function f and h can be rewritten as:

$$f(\boldsymbol{x}_k, \boldsymbol{u}_k) = \boldsymbol{A}_k \boldsymbol{x}_k + \boldsymbol{B}_k \boldsymbol{u}_k \tag{4.6}$$

$$h(\boldsymbol{x}_k) = \boldsymbol{C}_k \boldsymbol{x}_k \tag{4.7}$$

The objective of the Kalman filter algorithm is to estimate the optimal state $\boldsymbol{x}_k^a$ which minimizes the trace of the quantity $\mathrm{E}[e_k^a (e_k^a)^T]$ in which e_a^k is the state error evaluated as $e_k^a = x_k - x_k^a$. The Kalman algorithm consists of two

steps: filtering and prediction, i.e.

Filtering

$$\boldsymbol{K}_k = \boldsymbol{P}_k^f \boldsymbol{C}_k^T (\boldsymbol{C}_k \boldsymbol{P}_k^f \boldsymbol{C}_k^T + \boldsymbol{V}_k)^{-1} \tag{4.8}$$

$$\boldsymbol{P}_k^a = (\boldsymbol{I} - \boldsymbol{K}_k \boldsymbol{C}_k) \boldsymbol{P}_k^f \tag{4.9}$$

$$\boldsymbol{x}_k^a = \boldsymbol{x}_k^f + \boldsymbol{K}_k (\boldsymbol{y}_k - \boldsymbol{C}_k \boldsymbol{x}_k^f) \tag{4.10}$$

Prediction

$$\boldsymbol{x}_{k+1}^f = \boldsymbol{A}_k \boldsymbol{x}_k^a + \boldsymbol{B}_k \boldsymbol{u}_k \tag{4.11}$$

$$\boldsymbol{P}_{k+1}^f = \boldsymbol{A}_k \boldsymbol{P}_k^a \boldsymbol{A}_k^T + \boldsymbol{W}_k \tag{4.12}$$

Here, $\boldsymbol{W}_k$ and $\boldsymbol{V}_k$ are respectively the covariance matrices associated with the state and measurement error noise $\boldsymbol{w}_k$ and $\boldsymbol{v}_k$. $\boldsymbol{P}_k^f = \mathbb{E}[e_k^f (e_k^f)^T]$ is the forecast error covariance with $e_k^f = x_k - x_k^f$, $\boldsymbol{P}_k^a = \mathbb{E}[e_k^a (e_k^a)^T]$ is the state error covariance. $\boldsymbol{K}_k$ is the so called Kalman gain that represents how much one needs to change the estimate after the gain of knowledge due to a given measurement.

In case of a non-linear system the extended Kalman filter can be used. In it matrices $\boldsymbol{A}_k$ and $\boldsymbol{C}_k$ are expressed by:

$$\boldsymbol{A}_k = \left. \frac{\partial f(\boldsymbol{x}, \boldsymbol{u})}{\partial \boldsymbol{x}} \right|_{\boldsymbol{x} = \boldsymbol{x}_k^a} \tag{4.13}$$

$$\boldsymbol{C}_k = \left. \frac{\partial h(\boldsymbol{x})}{\partial \boldsymbol{x}} \right|_{\boldsymbol{x} = \boldsymbol{x}_k^a} \tag{4.14}$$

The only difference from the standard Kalman filter is that in the prediction step a first order Taylor expansion of the f and h functions around the $\boldsymbol{x}_k^a$ position is used.

The EnKF is a suboptimal estimator that is a Monte Carlo approximation of the standard Kalman filter. The error statistics are obtained using a Monte Carlo procedure. The starting point is an ensemble of s forecasted values of the unknown state:

$$\boldsymbol{X}_k^f = [\boldsymbol{x}_k^{f1}, \ldots, \boldsymbol{x}_k^{fs}] \tag{4.15}$$

the true value is considered to be the mean of the ensemble $\overline{\boldsymbol{x}}_k^f$ and the error

matrix $\boldsymbol{E}_k^f$ and output error matrix $\boldsymbol{E}_{yk}^a$ are defined as:

$$\boldsymbol{E}_k^f = [\boldsymbol{x}_k^{f1} - \overline{\boldsymbol{x}}_k^f, \ldots, \boldsymbol{x}_k^{fs} - \overline{\boldsymbol{x}}_k^f] \tag{4.16}$$

$$\boldsymbol{E}_{yk}^a = [\boldsymbol{y}_k^{f1} - \overline{\boldsymbol{y}}_k^f, \ldots, \boldsymbol{y}_k^{fs} - \overline{\boldsymbol{y}}_k^f] \tag{4.17}$$

The variances needed to compute the Kalman gain $\boldsymbol{K}$ are then evaluated as:

$$\boldsymbol{P}_k^f \approx \frac{1}{s-1}\boldsymbol{E}_k^f(\boldsymbol{E}_k^f)^T \tag{4.18}$$

$$\boldsymbol{P}_{xyk}^f \approx \frac{1}{s-1}\boldsymbol{E}_k^f(\boldsymbol{E}_{yk}^f)^T \tag{4.19}$$

$$\boldsymbol{P}_{yyk}^f \approx \frac{1}{s-1}\boldsymbol{E}_{yk}^f(\boldsymbol{E}_{yk}^f)^T \tag{4.20}$$

and the Kalman gain is obtained as:

$$\boldsymbol{K}_k \approx \boldsymbol{P}_{xyk}^f(\boldsymbol{P}_{yyk}^f)^{-1} \tag{4.21}$$

in this context the EnKF is explained for state identification but, for parameter estimation, the procedure is exactly the same with the only difference that the parameters of the system are unknown. The update is performed on the prior probability distribution of the uncertain parameters. The first step is the selection of p samples based on the a priori probability distribution $\mathbf{P}^{pr}$ of the parameters which are randomly chosen. The parameters are here arranged in matrix form $\boldsymbol{Q}_{pr} = [\boldsymbol{q}_1^{pr}, \ldots, \boldsymbol{q}_p^{pr}]$, where each term $\boldsymbol{q}_k^{pr}$ is a vector containing the a priori parameters associated with the k sample. For each sample the output vector is constructed and all the obtained vectors are assembled in matrix form $\boldsymbol{Y}_{pr} = [\boldsymbol{y}_1^{pr}, \ldots, \boldsymbol{y}_p^{pr}]$. The posterior is constructed using the ensemble Kalman filter with the following expression:

$$\boldsymbol{Q}_{po} = \boldsymbol{Q}_{pr} + \boldsymbol{K}(\boldsymbol{Z} - \boldsymbol{Y}_{pr}) \tag{4.22}$$

in which $\boldsymbol{Z}$ is the matrix containing the available observations about the system that in this case are coming from the high-fidelity simulations.

4.1.3 Parameter identification using the ensemble Kalman Filter

In this subsection the parameter estimation already presented in Chapter 3 is repeated in a probabilistic setting using the EnKF algorithm. The applicability of the EnKF algorithm for the parameter identification of the VDP system is discussed and analysed. In the following example only three parameters are considered uncertain: μ_{CF}, A_{CF} and B_{CF}. The term ω_{0CF}^2 depends on the vortex shedding frequency. The lift coefficient, for the two analysed flow velocities, as depicted in Figures 3.24 and 3.28, presents a narrow-band spectrum. The vortex shedding frequency is then the frequency with the highest power spectral density. Here results are presented only for the flow velocity $V = 1.4\text{m/s}$ which corresponds to a vortex shedding frequency $f_v = 7.32\text{Hz}$. The term ω_{0CF}^2, according also to [35, 116], is then taken fixed and equal to $(2\pi f_v)^2 = 2116.8$. This value is also the same value identified using the deterministic identification procedure.

4.1.3.1 VDP parameter identification using the high-fidelity model response

In this subsection the parameter identification, as presented in Chapter 3, is repeated in a probabilistic setting using the EnKF algorithm explained in Section 4.1.2. The observations coincide with the results of the high-fidelity model. The prior distributions are constructed starting from the deterministic identification procedure. During the deterministic identification procedure, all parameters turned out to be positive, therefore log-normal distributions are used. To completely define a log-normal distribution one has to specify just the mean and the standard deviation. In particular, for each i^{th} parameter $\boldsymbol{s}(i)$ the mean is taken to be equal to 90% of the identified deterministic value and the standard deviation is fixed to be 10% of the mean value:

$$m(i) = s(i)_{det} \cdot 0.9 \tag{4.23}$$

$$\sigma^2(i) = m(i) \cdot 0.1 \tag{4.24}$$

The deterministic values are taken from Table 3.5. This choice is made in order to be sure that the deterministic value is contained inside the prior

PDF. According to the so defined PDFs, $\mathbf{N}$ independent samples are taken. In particular, the values of $\mathbf{N} = 100$ and $\mathbf{N} = 1000$ are considered.

The measurement error is considered to have a normal distribution with zero mean and variance σ_r^2 equal to 1% of the mean of the observations. The variance of measurement error, since the results are coming from numerical simulations, is much smaller. Taking higher value on the measurement error in case of nonlinear measurement/model operator may lead to better posterior estimate as observed in Rosic et al. [102]. For this particular case with values of σ_r^2 smaller then 0.01% of the corresponding mean lead to over or under estimation of the model parameter due to presence of nonlinearity in the model. Further consideration about the influence of the measurement error are reported in Subsection 4.1.3.2.

In Figures 4.2 and 4.3 the comparison between the prior probability distribution and the posterior probability distribution for the three considered parameters is reported. The continuous blue lines are used for the prior PDFs, the dashed red ones for the posterior PDFs. In the graphs the identified deterministic value of the parameters is also reported , indicated with a blue asterisk, and the values identified using the probabilistic procedure indicated with a red cross. In Table 4.2 the identified values and their comparison with the deterministic values in terms of relative error are reported. In both cases the results show

	μ_{CF}	A_{CF}	B_{CF}
Det. Value	68.29	1.1848	70.69
$\text{EnKF}_{\mathbf{N}=100}$	71.3	1.259	78.25
$\text{EnKF}_{\mathbf{N}=1000}$	63.29	1.187	91.02
$\varepsilon_{r,\mathbf{N}=100}$ (%)	4.40	6.33	10.69
$\varepsilon_{r,\mathbf{N}=1000}$ (%)	7.32	0.25	28.75

Table 4.1: Comparison between the true values and the identified values using the deterministic identification procedure

that the probabilistic procedure leads to identified values that are different from the deterministic ones. The maximum relative error with respect to the deterministic values is obtained for the parameter B_{CF} in case of 1000 samples. The identification of the parameters μ_{CF} and A_{CF} returns a relative error which is smaller respect to the parameter B_{CF}.

Increasing the number of samples, assuming that the deterministic value is exact, leads to better results only for the case of the parameter A_{CF}, for

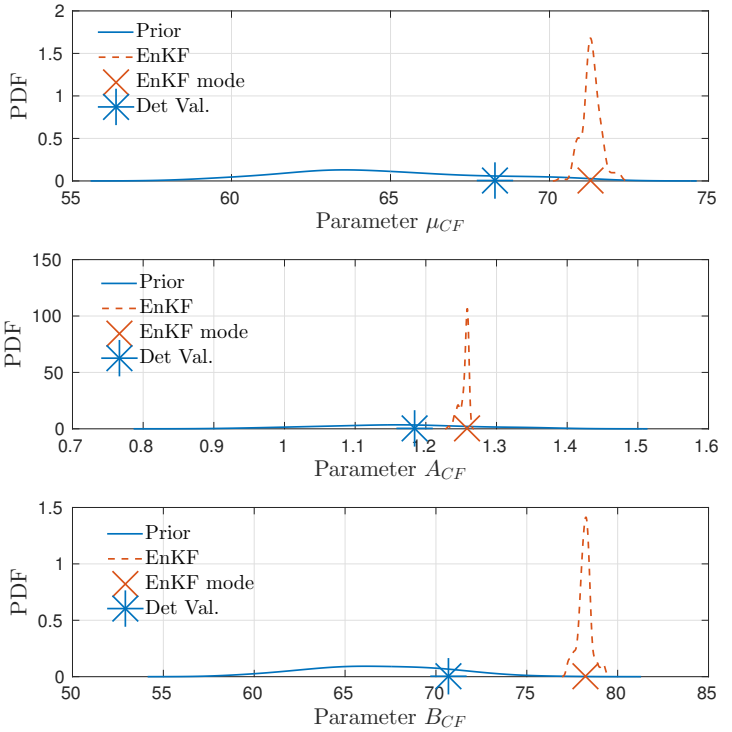

Figure 4.2: Comparison of prior and posterior PDF of the parameters - 100 Samples

other parameters the results get even further with respect to the deterministic value.

In order to see if it is possible to obtain closer values of the parameters to the deterministic values, the updating procedure is realised in a sequential way. In the standard updating procedure the forward problem is computed only once between the initial and the last time instant. After that the update is performed. In the sequential update the time history is divided in a certain number N_{int} of time intervals and the forward problem is computed N_{int} times. After the computation of each forward problem the updating procedure is performed and the posteriors become the prior for the next forward problem computation. The comparison of the two different updating procedures is reported in Figure 4.4. Results of this type of identification are reported in Figure 4.5. As shown in the results, this identification procedure, performed this time only with 100 samples, lead to identified values which are even further from the deterministic values with respect to the values identified using

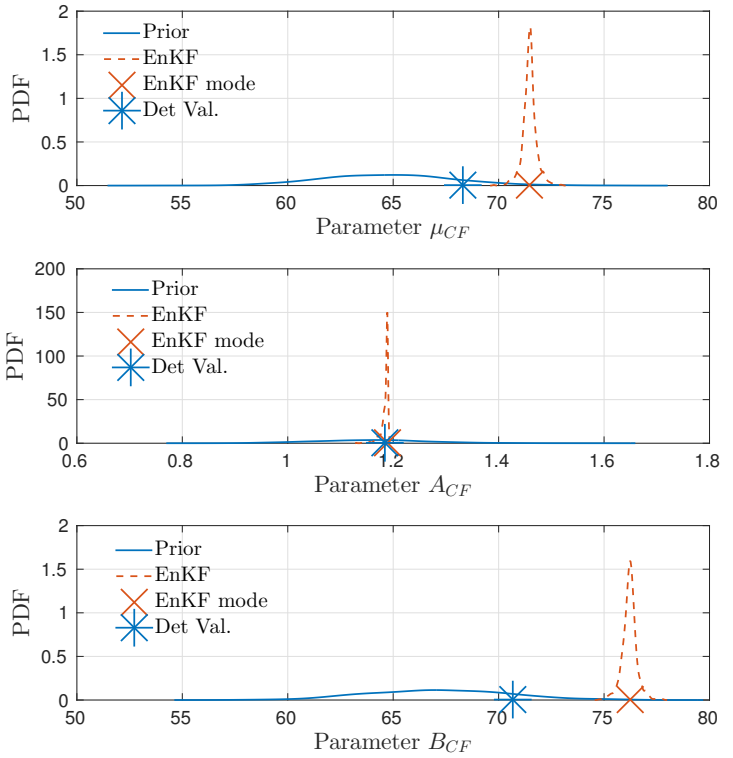

Figure 4.3: Comparison of prior and posterior PDF of the parameters - 1000 Samples

the standard updating. The sequential updating is not given better results because, after a certain number of updates, the prior PDF become completely different to the initial prior distribution. In other words, for each update step, the error produced in the updating procedure is summed with the errors produced in the previous update steps. This fact lead to unreasonable results, especially for the values which were correctly identified using the standard updating procedure. Looking at the results shown in Figures 4.2, 4.3, 4.5 and Table 4.2 it is possible to draw the following conclusions:

- The probabilistic identification with a standard updating procedure returns values of the parameters that are different from the deterministic ones.
- Changing the seeds and the number of sample one obtains different result, hence it is not a robust estimator.

- The sequential updating procedure does not increase the accuracy in the identification and lead to unreliable identified values.

So far it is unclear, especially for the standard updating procedure, what the source of the difference between the deterministic identification and the probabilistic identification is. The difference could be related to the modelling error or to the identification method which is not able to identify the right parameters. The usage of the van der Pol equation to model VIVs problem, as explained in Chapter 3, is a reasonable choice but does not completely capture the physics of the phenomena. For this reason, one has to consider that the parameter identification procedure may be affected by a non-negligible modelling error. In order to understand the origin of the discrepancy between the deterministic and the probabilistic identified values a different example has been performed. This example is described and discussed in Subsection 4.1.3.2.

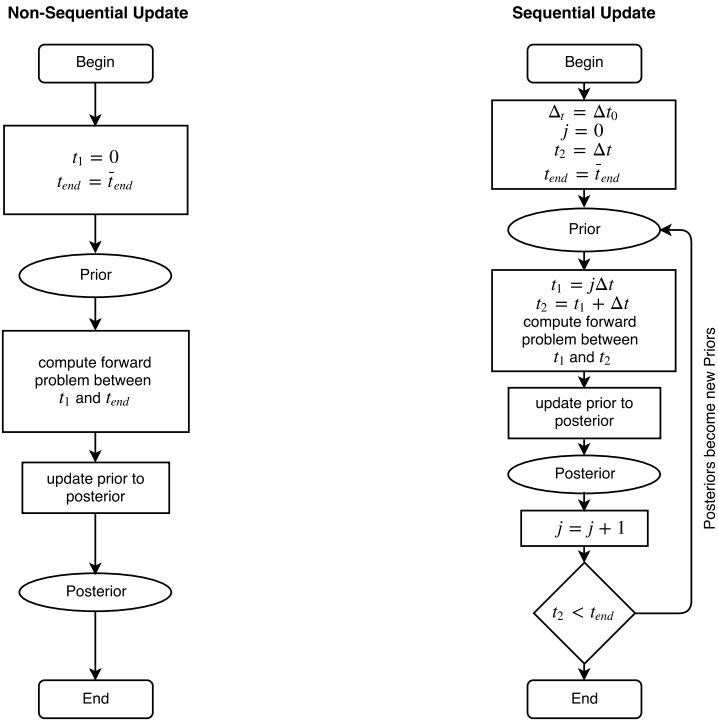

Figure 4.4: Comparison of between the standard update method and the sequential one

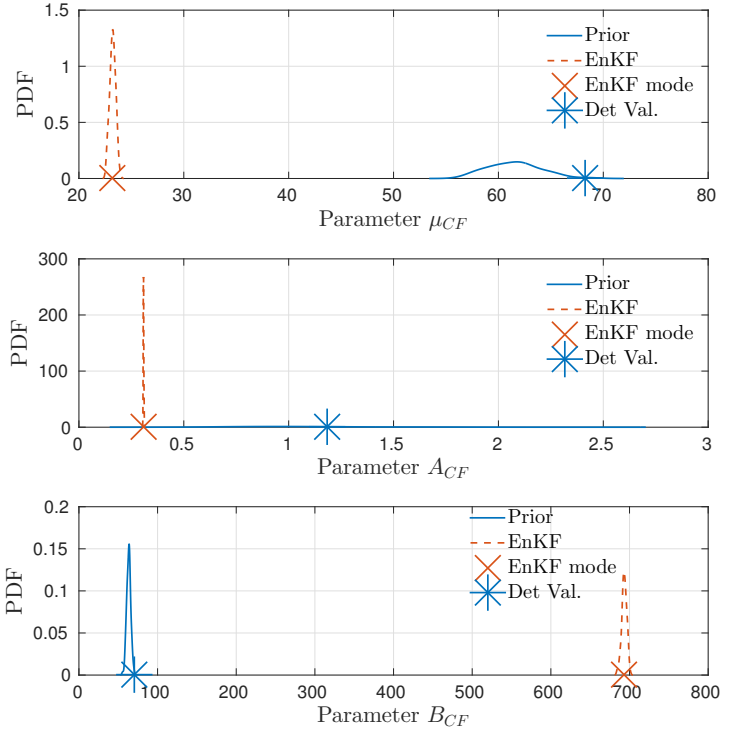

Figure 4.5: Comparison of prior and posterior PDF of the parameters - 100 Samples and sequential updating procedure

4.1.3.2 VDP probabilistic parameter identification using directly the response of the VDP model

In Subsection 4.1.3.1 it is explained that so far the origin of the discrepancy between the deterministic identified values and the probabilistic identified values is unclear. In particular, it is unclear whether the difference is caused by the modelling error or by the failure of one of the two identification methods. In order to clear this point it is performed a new example in which the model response, simulated under a certain set of known parameters, is used as observation. Operating in such a way, it is possible to eliminate the modelling of the error and to know what the true value of the parameters is. In order to create the measurements, the response of the model is simulated using the parameters taken from Table 3.5. The same excitation loading already used for the high-fidelity model is used. The identification procedure is then repeated in a deterministic and probabilistic setting and results are discussed and compared.

DETERMINISTIC IDENTIFICATION The deterministic identification procedure explained in Section 3.2 is here repeated using the response of the model directly as observations. In Table 4.2 the result of the deterministic

Name	True Val.	Ident. Val.	Start. Val.	Rel. Error %
μ_{CF}	69.2902	68.2898	19.53	$1.44E^{-}2$
A_{CF}	1.1839	1.1839	1.00	0
B_{CF}	70.6862	70.6858	135.00	$5.66E^{-}6$

Table 4.2: Comparison between the true values and the identified values using the deterministic identification procedure

identification are reported. The true values, the identified values, the starting values used for the identification and the relative errors are shown. The starting values are chosen equal to the starting values used in Section 3.2. The starting values are taken according to the suggestions by Srinil [116] and Facchinetti [35] who used a similar model for the modelling of cross flow forces. The procedure converges to the identified values after 14 iterations. The algorithm used for the parameter estimation is the same as that used in Section 3.2. It is possible to see from Table 4.2 that the identification procedure works well and leads to identified values that are close to true values. From the table it

is possible to conclude that the deterministic system identification works well to identify the parameters of the VDP system.

PROBABILISTIC IDENTIFICATION The same identification procedure is repeated in a probabilistic setting. The response of the model is used as measurements. In this way the modelling error is reduced to zero because the model being identified coincides with the model used to obtain the observations. The issues experienced before, with small values of the measurement error variance, are also found in this case: using a variance of the measurement error smaller than 0.01% of the measurement mean, the procedure becomes unstable or leads to unreliable results. The PDFs of the parameters are chosen making the same consideration made in 4.1.3.1. It is chosen not to use the starting value of the deterministic identification procedure, as mean of the PDFs, because for some parameters this value is far from the true value. The comparison between the prior PDFs and the posterior PDFs is reported for each parameter in Figure 4.6. In the figure only the case with $\mathbf{N} = 100$ and $\sigma_r^2 = 1\%$ is reported. In Table 4.3 the true values are reported, the identified values and the relative errors between the true and the identified values for different variances of the measurement error. As it is possible to see from Table 4.3 reducing the measurement error the accuracy of the results does not increase. For values of the measurement error variance smaller than 0.01% of the measurement mean the procedure is no longer converging. As it can be seen in Figure 4.6 and Table 4.3 the EnKF procedure, with a number of samples $\mathbf{N} = 100$, succeeds to identify the parameters in a quite accurate way especially concerning the μ_{CF} parameter for which the relative error is always below 1%.

CONCLUSIONS REGARDING THE TWO IDENTIFICATION TECHNIQUES: From the previous analysis it is possible to draw some conclusions. The difference between the deterministic and the probabilistic identification is due to two different factors: the modelling error and the identification procedure. The biggest error, as can be deduced from Subsection 4.1.3.1 is due to the modelling error. The VDP model, as already highlighted in the previous chapters, is a common system to model VIV problems but does not completely reproduce the physics of the problem. For this reason different identification procedures can lead to different identified parameters. The difference due to the identification method, highlighted in Subsection 4.1.3.2

	μ_{CF}	A_{CF}	B_{CF}
True Value	68.2902	1.1839	70.6862
$\text{EnKF}_{\mathbf{N}=100,\sigma_r^2=1\%}$	68.5281	1.1620	70.7981
$\text{EnKF}_{\mathbf{N}=100,\sigma_r^2=0.1\%}$	68.4143	1.1348	70.6272
$\text{EnKF}_{\mathbf{N}=100,\sigma_r^2=0.01\%}$	68.1142	1.1893	71.1634
$\text{EnKF}_{\mathbf{N}=100,\sigma_r^2=0.001\%}$	NC	NC	NC
$\varepsilon_{r,\mathbf{N}=100,\sigma_r^2=1\%}$ (%)	0.3484	1.8527	0.1582
$\varepsilon_{r,\mathbf{N}=100,\sigma_r^2=0.1\%}$ (%)	0.1817	4.1515	0.083
$\varepsilon_{r,\mathbf{N}=100,\sigma_r^2=0.01\%}$ (%)	0.2578	0.4518	0.6751
$\varepsilon_{r,\mathbf{N}=100,\sigma_r^2=0.001\%}$ (%)	NC	NC	NC

Table 4.3: Comparison between the true values and the identified values using the EnKF procedure

is much smaller and it is mainly due to the non-linearity of the VDP system. The model is in fact a non-linear model while the EnKF is an algorithm that is designed for state and parameter estimation of linear systems. In order to obtain a procedure that is convergent it is necessary to introduce an artificial measurement error which regularises the problem. This measurement error can be seen as the error one is doing considering a linear procedure instead of a non-linear one. It is possible to conclude that the EnKF procedure can identify the parameters of the VDP model in quite an accurate manner and can also provide the probability distribution of the identified parameters. On the other hand, it is affected by an error due to the fact that it is designed for linear systems while the VDP model is a non-linear system. For this reason it would be interesting to investigate the problem also with non-linear filters.

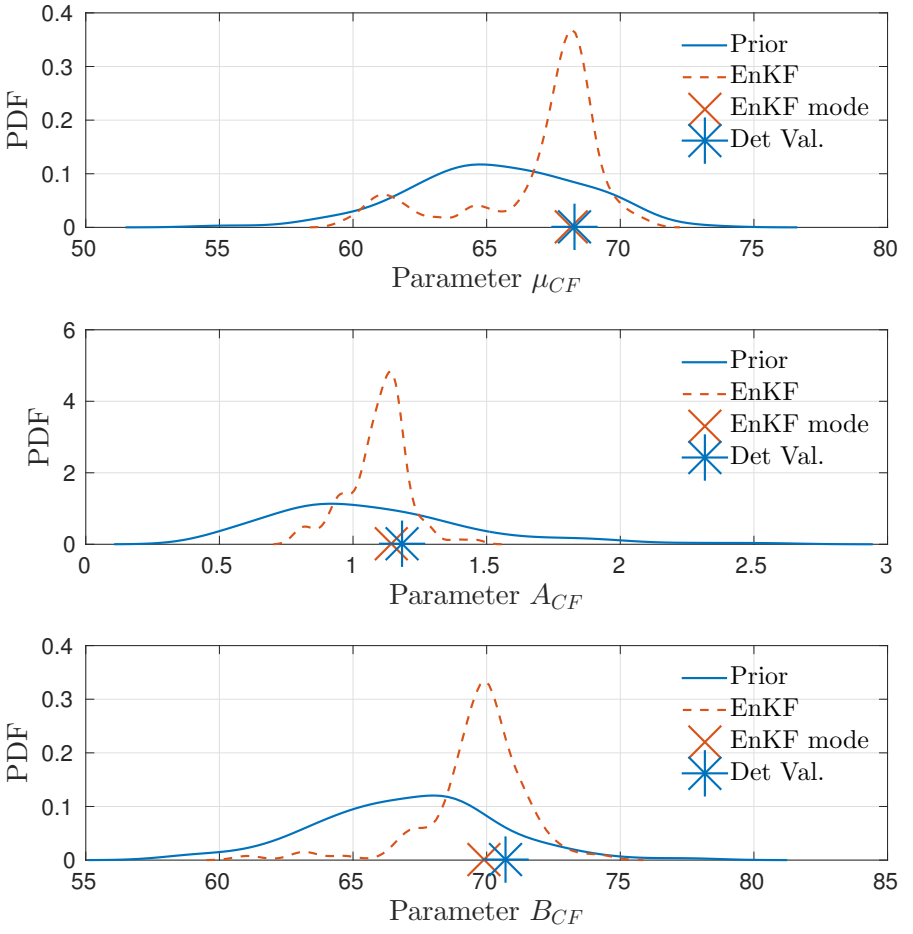

Figure 4.6: Comparison of prior and posterior PDF of the parameters with model response used as measurements - 100 Samples, $\sigma_r^2 = 1\%$

Chapter 5

A floating wind turbine application

In this chapter the proposed model is introduced in the general model of a floating wind turbine

Contents

5.1 The floating wind turbine example

Floating wind turbines are one of the most promising and most studied offshore applications for the exploitation of the huge amount of wind resources located in deepwater [132, 65]. In fact, after a certain depth, fixed-bottom structures become economically unfeasible [121]. According to the international design standard for off-shore wind turbines [58], to certify an offshore wind turbine an integrated loads and response analysis has to be performed. This kind of analysis is also important for the designer in order to optimize and verify the structural safety. Therefore, it is necessary to develop reliable tools that can model the dynamic response of floating wind turbine platforms in a comprehensive and fully integrated manner. When dealing with floating offshore wind turbines, numerous floating support configurations are possible. These can be divided into three general categories based on the physical principle used to achieve stability [15]. The first category, the ballast stabilized platform, uses ballast weights to achieve platform stability; in the second category, the mooring lines stabilized platform, stability is reached using mooring line tension; platforms that achieve stability through a distributed buoyancy can be placed into the third category named the buoyancy stabilized platform. Real platforms will be hybrid designs that gain static stability from all of these methods.

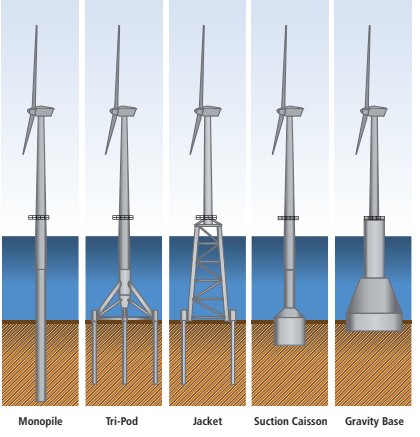

(a) Fixed-bottom wind turbine classification

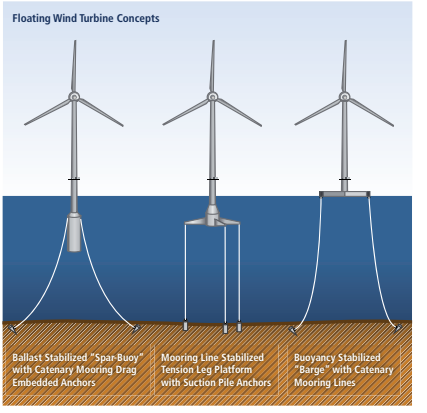

(b) Floating wind turbine classification

Figure 5.1: Offshore wind turbine classification - Image taken from [84]

Many models have been proposed for the fully coupled simulation of an offshore

wind turbine [65, 110, 29] but according to a recent report coordinated by Robertson [101] none of them consider the vortex-induced vibration phenomena for the mooring lines. The VIV model proposed in this thesis is quite general and can be added to any computational structural solver for offshore applications to model risers or mooring lines. Here it is presented how the coupling of the proposed model with a general simulation tool for offshore wind turbines could be realized. A general overview about the modelling aspects regarding a floating offshore wind turbine are given. Particular attention is given to the hydrodynamic part of the problem, which is the most important one in order to realize a coupling with the mooring lines model.

5.1.1 The coupled analysis

In this subsection a general overview about the coupled dynamic analysis of a floating wind turbine is given. The analysis of a floating wind turbine can be decomposed into four different subproblems that have to be properly coupled together:

- The Aerodynamic Problem
- The Hydrodynamic Problem
- The Structural Problem
- The Mooring Lines Problem

5.1.1.1 Aerodynamics

The aerodynamic problem can be solved in different ways; one of the most common approaches in literature is the blade element momentum (BEM) theory. This technique has been developed for helicopter aerodynamics and then applied to wind turbine modelling. It combines the blade element theory with the momentum theory and it permits the evaluation of the steady loads, the thrust and power for different wind speed settings. For further details regarding the mathematical approach of this method one can see several classical textbooks on wind turbines [43, 81].

This approach has been widely validated through experimental activities on full-size wind turbines. It is quite a simple method, easy and fast to be

implemented. Its disadvantages lie in the fact that it has to be intended only for steady flow and its accuracy has not already been checked with elevated pitch angles.

Alternatives to this method are the free wave lifting method [4, 51], and the CFD method [45, 109]. The former can also model nonlinear contributions but has the disadvantage of being slower than the BEM method. The latter can model the aerodynamics of the rotor in very realistic way but needs huge computational resources. For this reason it is not still applicable for design analysis where several different wind turbine configurations must be analysed.
.

5.1.1.2 Structural Dynamics

Several different approaches can be used to analyse the structural dynamics of floating offshore wind turbines. The most common method is the modal representation. With this approach, the fundamental mode shapes and frequencies are firstly evaluated and then coupled together inside the equation of motion. This approach is computationally efficient because it can describe the motion of the whole structure with only few degrees of freedom. However, with the modal representation, since results from different mode shapes are added together, it is only possible to analyse linear structures with small deflections.

Another widely used method is the multibody system approach. With this method the structure is divided into a number of flexible or rigid elements connected together by joint. The elements can either be rigid or flexible and their kinematics is described by equations of motion that can be easily derived from Newton's equation. Compared to modal representation, having normally more degrees of freedom, it is computationally less efficient but can describe the dynamics of the system in a more accurate manner. Each body can undergo large translational and rotational motions. For this reason, the assumption of linearity is no longer needed.

The Finite Element Method is a really powerful technique that has been developed for structural mechanical analysis. In this method, the structure is discretised into a finite number of elements interconnected in some points called nodes. The elements used can be beams, two dimensional plates and three-dimensional solids. FEM methods can describe the dynamic behaviour

of the structure in a highly accurate manner including large deformations and material non-linearities. However, a high level of detail is correlated with a big computational effort. Most of the available codes use a combination of the three methods reported here.

5.1.1.3 Mooring Lines

The problem regarding the mooring lines as already mentioned in Chapter 1 is a non-linear problem and normally needs a dedicated design tool. To model the effect of mooring lines, on codes for floating offshore wind turbines, some approximated methods are normally used. A possible method is the quasi-static representation, in which the non-linear mooring restoring force is represented with a quasi-static approach. With this approach the static equation of equilibrium is solved at each instant for a given platform displacement. It means that the drag force acting on the cable and inertia forces are not considered. Another possible approach is a force-displacement representation in which the forces acting on the platform are modelled through non-linear springs for each degree of freedom. None of these approaches account for the cable dynamics. The only way to account for the cable dynamics is to use a fully dynamic model. The equation of motion of the cables is quite complex and an analytical solution cannot be found. An alternative is to solve the equation of motion with numerical methods that discretise the cable in number of masses linked together by joints either with a multibody or a FEM approach.

5.1.1.4 Hydrodynamics

The hydrodynamics of an offshore platform is normally studied neglecting the hydro-elasticity of the structure. The platform is modelled as a rigid body with six DOFs. In most applications, ocean waves are modelled making the assumption of an ideal flow which means that there are no shear stresses due to viscosity and that the flow is irrotational [36]. This assumption implies that the flow velocity can be expressed as the gradient of a scalar function Φ satisfying the Laplace's equation:

$$\nabla^2 \Phi = 0 \tag{5.1}$$

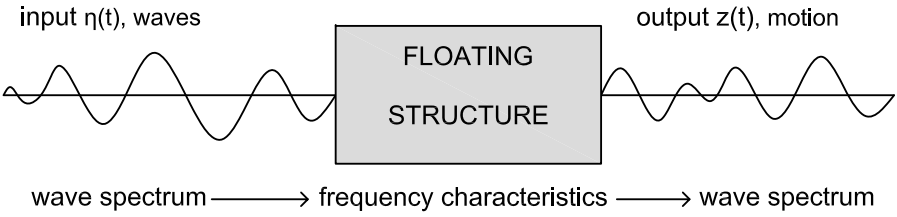

Figure 5.2: Relation between Motions and Waves

in which $\Phi(x,t)$ is the velocity potential. Equation 5.1, together with its kinematic and dynamic boundary condition at the free surface, at the platform-water interface, and at the bottom, can be solved in order to get the flow velocity field. For simple cases an analytical solution can be found while for more complex cases a numerical solution is needed. The model described above is the potential flow model. It consists of the Laplace's equation plus the free-surface and bottom boundary conditions. The wave-structure interaction can then be solved using two different approaches, the frequency domain approach and the time domain approach.

FREQUENCY-DOMAIN ANALYSIS METHODS:In oil and gas industries frequency domain methods are commonly used for the design and the analysis of floating offshore structures. Frequency domain methods are valid only for system with a linear behaviour. This means that, at each frequency, the different ratio between the motions and the waves is constant. The resulting motion can be obtained by adding together results from singular wave amplitudes. Operating in such a manner, when the wave spectrum and the frequency characteristics are known, it is easy to evaluate the response spectra and its statistic. The frequency domain approach is reported here only briefly - for further details one see the many textbooks and lecture notes on Hydrodynamics [66, 88].

As already stated, if the system is linear it is possible to obtain the resulting motion by adding the results from different wave frequencies. The linearity makes it possible to see the resulting motion as a superposition of the body oscillating in still water, without external forces, and the restrained body under wave forces. The equation of motion can be described by the following expression:

$$\frac{d}{dt}(\rho\nabla\cdot\dot{z}) = \rho\nabla\cdot\ddot{z} = F_h + F_w \tag{5.2}$$

in which ρ is the water density, ∇ is the volume of displacement of the body,

F_h is the hydro-mechanical force in the z-direction and F_w is the exciting force in the z-direction.

The forces acting on the body can be divided, into two contributions [36], one due to the motion of the body in still water and one due to the action of waves on the restrained body:

- **Hydro-mechanical forces and moments** result from the oscillation of the rigid body in still water. They can be subdivided into a **Radiation Term** and a **Hydrostatic Loading Term** that describes the loads on the structure arising from the static pressure around it.
- **Wave exciting forces and moments (Diffraction Term)** result from the ocean waves acting on the restrained body.

In the following paragraphs an example of how it is possible to evaluate these two contributions on a simple structure is presented. The case of a floating cylinder is presented.

HYDROMECHANICAL FORCES: The hydro-mechanical loads are carried out with a free decay test. The equation of motion of a free decay for the simple case of a vertical cylinder oscillating in water test is presented here. The equation of motion of the free decay test can be written as:

$$m\ddot{z} = -P + \rho g(T - z)A_w - b\dot{z} - a\ddot{z} \tag{5.3}$$

where z is the vertical displacement, $P = mg$ is the mass force, $m = \rho A_w T$ is the solid mass of the cylinder, a is the hydrodynamic mass coefficient, b is the hydrodynamic damping coefficient, $c = \rho g A_w$ is restoring spring coefficient, $A_w = \frac{\pi}{4}D^2$ is the diameter of the cylinder and T is the draft at the cylinder at rest. The equation above, using Archimedes' law becomes:

$$(m + a)\ddot{z} + b\dot{z} + cz = 0 \tag{5.4}$$

WAVE FORCES: Wave loads, as already mentioned, are computed considering the ocean waves acting on the restrained body. The classical potential theory of deep water waves gives:

$$\Phi = \frac{-\eta_a g}{\omega} e^{kz} sin(\omega t - kx) \tag{5.5}$$

$$\eta = \eta_a cos(\omega t - kx) \tag{5.6}$$

Eq.s 5.5 and 5.6 represent the wave potential and the wave elevation respectively according to the potential theory for deep water waves. Considering always the same cylinder, used to derive the equation of motion for the free decay test, it is possible to derive the pressure p on the bottom (for $z = -T$) of the cylinder using the linearised Bernoulli equation:

$$\begin{aligned} p =& -\rho\frac{\delta\Phi}{\delta t} - \rho g z \\ =& \rho g \eta_a e^{kz} cos(\omega t - kx) - \rho g z \\ =& \rho g \eta_a e^{-kT} cos(\omega t - kx) - \rho g T \end{aligned} \tag{5.7}$$

If the diameter of the cylinder is much smaller than the wave length the assumption of a uniform pressure acting on the bottom can be made. So the pressure and the total force become:

$$p = \rho g \eta_a e^{-kT} cos(\omega t) - \rho g T \tag{5.8}$$

$$F = [\rho g \eta_a e^{-kT} + \rho g T] \cdot \frac{\pi}{4} D^2 \tag{5.9}$$

The harmonic part of this expression can be rewritten as a spring coefficient c times a reduced or effective wave elevation η^*. This part of the force is known as the Froude-Krilov force. Part of the waves are diffracted and so correction terms need to be introduced. The correction terms are proportional to the vertical acceleration and to the vertical velocity of the water particles. The total force can be divided into three different parts as follow:

$$F_w = a\ddot{\eta}^* + b\dot{\eta}^* + c\eta^* \tag{5.10}$$

in which the terms $a\ddot{\eta}^*$ and $b\dot{\eta}^*$ are corrections to the Froude-Krilov term.

EQUATION OF MOTION: Once the mechanical and the wave forces are defined it is possible to write the general equation by combining Equation 5.4 and Equation 5.10:

$$(m + a)\ddot{z} + b\dot{z} + cz = a\ddot{\eta}^* + b\dot{\eta}^* + c\eta^* \tag{5.11}$$

Solving the above equation the result in heave amplitude is obtained:

$$\frac{z_a}{\eta_a} = e^{-kT}\sqrt{\frac{(c - a\omega^2)^2 + (b\omega)^2}{c - (m + a)\omega^2)^2 + (b\omega)^2}} \tag{5.12}$$

The response amplitude characteristics $\frac{z_a}{\eta_a}(\omega)$ are often called **Response Amplitude Operators(RAO)**.The response in irregular waves can be deduced, using the linearity of the problem, starting from the response in regular waves. Adding the results for different wave amplitudes the heave response spectrum is deduced:

$$S_z(\omega) = \left|\frac{z_a}{\eta_a}(\omega)\right| \cdot S_\eta(\omega) \tag{5.13}$$

TIME DOMAIN ANALYSIS: The frequency domain analysis takes advantage of the linearity of the problem. Many common cases, in which non-linearities become important, cannot be treated with such an approach. If the system is non-linear, the superposition principle, which permits the frequency domain approach, is no longer valid. In these cases, the only way to obtain the system response is to directly resolve Newton's second law. An initial approach to solve this problem, briefly reported here, can be found in the classical formulation proposed by Cummins [30].

The Cummins approach uses the Impulse Response Function. For any stable linear system, considering $R(t)$ the response to an unit impulse, the response to an arbitrary force $f(t)$ is given by:

$$x(t) = \int_{-\infty}^{t} R(t-\tau) f(\tau) d\tau \tag{5.14}$$

Let us define $x_i, (i = 1, ..., 6)$ as the displacements for the six degrees of freedom of the body:

x_1 = surge (positive forward)

x_2 = sway (positive to port)

x_3 = heave (positive upward)

x_4 = roll (positive, deck to starboard)

x_5 = pitch (positive, bow downward)

x_6 = yaw (positive, bow to port)

Considering $f_i(t)$ arbitrary forces and $R_{ij}(t)$ the response in mode j to an impulse at $t = t_0$ in mode i on obtain the corresponding responses as:

$$x_j(t) = \sum_{i=1}^{6} \int_0^{\infty} R_{ij}(\tau) f_i(t-\tau) d\tau \tag{5.15}$$

The response is completely defined once the matrix $R_{ij}(t)$ is defined. The complete equation of motion can be rewritten as:

$$(M + A) \cdot \ddot{x}(t) + \int_{-\infty}^{t} B(t-\tau) \cdot \dot{x}(t) \cdot d\tau + C \cdot x(t) = X(t) \tag{5.16}$$

in which $\ddot{x}(t)$ is the translational or rotational acceleration at time t, $\dot{x}(t)$ is the translational or rotational velocity at time t, $x(t)$ is the translational or rotational displacement at time t, M is the solid mass or mass moment of inertia, A is hydrodynamic or added mass coefficient, $B(t)$ is the matrix of retardation [90], C is the spring which depends on the body geometry, $X(t)$ are the external load at time t where t and τ represent time.

The spring coefficient C can easily be determined starting from the underwater geometry on the other hand, in order to determine the A and B coefficients it is necessary to determine the velocity potentials and a direct approach would be quite complex. An easy way to determine A and B is discussed by Ogilvie [90].

5.1.2 Fully Coupled Equation of motion

Now that the equations of motion for a floating platform have been introduced, the more specific equations of motion for a floating offshore wind turbine can be written. If all the forces acting on the rotor and on the tower are considered as additional external forces, the dynamic equation, starting from equation 5.16, can be written for each DOF i as:

$$(M_{ij} + A_{ij})\ddot{x}_i + F_i^{Hydro} + F_i^{Lines} + F_i^{Upper} = 0 \tag{5.17}$$

in which M_{ij} and A_{ij} are the inertia mass matrix and added mass matrix components respectively, F_i^{Hydro}, F_i^{Lines} and F_i^{Upper} are respectively the total hydrodynamic force, the force due to the mooring lines and the force coming

from the upper part of the structure for the i DOF, x_i is the displacement or rotation associated with the i DOF. As already seen the total hydrodynamic force can be written as:

$$F_i^{Hydro} = F_i^{Waves} + \rho g V_0 \delta_{i3} - C_{ij} x_j - \int_0^t B_{ij}(t-\tau)\dot{x}_j(\tau)\,\mathrm{d}\tau \tag{5.18}$$

in which F_i^{Waves} is the wave force that can be evaluated using eq. 5.10, the second term is the weight of the structure, the third term represents the restoring force and C_{ij} are spring coefficients, the last term is the contribution to the wave radiation damping and B_{ij} are the components of the retardation matrix.

Now each term is defined and the fully coupled equation in short form can be rewritten as:

$$f(\ddot{\boldsymbol{x}}, \dot{\boldsymbol{x}}, \boldsymbol{x}, \boldsymbol{p_1}, t) = -\boldsymbol{F}^{Lines}(\ddot{\boldsymbol{x}}, \dot{\boldsymbol{x}}, \boldsymbol{x}, \boldsymbol{p_2}, t) \tag{5.19}$$

in which f is a function which contains all the terms of equation 5.17 except from the mooring lines term $\boldsymbol{F}^{Lines}$. Forces coming from the mooring lines can be evaluated using the model developed in subsection 3.3.4. A suitable coupling between the function f, which describes the motion of the platform, and the reduced order model must be developed.

5.1.2.1 Coupling of the ROM with the platform motion equation

The coupled system is described by equation 5.19. In many existing tools for the modelling of floating offshore wind turbines, mooring lines are solved using a separate module. For this reason, here the same approach is used.

Each mooring line is structurally modelled using a standard finite element discretisation while hydrodynamic forces acting on the mooring are evaluated using the developed ROM. The idea, as already mentioned, is to keep the platform module and the mooring lines module separated. For this reason, the coupling has to be realized using a partitioned approach. The input information of the whole analysis are the flow velocity profile, the aerodynamic forces acting on the tower and on the rotor that in this context are considered just as an external applied force, and the mechanical characteristics of the moorings and of the platform.

Using such an approach, the influence of the mooring lines on the platform is considered as an external restoring force while the influence of the platform on the mooring system is considered as an imposed motion on the top of each mooring line. A sketch which illustrates how the problem has previously been decoupled and then re-coupled is shown in figure 5.3-b. An example of a coupling algorithm that could be used for the purpose is represented in algorithm 2. This algorithm is similar to the one used for the fluid-structure interaction coupling. At each time step of the coupled simulation an iterative problem must be solved. The first step is the prediction of the restoring forces based on the last converged values of them at the previous time steps. The choice of the predictor is not unique and several different orders and expression could be used. An example of the predictor could be:

$$\hat{\boldsymbol{F}}^{(p)}_{\boldsymbol{i,N+1}} = \boldsymbol{F_{i,N}} + \alpha_0 \Delta t \dot{\boldsymbol{F}}_{\boldsymbol{i,N}} + \alpha_1 \Delta t (\dot{\boldsymbol{F}}_{\boldsymbol{i,N}} - \dot{\boldsymbol{F}}_{\boldsymbol{i,N-1}}) \tag{5.20}$$

Depending on the values of α_0 and α_1 it is possible to change the order of the predictor. Once the predicted value of the restoring force is determined it is possible to the platform equation in order to get the displacements, velocities and accelerations at the anchoring points. Once the displacement is known the mooring lines problem is solved and a new restoring force is determined. In general the restoring force obtained during the mooring line computation is different from the predicted one. For this reason an iteration procedure must be performed. The iteration process continues until the difference between the forces evaluated at two sequential iterations is smaller than a certain tolerance.

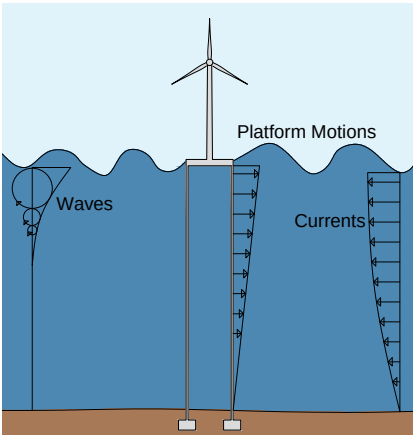

(a) Actions acting on the mooring lines

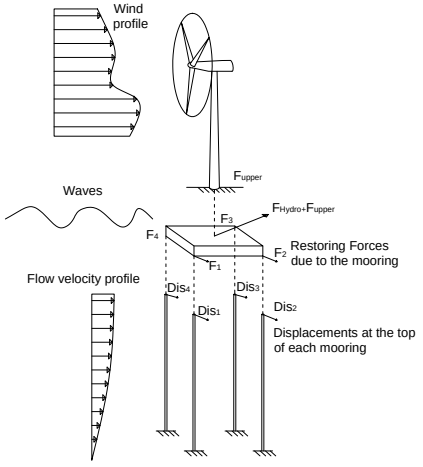

(b) Different components of the floating turbine

Figure 5.3: Coupling procedure scheme between the whole subparts

Algorithm 2 Coupling algorithm between platform and mooring modules

Given: initial time T_0, length of the simulation T, time step size of the simulation Δt, the tolerance TOL, Flow Velocity Profile $U(t)$, Forces coming from the upper part $F_{upper}(t)$

while $t < T$ **do**
  $k = 0$
  while $\boldsymbol{res}_{N+1}^{(k)} < TOL$ **do**
    if $k = 0$ **then**
      for $i = 1 : N_l$ **do**
        Predict restoring force: $\hat{\boldsymbol{F}}_{i,N+1}^{(0)} = P(\boldsymbol{F}_{i,N}^{(k_{max})}, \boldsymbol{F}_{i,N-1}^{(k_{max})}, \dots)$
      end for
    end if
    given $\hat{\boldsymbol{F}}_{1:N_l,N+1}^{(k)}$ solve the platform equation $\rightarrow \boldsymbol{Dis}_{1:N_l,N+1}^{(k)}$
    for $i = 1 : N_l$ **do**
      given $\boldsymbol{Dis}_{1:N_l,N+1}^{(k)}$ solve the mooring problem $\rightarrow \boldsymbol{F}_{1:N_l,N+1}^{(k)}$
    end for
    Evaluate residual $\boldsymbol{res}_{N+1}^{(k)} = \hat{\boldsymbol{F}}_{1:N_l,N+1}^{(k)} - \boldsymbol{F}_{1:N_l,N+1}^{(k)}$
    Update restoring forces $\hat{\boldsymbol{F}}_{f,N+1}^{(k+1)} = \boldsymbol{F}_{1:N_l,N+1}^{(k)}$
    $k = k + 1$;
  end while
  $N = N + 1, t = t + \Delta t$
end while

Chapter 6

Conclusions and Outlooks

In this chapter some conclusions about the PhD thesis are drawn. The main goals achieved in this thesis are summarised and suggestions for future developments of the work conducted in this thesis are given

Contents

6.1 Conclusions

This thesis aimed to present a novel reduced order model for the analysis of long flexible cylinders in an offshore environment with a focus on vortex induced vibrations. The main goals achieved during the development of this thesis can be summarised in the following way:

- A reduced order model for the analysis of vortex induced vibrations phenomena in both the in-line and cross-flow directions has been developed. Several different models were tested and discussed. In particular, models based on a forced van der Pol oscillator and on a linear state-space model are analysed. The final proposed model consists of a forced van der Pol oscillator along the cross-flow direction, and of a linear state space model along the in-line direction. The van der Pol system is forced by using a function of the instantaneous acceleration of the cylinder along the cross-flow direction while the linear state-space system is forced using a function of the square of the lift coefficient. To the author's knowledge, it is the first time that such a model has been used to model vortex induced vibrations phenomena. This reduced order model turned out to be the best alternative among the analysed models and has the capacity of exploiting the advantages of both the van der Pol equation and of linear state-space models. The van der Pol system has in fact the self-limitation and self-excitation features which are peculiar characteristics of the vortex induced vibrations phenomena. On the other hand, state-space models can model systems with arbitrary dimensions and with more than one dominant frequency. Operating in such a manner the resulting model is self-limited and self-excited for both the in-line and the cross-flow direction. Moreover, in this way, the two directions are coupled.

- A fluid-structure interaction solver has been developed by coupling a finite element method solver with a computational fluid dynamic solver with a large eddy simulation turbulence model. This solver has been tested and validated showing good matching with previous numerical results and experimental activities. The results of the fluid-structure interaction analyses, in terms of drag and lift coefficient, conducted on a small scale flexible cylinder, undergoing forced oscillations, are used to identify the parameters and the structure of the reduced order model.

- The identified reduced order model has been validated by using experimental activities conducted in a wave tank showing promising results. The model has the capacity of capturing the amplitude and frequency of oscillation for both the considered flow velocities. The trajectory of the cylinder has also been captured showing that the coupling between the in-line and cross-flow directions is well represented.
- Concerning the van der Pol model, the identification procedure of the model parameters, using the results of the fluid-structure interaction solver, has been conducted both in a deterministic and probabilistic setting. For the deterministic setting a non-linear optimization procedure based on a Trust-Newton region algorithm is used while for the probabilistic setting the ensemble Kalman filter algorithm is used. The probabilistic procedure returned similar values of the parameters as the deterministic procedure, but turned out to be less robust. The identified values depend on the seeds and on the number of samples used for the identification.
- A coupling strategy between the proposed reduced order model and a general solver to study the dynamic of an offshore platform is presented and discussed. The case of a floating offshore wind turbine is particularly studied.

6.2 Outlook

During the writing and the development of this thesis several problems and questions came out. Some of these would need further investigation:

- The proposed model was demonstrated to work well for the two analysed flow velocities, but it would be interesting to test the model for a wider range of velocities and to study the possibility of an interpolation algorithm between the different flow velocities as discussed in Subsection 3.3.8.
- A factor that is not treated in the thesis and would be interesting to study is the inclination between the flow and the cylinder. Only flows that are perpendicular to the axis of the cylinder have been studied and it would be interesting to study the influence of the flow inclination.

- The influence of vortex-induced vibrations phenomena on riser is widely discussed in literature but a comprehensive study on mooring lines and on the influence of these phenomena on the overall response of the platform, especially for floating offshore wind turbines, is still lacking. For this reason, as discussed in Chapter 5 it would be interesting to realize an efficient coupling between the reduced order model presented in this thesis and a dynamic solver for offshore platforms. This part of the work is currently under development.
- Regarding the identification procedure, the applicability of the ensemble Kalman filter procedure for the identification of the van der Pol model parameters has been studied showing some important limitations. For this reason, it would be interesting to repeat the identification procedure with non-linear filters.

List of Figures

List of Tables

Bibliography

[1] Akhtar, I. *Parallel Simulation, Reduced-Order Modeling, and Feedback Control of Vortex Shedding using Fluidic Actuators*. PhD thesis, Virginia Polytechnic Institute and State University, 2008.

[2] Akhtar, I., Marzouk, O. A., and Nayfeh, A. H. A van der Pol-Duffing oscillator model of hydrodynamic forces on canonical structures. *Journal of Computational and Nonlinear Dynamics 4*, 4 (2009), 041006–041006–9.

[3] Anderson, J. D., and Wendt, J. *Computational fluid dynamics*, vol. 206. Springer, 1995.

[4] Anderson Jr, J. D. *Fundamentals of aerodynamics*. Tata McGraw-Hill Education, 1985.

[5] Antsaklis, P. J., and Michel, A. N. *Linear systems*. Springer Science & Business Media, 2006.

[6] Bai, Y., and Bai, Q. *Subsea pipelines and risers*. Elsevier, 2005.

[7] Bai, Y., and Bai, Q. *Subsea engineering handbook*. Gulf Professional Publishing, 2012.

[8] Barltrop, N. D. *Floating Structures: a guide for design and analysis*, vol. 1. Oilfield Pubns Inc, 1998.

[9] Bourguet, R., Karniadakis, G. E., and Triantafyllou, M. S. Lock-in of the vortex-induced vibrations of a long tensioned beam in shear flow. *Journal of Fluids and Structures 27*, 5 (2011), 838–847.

[10] Bourguet, R., Karniadakis, G. E., and Triantafyllou, M. S. Vortex-induced vibrations of a long flexible cylinder in shear flow. *Journal of fluid mechanics 677* (2011), 342–382.

[11] Bourguet, R., Karniadakis, G. E., and Triantafyllou, M. S. Multi-frequency vortex-induced vibrations of a long tensioned beam in linear and exponential shear flows. *Journal of Fluids and Structures 41* (2013), 33–42.

[12] Boyer, F., De Nayer, G., Leroyer, A., and Visonneau, M. Geometreically exact kirchhoff beam theory: Application to cable dynamics. *Journal of Computational and Nonlinear Dynamics 6*, 4 (2011), 041004.

[13] Bungartz, H.-J., Mehl, M., and Schäfer, M. *Fluid Structure Interaction II: Modelling, Simulation, Optimization*, vol. 73. Springer Science & Business Media, 2010.

[14] Bungartz, H.-J., and Schäfer, M. *Fluid-Structure Interaction: Modelling, Simulation, Optimisation*, vol. 1. Springer Science & Business Media, 2006.

[15] Butterfield, C. P., Musial, W., Jonkman, J., Sclavounos, P., and Wayman, L. *Engineering challenges for floating offshore wind turbines*. National Renewable Energy Laboratory Golden, CO, USA, 2007.

[16] Cardona, A., and Geradin, M. A beam finite element non-linear theory with finite rotations. *International journal for numerical methods in engineering 26*, 11 (1988), 2403–2438.

[17] Caretto, L., Curr, R., and Spalding, D. Two numerical methods for three-dimensional boundary layers. *Computer Methods in Applied Mechanics and Engineering 1*, 1 (1972), 39–57.

[18] Carey, G. F., and Oden, T. J. *Finite Elements: Fluid Mechanics Vol., VI*. Prentice-Hall, Inc., 1986.

[19] Chai, X., and Mahesh, K. Dynamic-equation model for large-eddy simulation of compressible flows. *Journal of Fluid Mechanics 699* (2012), 385–413.

[20] Chaplin, J., Bearman, P., Cheng, Y., Fontaine, E., Graham, J., Herfjord, K., Huarte, F. H., Isherwood, M., Lambrakos, K., Larsen, C., et al. Blind predictions of laboratory measurements of vortex-induced vibrations of a tension riser. *Journal of Fluids and Structures 21*, 1 (2005), 25–40.

[21] Chen, C.-T. *Linear system theory and design*. Oxford University Press, Inc., 1995.

[22] Childers, M. Deep Water Mooring Part I, Environmental Factors Control Station Keeping Methods. *Petroleum Engineer 10* (1974), 36–58.

[23] Childers, M. Deep Water Mooring Part II, The Ultradeep Water Spread Mooring System. *Petroleum Engineer 2* (1974), 108–118.

[24] Childers, M. Deep Water Mooring Part III, Equipment for Handling the Ultradeep Water Spread Mooring System. *Petroleum Engineer 5* (1975), 114–132.

[25] Chorin, A. J. Numerical solution of the Navier-Stokes equations. *Mathematics of computation 22*, 104 (1968), 745–762.

[26] Chung, T. *Computational fluid dynamics*. Cambridge university press, 2010.

[27] Coleman, T. F., and Li, Y. On the convergence of interior-reflective Newton methods for nonlinear minimization subject to bounds. *Mathematical Programming 67*, 1, 189–224.

[28] Coleman, T. F., and Li, Y. An interior trust region approach for nonlinear minimization subject to bounds. *SIAM Journal on optimization 6*, 2 (1996), 418–445.

[29] Cordle, A., Jonkman, J. M., and Hassan, G. G. *State of the art in floating wind turbine design tools*. National Renewable Energy Laboratory, 2011.

[30] Cummins, W. The impulse response function and ship motions. Tech. rep., DTIC Document, 1962.

[31] Donea, J., Giuliani, S., and Halleux, J. An arbitrary Lagrangian-Eulerian finite element method for transient dynamic fluid-structure interactions. *Computer methods in applied mechanics and engineering 33*, 1 (1982), 689–723.

[32] Donea, J., Huerta, A., Ponthot, J.-P., and Rodriguez-Ferran, A. Arbitrary Lagrangian-Eulerian Methods, volume 1, chapter 14. *Encyclopedia of Computational Mechanics, John Wiley & Sons* (2004).

[33] Evensen, G. The ensemble Kalman filter: Theoretical formulation and practical implementation. *Ocean dynamics 53*, 4 (2003), 343–367.

[34] Evensen, G. *Data assimilation: the ensemble Kalman filter*. Springer Science & Business Media, 2009.

[35] Facchinetti, M. L., de Langre, E., and Biolley, F. Coupling of structure and wake oscillators in vortex-induced vibrations. *Journal of Fluids and structures 19*, 2 (2004), 123–140.

[36] Faltinsen, O. *Sea loads on ships and offshore structures*, vol. 1. Cambridge university press, 1993.

[37] Gabbai, R., and Benaroya, H. An overview of modeling and experiments of vortex-induced vibration of circular cylinders. *Journal of Sound and Vibration 282*, 3 (2005), 575–616.

[38] Gallardo, D., Bevilacqua, R., and Sahni, O. Data-based hybrid reduced order modeling for vortex-induced nonlinear fluid–structure interaction at low Reynolds numbers. *Journal of Fluids and Structures 44* (2014), 115–128.

[39] Geuss, M., Panzer, H., and Lohmann, B. On parametric model order reduction by matrix interpolation. In *Control Conference (ECC), 2013 European* (2013), IEEE, pp. 3433–3438.

[40] Gobat, J., and Grosenbaugh, M. Time-domain numerical simulation of ocean cable structures. *Ocean Engineering 33*, 10 (2006), 1373–1400.

[41] Gobat, J. I. *The dynamics of geometrically compliant mooring systems.* PhD thesis, Massachusetts Institute of Technology and Woods Hole Oceanographic Institution, 2000.

[42] Goldstein, S. *Modern developments in fluid dynamics: an account of theory and experiment relating to boundary layers, turbulent motion and wakes*, vol. 1. Clarendon Press, 1938.

[43] Hansen, M. O. *Aerodynamics of wind turbines.* Routledge, 2015.

[44] Hartlen, R. T., and Currie, I. G. Lift-oscillator model of vortex-induced vibration. *Journal of the Engineering Mechanics Division 96*, 5 (1970), 577–591.

[45] Hartwanger, D., and Horvat, A. 3-D modeling of a wind turbine using CFD. In *NAFEMS Conference, United Kingdom* (2008).

[46] Haykin, S. *Kalman filtering and neural networks*, vol. 47. John Wiley & Sons, 2004.

[47] Herfjord, K., Drange, S., and Kvamsdal, T. Assessment of vortex-induced vibrations on deepwater risers by considering fluid-structure interaction. *Journal of Offshore Mechanics and Arctic Engineering 121*, 4 (1999), 207–212.

[48] Hilber, H. M., Hughes, T. J., and Taylor, R. L. Improved numerical dissipation for time integration algorithms in structural dynamics. *Earthquake Engineering & Structural Dynamics 5*, 3 (1977), 283–292.

[49] Hirt, C., Amsden, A. A., and Cook, J. An arbitrary Lagrangian-Eulerian computing method for all flow speeds. *Journal of Computational Physics 14*, 3 (1974), 227–253.

[50] Holmes, S., Oakley, O. H., and Constantinides, Y. Simulation of riser VIV using fully three dimensional CFD simulations. In *25th International Conference on Offshore Mechanics and Arctic Engineering* (2006), American Society of Mechanical Engineers, pp. 563–570.

[51] Houghton, E. L., and Carpenter, P. W. *Aerodynamics for engineering students*. Butterworth-Heinemann, 2003.

[52] Huang, S. Dynamic analysis of three-dimensional marine cables. *Ocean Engineering 21*, 6 (1994), 587–605.

[53] Huang, Z. *CFD simulation of riser VIV*. PhD thesis, Texas A&M University, 2011.

[54] Ibrahimbegović, A. On finite element implementation of geometrically nonlinear Reissner's beam theory: three-dimensional curved beam elements. *Computer methods in applied mechanics and engineering 122*, 1 (1995), 11–26.

[55] Ibrahimbegovic, A. On the choice of finite rotation parameters. *Computer Methods in Applied Mechanics and Engineering 149*, 1 (1997), 49–71.

[56] Ibrahimbegovic, A. *Nonlinear solid mechanics: theoretical formulations and finite element solution methods*, vol. 160. Springer Science & Business Media, 2009.

[57] Ibrahimbegovic, A., Niekamp, R., Kassiotis, C., Markovic, D., and Matthies, H. G. Code-coupling strategy for efficient development of computer software in multiscale and multiphysics nonlinear evolution

problems in computational mechanics. *Advances in Engineering Software 72* (2014), 8–17.

[58] IEC, T.-M. IEC 61400-3: Wind Turbines–Part 1: Design Requirements. *International Electrotechnical Commission, Geneva* (2005).

[59] Issa, R. I., Gosman, A., and Watkins, A. The computation of compressible and incompressible recirculating flows by a non-iterative implicit scheme. *Journal of Computational Physics 62*, 1 (1986), 66–82.

[60] Iwan, W., and Blevins, R. A model for vortex induced oscillation of structures. *Journal of Applied Mechanics 41*, 3 (1974), 581–586.

[61] Jain, A. Review of flexible risers and articulated storage systems. *Ocean engineering 21*, 8 (1994), 733–750.

[62] Jasak, H., Jemcov, A., and Tukovic, Z. OpenFOAM: A C++ library for complex physics simulations. In *International workshop on coupled methods in numerical dynamics* (2007), vol. 1000, pp. 1–20.

[63] Jelenić, G., and Crisfield, M. Interpolation of rotational variables in nonlinear dynamics of 3D beams. *International Journal for Numerical Methods in Engineering 43*, 7 (1998), 1193–1222.

[64] Jelenić, G., and Crisfield, M. Geometrically exact 3D beam theory: implementation of a strain-invariant finite element for statics and dynamics. *Computer Methods in Applied Mechanics and Engineering 171*, 1 (1999), 141–171.

[65] Jonkman, J. M. *Dynamics modeling and loads analysis of an offshore floating wind turbine*. ProQuest, 2007.

[66] Journée, J., and Massie, W. *Offshore hydromechanics*. TU Delft, 2000.

[67] Juang, J.-N. *Applied System Identification*. Prentice-Hall, Inc., Upper Saddle River, NJ, USA, 1994.

[68] Kalman, R. E. A new approach to linear filtering and prediction problems. *Journal of Fluids Engineering 82*, 1 (1960), 35–45.

[69] Katayama, T. *Subspace methods for system identification*. Springer Science & Business Media, 2006.

[70] Kim, W.-J., and Perkins, N. Coupled slow and fast dynamics of flow excited elastic cable systems. *Journal of vibration and acoustics 125*, 2 (2003), 155–161.

[71] Küttler, U., and Wall, W. A. Fixed-point fluid–structure interaction solvers with dynamic relaxation. *Computational Mechanics 43*, 1 (2008), 61–72.

[72] Kvamsdal, T., Amundsen, J., and Okstad, K. Numerical methods for fluid–structure interactions of slender structures. In *Proceedings of ECCM* (1999), vol. 99, Citeseer.

[73] Landahl, M. T., and Mollo-Christensen, E. *Turbulence and random processes in fluid mechanics*. Cambridge University Press, 1992.

[74] Larsen, C. M., Vikestad, K., Yttervik, R., and Passano, E. Empirical model for analysis of vortex induced vibrations-theoretical background and case studies. In *Proceedings of 20th International Conference on Offshore Mechanics and Arctic Engineering, OMAE* (2001), vol. 1.

[75] Larsen, C. M., Vikestad, K., Yttervik, R., Passano, E., and Baarholm, G. S. VIVANA–Theory Manual. *Marintek, Trondheim, Norway* (2001).

[76] Lesieur, M. *Turbulence in fluids*, vol. 40. Springer Science & Business Media, 2012.

[77] Ljung, L. *System Identification Toolbox for use with MATLAB: User's Guide*. Apr. 1988.

[78] Ljung, L. *System identification: theory for the user*, second ed. Prentice Hall information and system sciences series. 1999.

[79] Lyons, G., and Patel, M. Application of a general technique for prediction of riser vortex-induced response in waves and current. *Journal of Offshore Mechanics and Arctic Engineering 111*, 2 (1989), 82–91.

[80] Mainçon, P. A Wiener-Laguerre model of VIV forces given recent cylinder velocities. *Mathematical Problems in Engineering 2011* (2011), Article ID 414702, 43 pages.

[81] Manwell, J. F., McGowan, J. G., and Rogers, A. L. *Wind energy explained: theory, design and application*. John Wiley & Sons, 2010.

[82] Matthies, H. G., Niekamp, R., and Steindorf, J. Algorithms for strong coupling procedures. *Computer methods in applied mechanics and engineering 195*, 17 (2006), 2028–2049.

[83] McComb, W. D. The physics of fluid turbulence. *Chemical Physics 1* (1990).

[84] Mitigation, C. C. IPCC special report on renewable energy sources and climate change mitigation.

[85] Monin, A., Yaglom, A., and Ablow, C. Statistical Fluid Mechanics: The Mechanics of Turbulence. *American Journal of Physics 45* (1977), 1010–1010.

[86] Morison, J., Johnson, J., Schaaf, S., et al. The force exerted by surface waves on piles. *Journal of Petroleum Technology 2*, 05 (1950), 149–154.

[87] Nayfeh, A. H., Owis, F., and Hajj, M. R. A model for the coupled lift and drag on a circular cylinder. In *ASME 2003 International Design Engineering Technical Conferences and Computers and Information in Engineering Conference* (2003), American Society of Mechanical Engineers, pp. 1289–1296.

[88] Newman, J. N. *Marine hydrodynamics*. MIT press, 1977.

[89] Niekamp, R., and Matthies, H. CTL: a C++ communication template library. *GAMM Jahreshauptversammlung in Dresden 21* (2004), 27.

[90] Ogilvie, T. F. Recent progress toward the understanding and prediction of ship motions. In *5th Symposium on naval hydrodynamics* (1964), vol. 1, Bergen, Norway, pp. 2–5.

[91] Orszag, S. A. Analytical theories of turbulence. *Journal of Fluid Mechanics 41*, 02 (1970), 363–386.

[92] Palm, J., Paredes, G. M., Eskilsson, C., Pinto, F. T., and Bergdahl, L. Simulation of mooring cable dynamics using a discontinuous Galerkin method. In *Proceedings of 5th International Conference on Computational Methods in Marine Engineering, Hamburg, Germany* (2013).

[93] Panzer, H., Mohring, J., Eid, R., and Lohmann, B. Parametric model order reduction by matrix interpolation. *at-Automatisierungstechnik Methoden und Anwendungen der Steuerungs-, Regelungs-und Informationstechnik 58*, 8 (2010), 475–484.

[94] Patankar, S. V., and Spalding, D. B. A calculation procedure for heat, mass and momentum transfer in three-dimensional parabolic flows. *International Journal of Heat and Mass Transfer 15*, 10 (1972), 1787–1806.

[95] Peiró, J., and Sherwin, S. Finite difference, finite element and finite volume methods for partial differential equations. In *Handbook of materials modeling*. Springer, 2005, pp. 2415–2446.

[96] Phan, M., Juang, J.-N., and Longman, R. W. *On Markov parameters in system identification*. National Aeronautics and Space Administration, Langley Research Center, 1991.

[97] Qin, L. *Development of Reduced-Order Models for Lift and Drag on Oscillating Cylinders with Higher-Order Spectral Moments*. PhD thesis, Virginia Tech, Blacksburg, VA, 2004.

[98] Qiu, W., Lie, H., Rousset, J., Sphaier, S., Tao, L., Wang, X., Mikami, T., and Magarovskii, V. Report of the Ocean Engineering Committee. In *27th International Towing Tank Conference* (2014), pp. 1–74.

[99] Regg, J. B., Adams, S., Hauser, B., Hennessey, J., Kruse, B. J., Lowenhaupt, J., Smith, B., and White, A. Deepwater Development: A Reference Document for the Deepwater Environmental Assessment Gulf of Mexico OCS (1998 through 2007). *OCSReport MMS-2000-015, US DOI, Minerals Management Service Gulf of Mexico OCSRegion, New Orleans, Louisiana* (2000).

[100] Reissner, E. On one-dimensional finite-strain beam theory: the plane problem. *Zeitschrift für angewandte Mathematik und Physik ZAMP 23*, 5 (1972), 795–804.

[101] Robertson, A., Jonkman, J., Vorpahl, F., Popko, W., Qvist, J., Frøyd, L., Chen, X., Azcona, J., Uzunoglu, E., Soares, C. G., et al. Offshore code comparison collaboration continuation within IEA Wind Task 30: Phase II results regarding a floating semisubmersible

wind system. In *ASME 2014 33rd International Conference on Ocean, Offshore and Arctic Engineering* (2014), American Society of Mechanical Engineers, pp. V09BT09A012–V09BT09A012.

[102] Rosić, B., J., S., Pajonk, O., A., K., and Matthies, H. Comparison of Numerical Approaches to Bayesian Updating. Tech. rep., TU Braunschweig, http://www.digibib.tu-bs.de/?docid=00057895, 2014.

[103] Rosić, B. V., Kučerová, A., Sỳkora, J., Pajonk, O., Litvinenko, A., and Matthies, H. G. Parameter identification in a probabilistic setting. *Engineering Structures 50* (2013), 179–196.

[104] Ross, M. R., Sprague, M. A., Felippa, C. A., and Park, K. Treatment of acoustic fluid–structure interaction by localized Lagrange multipliers and comparison to alternative interface-coupling methods. *Computer Methods in Applied Mechanics and Engineering 198*, 9 (2009), 986–1005.

[105] Sagaut, P. *Large Eddy Simulations for Incompressible Flows*, vol. 3. Springer Berlin, 2000.

[106] Sarpkaya, T. Vortex-induced oscillations: a selective review. *Journal of applied mechanics 46*, 2 (1979), 241–258.

[107] Sarpkaya, T. A critical review of the intrinsic nature of vortex-induced vibrations. *Journal of Fluids and Structures 19*, 4 (2004), 389–447.

[108] Schulz, K. W., and Meling, T. S. Multi-strip numerical analysis for flexible riser response. In *ASME 2004 23rd International Conference on Offshore Mechanics and Arctic Engineering* (2004), American Society of Mechanical Engineers, pp. 379–384.

[109] Sezer-Uzol, N., and Long, L. N. 3-D time-accurate CFD simulations of wind turbine rotor flow fields. *AIAA paper 394* (2006), 2006.

[110] Shim, S., Kim, M., et al. Rotor-floater-tether coupled dynamic analysis of offshore floating wind turbines. In *The Eighteenth International Offshore and Polar Engineering Conference* (2008), International Society of Offshore and Polar Engineers.

[111] Shur, M., Spalart, P. R., Squires, K. D., Strelets, M., and Travin, A. Three-Dimensionality in Reynolds-Averaged Navier-Stokes

Solutions Around Two-Dimensional Geometries. *AIAA journal 43*, 6 (2005), 1230–1242.

[112] Simiu, E., and Scanlan, R. H. *Wind effects on structures*. Wiley, 1996.

[113] Simo, J. A finite strain beam formulation. The three-dimensional dynamic problem. Part I. *Computer methods in applied mechanics and engineering 49*, 1 (1985), 55–70.

[114] Simo, J. C., and Vu-Quoc, L. On the dynamics in space of rods undergoing large motions—a geometrically exact approach. *Computer methods in applied mechanics and engineering 66*, 2 (1988), 125–161.

[115] Skop, R., and Griffin, O. A model for the vortex-excited resonant response of bluff cylinders. *Journal of Sound and Vibration 27*, 2 (1973), 225–233.

[116] Srinil, N., and Zanganeh, H. Modelling of coupled cross-flow/in-line vortex-induced vibrations using double Duffing and van der Pol oscillators. *Ocean Engineering 53* (2012), 83–97.

[117] Strouhal, V. Über eine besondere Art der Tonerregung. *Annalen der Physik 241*, 10 (1878), 216–251.

[118] Taylor, R. L. FEAP - Finite Element Analysis Program, 2014.

[119] Thomas, D., Hearn, G., et al. Deepwater mooring line dynamics with emphasis on seabed interference effects. In *Offshore Technology Conference* (1994), Offshore Technology Conference.

[120] Tognarelli, M. A., Taggart, S., and Campbell, M. Actual VIV fatigue response of full scale drilling risers: with and without suppression devices. In *ASME 2008 27th International Conference on Offshore Mechanics and Arctic Engineering* (2008), American Society of Mechanical Engineers, pp. 513–525.

[121] Tong, K. Technical and economic aspects of a floating offshore wind farm. *Journal of Wind Engineering and Industrial Aerodynamics 74* (1998), 399–410.

[122] Triantafyllou, M. VIVA extended user's manual. *Massachusetts Institute of Technology, Department of Ocean Engineering, Cambridge, MA, USA* (2003).

[123] Trim, A., Braaten, H., Lie, H., and Tognarelli, M. Experimental investigation of vortex-induced vibration of long marine risers. *Journal of fluids and structures 21*, 3 (2005), 335–361.

[124] Van Overschee, P., and De Moor, B. *Subspace identification for linear systems: Theory—Implementation—Applications*. Springer Science & Business Media, 2012.

[125] Vandiver, J. Dimensionless parameters important to the prediction of vortex-induced vibration of long, flexible cylinders in ocean currents. *Journal of Fluids and Structures 7*, 5 (1993), 423–455.

[126] Vandiver, J. K., et al. Drag coefficients of long flexible cylinders. In *Offshore technology conference* (1983), Offshore Technology Conference.

[127] Vandiver, J. K., and Li, L. SHEAR7 V4. 4 program theoretical manual. *Department of Ocean Engineering, Massachusetts Institute of Technology* (2005).

[128] Versteeg, H. K., and Malalasekera, W. *An introduction to computational fluid dynamics: the finite volume method*. Pearson Education, 2007.

[129] Vryhof Anchors. Mooring Systems. `http://www.vryhof.com/pdf_2010/Mk5-MooringSystem.pdf`, 2010. [Online; retrieved February 22, 2016].

[130] Walton, T. S., and Polachek, H. Calculation of transient motion of submerged cables. *Mathematics of computation 14*, 69 (1960), 27–46.

[131] Wang, C., and Tay, Z. Very large floating structures: applications, research and development. *Procedia Engineering 14* (2011), 62–72.

[132] Wayman, E. N., Sclavounos, P., Butterfield, S., Jonkman, J., Musial, W., et al. Coupled dynamic modeling of floating wind turbine systems. In *Offshore Technology Conference* (2006), Offshore Technology Conference.

[133] Wieselsberger, C. New data on the laws of fluid resistance. *Phys.Z. 22*, 11 (1921), 321–328.

[134] Wilcox, D. C., et al. *Turbulence modeling for CFD*, vol. 2. DCW industries La Canada, CA, 1998.

[135] Willden, R., and Graham, J. Numerical prediction of VIV on long flexible circular cylinders. *Journal of Fluids and Structures 15*, 3 (2001), 659–669.

[136] Willden, R. H., and Graham, J. M. R. CFD simulations of the vortex-induced vibrations of model riser pipes. In *ASME 2005 24th International Conference on Offshore Mechanics and Arctic Engineering* (2005), American Society of Mechanical Engineers, pp. 837–846.

[137] Willems, J. C., and Polderman, J. W. *Introduction to mathematical systems theory: a behavioral approach*, vol. 26. Springer Science & Business Media, 2013.

[138] Williams, R. L., Lawrence, D. A., et al. *Linear state-space control systems*. John Wiley & Sons, 2007.

[139] Williamson, C., and Govardhan, R. Vortex-induced vibrations. *Annu. Rev. Fluid Mech. 36* (2004), 413–455.

[140] Williamson, C., and Govardhan, R. A brief review of recent results in vortex-induced vibrations. *Journal of Wind Engineering and Industrial Aerodynamics 96*, 6 (2008), 713–735.

[141] Wu, X., Ge, F., and Hong, Y. A review of recent studies on vortex-induced vibrations of long slender cylinders. *Journal of Fluids and Structures 28* (2012), 292–308.

[142] Zheng, H., Price, R., Modarres-Sadeghi, Y., Triantafyllou, G. S., and Triantafyllou, M. S. Vortex-induced vibration analysis (VIVA) based on hydrodynamic databases. In *ASME 2011 30th International Conference on Ocean, Offshore and Arctic Engineering* (2011), American Society of Mechanical Engineers, pp. 657–663.

[143] Zienkiewicz, O. C., and Taylor, R. L. *The finite element method for solid and structural mechanics*. Butterworth-heinemann, 2005.